Politecnico di Torino

Master's Degree in Chemical and Sustainable Processes Engineering

Design of a Separation System to Recover N-decafluorobutane from a Gas Mixture

Engineering of a Small Chemical Plant

Candidate:
Damiano Galassi

Supervisors:
Fabio Alessandro Deorsola (PoliTO)
Roberto Guida (Cern)

Politecnico di Torino
A.A. 2022/2023

Declaration

I hereby declare that, the contents and organization of this dissertation constitute my own original work and does not compromise in any way the rights of third parties, including those relating to the security of personal data.

Damiano Galassi
2023

Acknowledgements

I would like to dedicate this space to thank all those who have supported me throughout my educational, personal, and life journey.

First and foremost, I dedicate this work to my mother and my grandparents. To my three pillars, I owe my essence and my way of being. I owe you my determination, tenacity, and dedication. Specifically, I thank my grandfather for not only supporting me financially during my university years but, more importantly, for being there for me in the toughest moments and encouraging me to give my best in every situation. With your great patience and experience, you have guided me in making the most important decisions. You've always known how to advise me and analyze every situation to make the wisest and most rational decisions. I thank my mother for making me who I am. You've dedicated everything to me, and to you, I will dedicate every small and great achievement.

Secondly, I thank all my colleagues at CERN. I want to dedicate a few words to each of them. To Fabio Bordon, thank you for helping me in building the systems and for teaching me a lot with your "young experience." I also thank you for your smiles and the wonderful moments we've shared. To Maria Cristina Arena, thank you for assisting me in the analyses and providing me with the fundamental data for the selection and sizing of the accumulation tank. But I also want to thank you for your friendliness and treating me like a younger brother. To Mattia Busato, thank you, colleague, for helping me understand the organization's mechanisms and for contributing to the realization of this fantastic project. To Alessio Galloro and Stefano Saroglia, even though we're not technically department colleagues, thank you for your advice and pleasant conversations. To Bianca Sabiu, thank you for teaching me to use various tools that will be extremely useful in my future. Thanks also to Michele Bruno, who graduated a few weeks ago and was my internship companion in this adventure. Together, we worked wonderfully and motivated

each other to achieve our goals. Gianluca Rigoletti, thank you for assisting me in defining the control systems, and thanks for your hospitality, warmth, and extreme professionalism. I would like to thank Mattia Verzeroli, Stefania Juks, Kacper Jerzy Kapusniak for welcoming me as a family member. I thank my supervisor, Roberto Guida, for this magnificent experience and for allowing me to express my ideas, thoughts, and knowledge freely and openly. I hope to continue working with all of you and contribute to achieving the goals we pursue day by day.

Finally, I am infinitely grateful to my dearest course c ompanions. Davide Di Profio, Giulio Bernardi, Amin Bouzaiene, and above all, Federico Fiore and Valerio Romiti, with whom I have shared all the joys and sorrows that this course of study has presented to us.

Words could never be enough to thank you; each of you has left either a profound or a small mark in my life. You are and will always be a part of who I am.

Abstract

In recent years, CERN has faced a significant environmental and economic challenge due to the extensive use of gas mixtures with a high Global Warming Potential. Approximately 70% of CERN's emissions are attributed to the use of fluorinated gases in various gas detectors. Specifically, the LHCb (Large Hadron Collider "Beauty") experiment utilizes a mixture of carbon dioxide and n-decafluorobutane. Not only does C_4F_{10} have a high environmental impact (9200 kg of CO_2 per kg of C_4F_{10}), but it has also seen a reduction in production due to EU regulations, leading to increased costs. This thesis aims to tackle this challenge by implementing a new strategy for the separation of the mixture. The recovery of these two molecules can significantly reduce pollution and allow for the replenishment of a fresh mixture in the LHCb detector. This thesis offers a comprehensive exploration of the principles, technologies, and strategies for the development of an advanced fluorinated gas recovery plant. The development of a standardized approach to one of the gas mixtures could serve as a foundation to recover and reuse high-polluting gases. The first chapter introduces CERN and the LHCb experiment, which investigates the decay of b-quarks and provides insights into matter-antimatter asymmetries. The use of C_4F_{10} in the RICH-1 detector is explained, followed by an overview of the current methods to supply, distribute, and manage exhaust and recovery modules. The second chapter discusses the different phases of LHCb experiments (Filling, Cleaning, and Emptying) and the challenges faced while defining the project's goals. The existing recovery system, which includes a partial condenser, is analyzed, highlighting its inability to guarantee the required purity due to variable composition and flow rates of the incoming feed and the lack of a control system to control process variables. The third chapter delves into the nature of the binary mixture. It defines metrics for measuring system performance and objectives and reviews the vapor-liquid equilibria. Thermodynamic models based on equations of state and predictive models are examined to select the most suitable physicochemical model.

The choice is made based on minimizing errors between experimental evidence and model predictions. The fourth chapter focuses on the design phase. It begins with assessing the performance of the current recovery system, and revealing its inefficiency. The design choices are explained, highlighting the need to equalize the incoming stream and design a control system for managing disturbances. The plant consists of three subsystems: an Accumulation Tank and Pumping Station (ATPS) and two Separation Systems. The ATPS, which is responsible for accumulating the gas exiting the detector follows, is explained. The first recovery system (DSE), consisting of two buffers, is then discussed. The influence of pressure and operating temperatures on purity, recovery, and recirculation flow rate are studied in-depth. The fourth chapter ends with the design of the second recovery system, a packed-bed distillation column (DC). The work includes defining specifications, degrees of freedom, and optimizing key variables to achieve the desired outcomes. The column's design, condenser, and reboiler are discussed, as well as the control loop. The conclusion and various appendices provide information on the current status of the plant, potential issues, and a timeline for future needs and developments.

Summary (Sommario)

0.0.1 Introduzione

Il Centro Europeo per la Ricerca Nucleare, noto come CERN, è stato fondato nel 1954 ed è la principale istituzione europea per lo studio della fisica delle particelle. Situato vicino a Ginevra, al confine tra Svizzera e Francia, ospita il “Large Hadron Collider” (LHC) e altri acceleratori progettati per far collidere fasci di protoni. Il LHC permette di approfondire la comprensione dei fenomeni che si sono verificati durante la nascita dell’universo. L’istituto è costituito da diverse strutture, tra cui il Rivelatore LHCb, situato a 100 metri sotto terra vicino a Ferney-Voltaire, in Francia (Fig. 1.1). Questo rivelatore è dedicato allo studio dei "quark beauty" e contribuisce alla comprensione dell’asimmetria tra materia e antimateria [1]. La struttura di LHCb è suddivisa nei seguenti sottosistemi. Il Vertex Locator (VELO) viene utilizzato per identificare con precisione i punti di interazione dei protoni e il decadimento dei mesoni. La presenza di un magnete e una serie di piani rivelatori consente di misurare la traiettoria delle particelle cariche e il loro momento sfruttando la curvatura indotta dal campo magnetico. Segue il sistema di Rivelatori Cherenkov ad Anello di Immagine (RICH) [2]. Il suo ruolo è di identificare particelle cariche nell’intervallo di momento di 1-150 GeV/c. Il sistema è composto da un rivelatore a monte (RICH-1) con radiatori in aerogel di silice e C_4F_{10} e un rivelatore a valle (RICH-2) con un radiatore di gas CF_4, posizionato dietro l’anello magnetico e il sistema di tracciamento. L’aerogel di silice, a causa della bassa densità, viene utilizzato per rivelare le particelle a basso momento. Al contrario, i fluorocarburi sono in grado di gestire momenti più elevati (da 10 a 65 GeV/c per il C_4F_{10} e da 15 a 150 GeV/c per il CF4). Le particelle prodotte durante le collisioni attraversano gli specchi di RICH-1 prima di raggiungere i componenti di misurazione a valle.

L'energia trasportata da elettroni, fotoni e adroni che attraversano il rivelatore può essere rilevata dai calorimetri elettromagnetici (ECAL) o per adroni (HCAL) [3].

Come detto in precedenza l'intero sistema si basa sull'effetto Cherenkov, in cui le particelle cariche, muovendosi più velocemente della luce nel mezzo, emettono una distintiva radiazione elettromagnetica blu. Gli specchi presenti riflettono le particelle prodotte nei radiatori contenenti C_4F_{10} [4], [5]. Per cui, al fine di garantire il corretto funzionamento del detector, due sono gli aspetti da controllare finemente. In primis, la natura del gas presente nel radiatore è chiave per garantire un'elevata affidabilità delle misurazioni. Tra i diversi gas utilizzati in numerosi test, la famiglia dei n-perfluorocarburi offre un'ampia gamma di indici di rifrazione, in particolare il n-decafluorobutano, rappresenta un compromesso ottimale tra alto indice di rifrazione e trasparenza [6]. In secondo luogo, bisogna dotare il rivelatore di un sistema che ne suporti il funzionamento. Per tale ragione sono stati progettati diversi moduli: (1) Il *Sistema di Monitoraggio e Distribuzione* il quale si occupa di distriburie il gas; (2) Il *Modulo di Miscelazione* che funge da vaporizzatore di miscele liquide e fine miscelatore di diverse molecole; (3) Il *Modulo di Pompaggio* che ha lo scopo di fornire l'energia necessaria per vincere le perdite di carico lungo il sistema; (4) Il *Modulo di Esausto* attraverso cui i gas esausti o contaminati vengono scaricai in atmosfera; (5) Il *Modulo di Recupero* il quale si pone come obiettivo quello di separare i componeti in miscela e ottenere delle speci pure da poter riutillizare. L'ottimizzazione del recupero costituisce uno degli obiettivi principali del CERN. Infatti, secondo i dati IPCC (Fifth Assessment Report) [7], il GWP a 100 anni del decafluorobutano si attesta su un valore di 9200 kg equivalenti di anidride carbonica. Per tali ragioni la costruzione di un nuovo modulo di recupero costituisce l'obiettivo di questo lavoro.

0.0.2 Le Fasi del RICH-1 e L'Attuale Sistema di Recupero del Decafluorobutano

Prima di procedere con la spiegazione dell'attuale sistema di recupero si ritiene necessario dare un'introduzione alle fasi che distinguono i diversi momenti delle sperimentazioni su LHCb. Vi sono tre fasi: *Filling, Cleaning* e *Emptying*. Il *Filling* consiste nell'inieizione di C_4F_{10} al fine di scaricare l'anidride carbonica utilizzata per l'inertizzazione e la messa in sicurezza del rivelatore. Il decafluorobutano,

immagazzinato in fase liquida, viene vaporizzato e inviato all'interno del circuito con una portata compresa tra 110 e 160 NL/h. Il processo di riempimento dura circa 50-100 ore, e la composizione molare della miscela, CO_2-C_4F_{10}, misurata al modulo di pompaggio, varia durante l'intero intervallo temporale. L'attuale sistema di recupero (*Liquifier*, Fig. 2.3), basato sul principio di condensazione del componente meno volatile (C_4F_{10}), viene avviato intorno alla decima ora, in quanto, come si osserva in Figura 2.2, la frazione di decafluorobutano è, fino a questo momento, trascurabile. Da ciò, si possono immediatamente evidenziare le ragioni delle basse performance del liquifier. Infatti, l'alimentazione presenta una portata oscillante, una composizione fortemente variabile nel tempo e, inoltre, la mancanza di un sistema di controllo in grado di variare le condizioni termodinamiche non permette di modificare la temperatura e la pressione operativa del sistema. Il *Cleaning* è un'operazione in ciclo chiuso durante cui vengono estratte, tramite un processo di adsorbimento (*Purifier*, Fig. 2.5), le rimanenze di anidride carbonica ed eventuali tracce di acqua e aria dovute alla presenza di eventuali punti di perdita lungo l'intero sistema. Infine, L'*Emptying* costituisce il processo inverso al filling. Durante questa fase il sistema viene inertizzato inviando anidride carbonica per spingere fuori dal circuito il decafluorobutano.

0.0.3 Equilibri Binari tra Anidride Carbonica e Decafluorobutano

Come accennato nel paragrafo precedente, il funzionamento del liquifier si basa su un meccanismo di condensazione parziale. Questa tecnica sfrutta la volatilità relativa tra le molecole in miscela. Per tale ragione, l'investigazione degli equilibri termodinamici risulta fondamentale per comprenderne le performance. Queste verranno espresse in termini di purezza (Eq. 3.1) e recupero (Eq. 3.2) di C_4F_{10}. In generale, la condizione di equilibrio liquido vapore (VLE), viene espressa attraverso l'uguaglianza dei potenziali chimici (μ) delle specie presenti nelle due fasi. L'utilizzo dalle Equazioni 3.3, 3.4 e 3.5 permette di esprimere questa condizioni in termini di frazioni molari dei diversi componenti nelle distinte fasi, pressione totale, pressione di vapore e coefficienti di attività e fugacità. Generalmente, il coefficiente di fugacità può essere considerato unitario in sistemi termodinamici a bassa pressione, d'altra parte, assumere un coefficiente di attività unitario significherebbe trascurare le interazioni molecolari in fase liquida. Nel caso in esame, la presenza di

un gas incondensabile, come la CO_2, rende la modellazione ancor più complessa. Di fatto, l'approccio migliore sarebbe la determinazione della solubilità dell'anidride carbonica all'interno della fase liquida e la costruzione di modelli basati sulla legge di Henry. Diversi autori, tra cui Costa Gomes [8] e Benoit Gwinner [9], hanno evidenziato l'elevata solubilità della CO_2 all'interno di idrocarburi fluorurati. Questo fenomeno è principalmente dovuto ai maggiori angoli diedrali e distanze tra i legami carbonio-carbonio. D'altronde, il meccanismo di solubilizzazione può essere descritto come la serie tra (1) la formazione di cavità nella molecola ospitante (rottura dei legami solvente-solvente) e (2) all'inserzione del soluto all'interno del vuoto creatosi (formazione di legami soluto-solvente). Tra i due, il primo step si dimostra, nella maggioranza dei casi, il fattore limitante. Per cui, la presenza di molecole di fluoro favorisce la solubilizzazione della CO_2. In altre parole, gli idrocarburi fluorurati sono in grado di ospitare, a parità di condizioni esterne, una maggiore quantità di anidride carbonica rispetto agli alcani idrogenati di riferimento.

Sfortunatamente, la letteratura pone l'attenzione su fluorocarburi a lunga catena (C6+), in quanto, meno volatili, presentano ottime caratteristiche per essere utilizzati come solventi nell'estrazione di anidride carbonica per mezzo di processi di assorbimento. Dunque, avendo a disposizione una serie di dati basati su relazioni VLE (Valtz et al. [10]) si è deciso di procedere alla determinazione del metodo termodinamico più adatto attraverso l'utilizzo di modelli matematici (Appendice A) in grado restituire il metodo che minimizzasse gli errori tra evidenze sperimentali e predizioni fornite dal modello medesimo. Numerosi metodi sono stati testati, tra questi i piu promettenti risultano essere NRTL-HOC (Non-Random-Two-Liquids accoppiato all'equazione di stato di Hayden-O'Connel, [11], [12]) e NRTL-RK (Non-Random-Two-Liquids accoppiato all'equazione di stato di Redlich-Kwong, [11], [13]). La Figura 3.3 riporta dei diagrammi *Pxy* tra CO_2 e C_4F_{10}. Da questa è possibile notare come i suddetti metodi siano in grado di predire le evidenze sperimentali con ottimi risultati se confrontate a modelli basati solamente su equazioni di stato (EOS), come Peng-Robinson (PR [14]), usato come "benchmark" di riferimento. Le Figure da 3.4 a 3.7, invece, riportano gli errori quadratici tra dati sperimentali e predizioni dei diversi modelli termodinamici. In particolare, fissata la composizione molare in fase liquida, si determina: (1) l'errore (Fig. 3.4) e l'errore quadratico (Fig. 3.5) tra la composizione in fase vapore misurata sperimentalmente e predetta (PR, NRTL-HOC e NRTL-RK) a date condizioni di pressione e temperatura; (2) l'errore (Fig. 3.4) e l'errore quadratico (Fig. 3.5) tra la pressione di vapore esercitata dalla miscela

misurata sperimentalmente e predetta (PR, NRTL-HOC e NRTL-RK) a date condizioni di composizione e temperatura. In questo secondo caso, il valore di pressione di vapore ottenuto dai modelli è stato normalizzato rispetto al valore sperimentale (Appendice A) in modo tale da avere come riferimento la pressione sperimentale stessa. Questi grafici e le Tabelle da 3.2 a 3.4 mettono in luce la qualità dei suddetti modelli rispetto al benchmark. In conclusione, si evidenzia che, il modello scelto per il dimensionamento e la simulazione dei sistemi progettati è NRTL-RK. La scelta finale ricade su questo modello in quanto si dimostra migliore negli intervalli termici (temperature prossime a 0 °C) a cui faremo successivamente riferimento.

0.0.4 Performance dell'Attuale Sistema di Recupero

Nei paragrafi precedenti sono state descritte le problematiche associate all'uso dell'attuale sistema di recupero. Poichè lo scopo di questo progetto è la progettazione di un nuovo impianto volto al miglioramento delle performance correnti, risulta interessante analizzare in modo approfondito le operazioni svoltesi quest'anno al fine di inquadrare il problema e trovare una soluzione specifica e mirata.

Per comprendere il funzionamento del processo attuale del liquifier e ottenere un quadro più preciso delle condizioni del condensato che esce dallo stadio di separazione e la relativa efficienza si fa uso del diagramma *Txy*. Il diagramma *Txy* è un grafico isobaro che descrive le dinamiche di una miscela binaria in funzione di composizione e temperatura. Due curve, dette di rugiada e di ebollizione definiscono tre diversi domini in cui si distinguono il vapore, la lente bifasica e il liquido. Il diagramma Txy per il sistema in esame è mostrato in Figura 4.1. Le curve di rugiada e di ebollizione sono mostrate specificamente a pressioni di 1, 2, 3, 4 e 5 bar. Ci sono quindi due fasi in equilibrio quando la pressione, ad esempio, è fissata a 3 bar e la temperatura è impostata tra i punti di ebollizione dei due costituenti della miscela. L'intersezione tra un'isoterma e le curve di rugiada e di ebollizione descrive rispettivamente la composizione e la quantità delle fasi di vapore e liquido. Ad esempio, fissando T e P, rispettivamente, a -25°C (temperatura operativa nominale del liquifier) e 3 bar (Fig 4.2) è possibile determinare le composizioni delle due fasi. Essendo una regione bivariante, fissando due parametri (T, P), la composizione delle due fasi può essere identificata in modo univoco, indipendentemente dalla composizione iniziale (il punto A corrisponde al punto D e il punto B al punto E). Tuttavia, selezionando una composizione iniziale differente, si otterranno diverse

proporzioni quantitative (in termini di massa) tra le due fasi. Entrando nel diagramma con un vapore che contiene il 30% mol di CO_2 a circa 25°C e iniziando a rimuovere calore fino a -25°C (diagramma di sinistra), si ottiene con una miscela bifase. La fase di vapore avrà una composizione al 90% mol di CO_2 (punto B) e il liquido in equilibrio con essa avrà il 12% mol di CO_2. Tuttavia, la regola della leva è utilizzata per calcolare la quantità di vapore e liquido in termini molari. Di conseguenza, il rapporto tra le lunghezze dei segmenti AC e BC fornisce la relazione tra le moli di vapore e liquido. Questa breve spiegazione ci aiuta a capire che la purezza della fase liquida non è perfetta come il CERN aveva sperato. In ragione di ciò, la purezza e la quantità di decafluorobutano recuperato variano al variare delle condizioni di composizione in ingresso al Liquifier.

I dati relativi alle operazioni svolte nel primo semestre di quest'anno (2023) supportano questa rapida valutazione. La procedura di filling è avvenuta tra il 07/03/2023 e il 28/03/2023. Questo processo viene ulteriormente diviso in due sotto-fasi, dette *Filling I* e *Filling II*. Il sistema di recupero è stato attivato il 07/03/2023. Durante le prime ore la fase gassosa presente nel serbatoio di accumulo del decafluorobutano viene utilizzato per l'iniezione. Quando la frazione molare di C_4F_{10} nel circuito è prossima a quella del gas iniettato si inizia ad utilizzare il liquido (in quanto più ricco in decafluorobutano) come alimentazione. La composizione del gas e del liquido alimentati è riportata in Tabella 4.1. Questo processo, della durata di circa 50 ore, definisce il filling I. Durante queste operazioni si iniettano 63.7 kg di C_4F_{10}, di cui 49.6 kg restano nel circuito del detector, 8.7 kg vengono espulsi in atmosfera e i restanti 5.4 kg vengono idealmente recuperati. Il termine ideale vuole sottolineare che 5.4 kg indica la massa di decafluorobutano che si potrebbe recuperare qualora il condensato fosse puro. La Figura 4.3 riassume questi risultati. Il 15 marzo 2023 inizia la seconda fase (Filling II). Il periodo di tempo tra il filling I e II è volto per la pulizia del serbatoio di accumulo. In effetti, è necessario fornire un flusso di alimentazione più ricco in C_4F_{10}. La pulizia avviene in un ciclo semichiuso, il che significa che il circuito principale non è collegato al sistema di separazione. Il vapore nel serbatoio viene inviato alla consueta fase di liquefazione parziale. Le composizioni di vapore all'interno del serbatoio all'inizio di questo processo (10/03/2023) e alla fine (14/03/2023) sono mostrate nella Tabella 4.3. Il filling II inizia ufficialmente il 15/03/2023. Le modalità con cui viene condotta questa fase sono identiche a quelle descritte precedentemente. Tuttavia, anche in questo caso, è utile e piuttosto affascinante esaminare i dati raccolti. L'andamento della composizione del gas

misurato al modulo di pompaggio è riportato in Figura 4.4. Le prestazioni della prima e della seconda fase di riempimento in termini di efficienza (Equazioni 4.1 e 4.2) sono, rispettivamente, 38% e 88%. Si noti come l'efficienza del filling II sia molto maggiore. Questo risultato può essere spiegato dal fatto che una miscela già estremamente ricca di C_4F_{10} viene alimentata al liquifier, per cui la frazione di liquido formata (a condizioni di processo costanti) è molto maggiore rispetto a quella del gas che esce come esausto. L'andamento dell'efficienza nel corso di singoli giorni del filling II conferma questo effetto. Si noti che la trendline (Figura 4.6) aumenta man mano che ci si avvicina alla conclusione del processo di riempimento. In conclusione, la massa totale di C_4F_{10} recuperata durante le due operazioni è di circa 41,5 kg, ma le perdite sono significativamente maggiori. Inoltre, la purezza del condensato è molto al di sotto dei livelli desiderati.

0.0.5 Progettazione del Nuovo Sistema di Separazione

Come precedentemente riportato, i punti di ebollizione delle due molecole in esame, diossido di carbonio e perfluorobutano, sono piuttosto diversi l'uno dall'altro. Inoltre, per trarre paralleli con la tecnologia attuale di separazione (condensazione parziale), è stato scelto di costruire due sistemi che, pur utilizzando gli stessi principi di separazione, sono unici nel loro genere. I due sistemi sono: (1) Doppio Stadio di Equilibrio (DSE); (2) Colonna di Distillazione (DC). Al fine di garantire l'affidabilità del sistema ed ovviare alla variazione di composizione e portata alimentate si è deciso di inserire un serbatoio di equalizzazione per garantirne la costanza. Per cui, la struttura dell'impianto può essere divisa in base a due periodi temporali distinti: accumulo e separazione. Infine, è stata installata una piccola stazione di pompaggio per la compressione e la movimentazione dei fluidi. I prossimi sottocapitoli sono dedicati alla descrizione, progettazione e simulazione dei tre sottosistemi (doppio stadio di equilibrio, colonna di distillazione e serbatoio di accumulo e stazione di pompaggio). Prima di procedere con la lettura, si consiglia di fare riferimento all'Appendice B, dove è fornito il P&ID dell'intero sistema insieme ad una breve spiegazione.

Progettazione del Tank di Accumulazione e della Stazione di Pompaggio (ATPS)

La sezione di accumulo e compressione è una parte critica del sistema di separazione. La miscela gassosa proveniente dal rivelatore passa attraverso un ciclo di compressione controllato da sensori di pressione e valvole pneumatiche. Nella fase di accumulo la miscela viene compressa e immessa nel serbatoio di equalizzazione. La fase di separazione, durante la quale la miscela accumulata viene inviata ai sistemi di recupero, viene, per semplicità, suddivisa in separazione I e II. Durante la prima sottofase la pressione del serbatoio è maggiore di quella operativa degli organi di separazione, per cui si avrà un moto dettato da tale gradiente. Nella seconda fase, invece, si sfrutta lo stesso loop di compressione utilizzato per l'accumulo. Una valvola a tre vie si occupa di dirigere il flusso al sistema a doppio stadio o al sistema di distillazione. Per una descrizione più dettagliata si faccia riferimento alla sezione 4.3.

Introdotto il funzionamento di questo sottosistema si passa ai criteri di dimensionamento del serbatoio. Per tale scopo sono necessarie molte informazioni, come il volume di progettazione (V_D), la pressione e la temperatura di esercizio (P_{op} T_{op}), la pressione e la temperatura massime e minime, e la composizione della miscela. Il volume richiesto è stato valutato sfruttando che la quantità di gas utilizzata per pulire la camera del rivelatore (RICH-1) durante il riempimento è di circa 16 Nm^3. Al fine di ridurre le dimensioni del serbatoio, è stata scelta una pressione di progettazione di 7 bar. Con questa opzione, è possibile scegliere un serbatoio significativamente più piccolo (le dimensioni sono ridotte di 7 volte se si approssima la miscela ad un gas ideale). Due fattori di correzione k_g e k_T (Equazioni 4.3 e 4.4) sono stati rispettivamente adottati per tenere in considerazione l'assunzione di idealità della miscela e conto delle variazioni del volume specifico (V_m) con la temperatura. Le variazioni termiche sono dovute al processo di compressione. Nonostante ciò, avendo considerato la cessione di calore verso l'esterno del gas in moto nei tubi, in condizioni di lavoro nominali, non si raggiunge la temperatura massima di 100 °C. In ogni caso, due valvole di sicurezza garantiscono la messa in sicurezza del sistema in caso di sovrapressione.

Segue la progettazione del sistema di compressione. Questo elemento dell'impianto è costituito da un compressore e da diverse valvole pneumatiche air-to-open per regolare le condizioni di apertura e chiusura delle linee. Questa sezione svolge due scopi. Poiché la pressione di lavoro a monte del sistema di separazione varia tra 1,3

e 1,7 bar, il compito principale del compressore è quello di comprimere il gas prima che fluisca nel serbatoio (fase di accumulo). In secondo luogo, funge da booster del gas durante la fase II di separazione. La scelta del compressore deve tener conto di diverse esigenze. Innanzitutto, la composizione della miscela da comprimere cambia istantaneamente durante la fase di accumulo. Infatti, il gas in aspirazione, assumendo di trovarci in fase di filling, sarà puro in CO_2 nelle prime ore e puro C_4F_{10} nelle ore di finali. In entrambi gli scenari emergono importanti problematiche. A una pressione di 7 bar, il C_4F_{10} condensa a circa 62 °C (Fig. 4.9). Pertanto, potrebbe essere necessario preriscaldare il gas a monte dell'aspirazione per evitare la formazione di liquido all'interno della macchina volumetrica. Tuttavia, questa convalida deve essere fatta sperimentalmente. Quando, invece, la miscela è CO_2 quasi pura, si osserva un importante riscaldamento (Fig. 4.10). In questo caso è necessario un inter-raffreddamento per evitare di alimentare gas eccessivamente caldo nel serbatoio. Il compressore scelto (Tab. 4.6) non include un sistema di inter-raffreddamento in quanto è si è deciso di porre maggiore enfasi sulla problematica della condensazione.

Progettazione del Doppio Stadio di Equilibrio (DSE)

Il sistema in esame (Fig. 4.11) è costituito da due stadi di equilibrio operanti a diverse condizioni termiche. Il primo stadio funge da condensatore parziale, mentre il secondo evapora parzialmente il condensato derivante dal primo stadio. La miscela in uscita dal serbatoio di accumulo viene raffreddata e parzialmente condensata attraverso uno scambiatore di calore a piastre. La temperatura operativa è cruciale per la purezza e la resa del prodotto. Il vapore residuo viene eliminato in testa, mentre la corrente di condensato in uscita dal primo stadio viene controllata da un trasmettitore di livello e una valvola di regolazione. Giunto al secondo serbatoio, il liquido, viene vaporizzato parzialmente tramite una resistenza elettrica. Il liquido residuo rappresenta il prodotto finale, mentre il vapore viene ricircolato a monte dello scambiatore ed unito alla corrente di alimentazione fresca. Le condizioni termiche influiscono sulla qualità del prodotto e sulla magnitudine del ricircolato. La sicurezza del processo è garantita da valvole di sicurezza e sensori in continuo monitoraggio dei parametri di processo. Una descrizione più dettagliata è presente in sezione 4.4.

Comprendere le condizioni di alimentazione è fondamentale prima di procedere con la progettazione dei sistemi di recupero. Dato che l'alimentazione (F) proviene dal serbatoio di stoccaggio, lo stato della miscela all'interno del serbatoio definisce

la composizione del flusso stesso. Tuttavia, non è possibile prevedere quale sia la composizione alla fine del periodo di accumulo. La composizione dell'alimentazione deve quindi essere stimata. A partire dai dati riguardanti il flusso alimentato e la percentuale in volume di C_4F_{10} durante la fase di riempimento del 2023 (Fig. 4.12) e, integrando le curve nel tempo, si ottengono delle curve cumulative utilizzate per la stima sia del volume effettivamente alimentato nel sistema sia della composizione del gas accumulato (Fig. 4.13). Il volume nominale ottenuto (V_s, Eq. 4.5) è di 16.2 m^3 (prossimo ai 16 m^3 dichiarati in precedenza) mentre la frazione molare di C_4F_{10} (Z_s, Eq. 4.6) risulta 0.769.

La scelta della temperatura operativa dei due stadi è la variabile che ha il maggior impatto sull'efficienza del sistema. In generale, un aumento della temperatura per una data composizione in ingresso comporta: (1) Un aumento del flusso di gas e una diminuzione della portata di liquido; (2) Un aumento della purezza della fase liquida; (3) Una diminuzione della resa dovuta all'aumento della frazione di C_4F_{10} nel vapore esausto. Pertanto, la scelta delle condizioni operative ottimali è stata ottenuta attraverso una serie di simulazioni che seguono un algoritmo descritto in Figura 4.14. In breve, si fissa la temperatura del primo stadio (T1) in modo da garantire un recovery in C_4F_{10} superiore al 98% in assenza di ricircolo (Eq. 4.7). In seguito, il secondo ciclo dell'algoritmo è forzato aggiungendo la corrente di ricircolo. I risultati di questa analisi, condotta utilizzando Aspen Plus, sono visibili nelle Figure 4.15 e 4.16. Da queste si nota che all'aumentare di T1: (1) Si verifica un aumento di portata dell'esausto; (2) Un aumento della frazione molare di decafluorobutano sia nel vapore che nel liquido uscente dal primo stadio. Ne consegue un aumento di purezza del liquido residuo a discapito di una maggiore perdita di prodotto attraverso l'esausto.

In seguito, sono stati studiati gli effetti della temperatura del secondo serbatoio (T2) sulla qualità del prodotto finale e sull'entità del ricircolo. Ciò è stato fatto variando T2 e mantenendo costante il valore T1 (-35, -40 e -45 °C). Le simulazioni mostrano che un aumento di T2, a parità di T1, migliora la purezza del prodotto finale, ma comporta incremento della portata ricircolata, soprattutto sopra 10°C, dove tale crescita assume un andamento esponenziale. Inoltre, a parità di T2, minore è T1 tanto maggiore è il tasso crescita esponenziale. D'altra parte si osserva un aumento di produttività, espressa come portata molare di liquido in uscita dal fondo del secondo stadio. infine, è evidente che la qualità del prodotto è principalmente influenzata da T2. Queste affermazioni sono evidenti nelle Figure 4.17 e 4.18. Per concludere, le

condizioni operative scelte (Tab. 4.8) sono state ottimizzate per massimizzare sia la resa che la purezza del decafluorobutano, anche se richiedono costi energetici e di investimento iniziale maggiori.

Progettazione della Colonna di Distillazione (DC)

Una delle tecniche di separazione più utilizzate nell'industria di processo è la distillazione. All'interno di una colonna di distillazione, avviene un trasferimento di materia tra una fase liquida e una fase di vapore che si muovono in controcorrente al fine di arricchire il vapore dei componenti più volatili e il liquido delle specie più pesanti. Il processo di separazione è facilitato quando la volatilità relativa dei componenti da separare è elevata. Una colonna di distillazione è composta da tre elementi chiave: (1) Ribollitore, uno scambiatore di calore che consente la vaporizzazione continua del liquido di fondo colonna. Una parte del liquido viene estratta come prodotto, mentre la frazione restante viene vaporizzata e reimmessa in colonna (vapore di ricircolo); (2) Condensatore, uno scambiatore di calore collegato a un serbatoio (drum di riflusso) dove il vapore di testa viene completamente o parzialmente condensato. La corrente in uscita dal condensatore si divide in distillato e riflusso. Il rapporto tra riflusso e distillato (RR) è una metrica significativa; (3) Colonna, è l'elemento strutturale principale del sistema e serve a massimizzare l'area di contatto tra le due fasi, garantendo una maggiore capacità di scambio di materia e calore. A tale scopo gli interni delle colonne sono altamente ingegnerizzati e possono essere suddivisi in colonne a piatti o colonne a riempimento.

L'equilibrio liquido-vapore (sezione 3.1) è alla base del processo di distillazione. Ogni piatto in una colonna può essere assimilato a uno stadio di equilibrio teorico (Figura 4.20) e per ogni stadio e componente si possono definire quattro equazioni fondamentali (Equazioni MESH: Bilancio di massa, Equilibrio, Sommatoria e Bilancio di calore) [15]. I metodi rigorosi per il design o il rating delle colonne sono costruiti a partire da queste equazioni. Tuttavia, la stima delle temperature in ciascuno stadio richiede il calcolo delle temperature di ebollizione del liquido e di condensazione del vapore. In queste condizioni, è necessario saturare un numero di gradi di libertà pari al numero di componenti più sei al fine di definire il problema in modo univoco (Tabella 4.9).

Nel caso in esame, questi parametri sono la composizione, la portata e le condizioni termiche dell'alimentazione. Con queste informazioni, al fine di saturare i

gradi di libertà, è necessario fissare altri parametri chiave. La scelta delle variabili da fissare rimane in parte arbitraria e dipende dagli obiettivi e dalle specifiche stabilite. In questo progetto, gli obiettivi principali sono: (1) massimizzare la purezza del prodotto di fondo e (2) ottenere il massimo recovery possibile. Per queste ragioni, è utile fissare, oltre alla pressione in testa alla colonna, la portata di fondo della colonna, o più precisamente, il cosiddetto rapporto fondo/alimentazione (B/F). Infatti, assumendo che sia possibile ottenere un prodotto di fondo puro, fissare un B/F uguale alla portata del prodotto di alimentazione è una scelta saggia, in quanto si otterrà anche un recupero del 100%. Inoltre, sono stati fissati valori di primo tentativo per il rapporto di riflusso e per il numero di stadi teorici e, iterativamente, si è giunti ai loro valori ottimali.

Si descrivono ora le scelte fatte in termini quantitativi. La pressione operativa svolge un ruolo chiave nel processo. In generale, una pressione più elevata rende la separazione più complessa. Aumentare la pressione fa sì che le linee di rugiada e di ebollizione descritte nei diagrammi binari (Sezione 4.1) si avvicinino l'una all'altra. Inoltre, in applicazioni come questa, in cui le temperature di transizione a pressione atmosferica sono al di sotto di zero gradi Celsius, operare a basse pressioni comporta costi energetici elevati. Pertanto, viene fissato un valore iniziale di circa 2,5 bara. Questa scelta consente di condensare il distillato a circa -70°C e vaporizzare il prodotto di fondo a circa 20°C. Il rapporto B/F viene fissato pari alla frazione molare di C_4F_{10} nell'alimentazione. Il numero di stadi di equilibrio (N) e il rapporto di riflusso (RR) sono determinati in modo iterativo. Si fissa il numero di stadi e si fa variare il rapporto di riflusso osservando l'impatto di questa analisi sulla purezza e sul recupero del decafluorobutano. I risultati di questa analisi di sensitività sono riportati nelle Figure da 4.21 a 4.24.

A questo punto è importante fare una breve digressione. Il sistema deve essere in grado di gestire sia la fase di filling che quella di emptying. Mentre la composizione durante la fase di riempimento è stata ampiamente discussa, per la gestione della fase di svuotamento, è necessario assumere che la composizione della miscela da trattare sia simmetrica rispetto a quella della fase di riempimento. Pertanto, verrà utilizzata una miscela in ingresso con una frazione molare del 24% di decafluorobutano. Di conseguenza è necessario che: (1) il numero di stadi scelto (come variabile non modificabile una volta costruita la colonna) sia sufficiente a soddisfare le specifiche nel peggiore dei due casi e (2) il B/F e il RR cambino a seconda del caso.

La selezione del numero di stadi di equilibrio viene ora descritta al fine di soddisfare le seguenti specifiche: (1) purezza maggiore del 99,9% mol e (2) Recovery maggiore del 99,5 %. Dalle Figure da 4.21 a 4.24, è evidente che la purezza e il recupero aumentino con il numero di stadi e il rapporto di riflusso. In particolare: (1) Nella fase di svuotamento (Figure 4.21 e 4.22), la dipendenza della purezza e del recupero dal numero di stadi diminuisce all'aumentare di quest'ultimo. In altre parole, non vi è alcun miglioramento delle prestazioni per un numero di stadi superiore a 5. Inoltre, fissato il numero di stadi, l'uso di un rapporto di riflusso superiore a 3 non comporta cambiamenti significativi. Infatti, le curve raggiungono un asintoto orizzontale. (2) Nella fase di riempimento (Figure 4.23 e 4.24) si osservano tendenze simili. L'unica differenza è che la curva associata a un numero di stadi pari a 4 tende a sovrapporsi alle curve di 5 e 6 stadi quando il rapporto di riflusso supera un valore di 4. Risulta evidente che aumentare indefinitamente N e RR è la scelta migliore. Tuttavia, è importante considerare che: (1) un aumento del numero di stadi comporta costi capitali maggiori e (2) un aumento del rapporto di riflusso comporta un maggiore consumo di energia e, di conseguenza, costi operativi più elevati. Presumendo che il numero di stadi non abbia un impatto significativo sui carichi degli scambiatori di calore, è chiaro che (Figure 4.25 e 4.26) esiste una relazione lineare tra il rapporto di riflusso e la potenza termica da fornire o sottrarre. Per tali ragioni si fissare un numero di stadi a 5 e un rapporto di riflusso (teorico) pari a 3. Per garantire un corretto funzionamento, è stato deciso di aumentare il rapporto di riflusso a 4 mediante l'aggiunta di un fattore correttivo. Le Tabelle 4.10 e 4.11 riassumono i risultati delle simulazioni.

Mentre le ragioni alla base della selezione ottimale dei parametri liberi sono state discusse ampiamente, il nucleo della simulazione non è stato ancora approfondito. Per cui si passa al dimensionamento e all'ottimizzazione della colonna con riferimento alla fase di riempimento. I passaggi effettuati per la fase di svuotamento sono gli stessi. Prima di tutto, si definiscono sia le condizioni in ingresso (Tabella 4.12) sia: (1) il tipo di condensatore, (2) il profilo idraulico e di caduta di pressione all'interno della colonna e (3) il punto di alimentazione. Per quanto riguarda il tipo di condensatore, si opta per un condensatore parziale poiché non c'è bisogno di condensare completamente il vapore di testa. Questa scelta comporta anche una riduzione del carico termico rimosso dal fluido refrigerante. Il profilo idraulico e di caduta di pressione è inizialmente supposto variare costantemente, con una perdita di carico di 50 mbar tra il punto di iniezione e la pressione in cima alla colonna.

Infine, il punto di alimentazione che influisce sulle prestazioni di separazione è scelto mediante un'analisi di sensitività. I risultati di questa analisi sono riportati in Tabella 4.13. La scelta ottimale è alimentare esattamente a metà della colonna. In questo caso, assumendo che la colonna sia adiabatica, i carichi termici del ribollitore e del condensatore sono rispettivamente di 60,02 W e -297,02 W. Inoltre, i profili termici, di pressione e di composizione lungo la colonna sono riportati nelle Figure 4.27 e 4.28.

Come si può vedere dalla Figura 4.27, la temperatura di condensazione parziale della miscela è molto bassa, specificamente -66,84 °C. Questa condizione impone un grande vincolo operativo. Infatti, l'anidride carbonica, intorno a questa temperatura, subisce una transizione solido-vapore. La possibilità di solidificazione rappresenta un rischio in quanto potrebbe portare a una riduzione parziale dell'area di scambio termico nel condensatore e, nel peggiore dei casi, ad una completa ostruzione. Per cui, è necessario mantenere una temperatura del condensatore superiore alla temperatura di transizione solido-vapore della CO_2 pura alla pressione in testa alla colonna. Adattando i dati sperimentali [16], è possibile determinare la temperatura di solidificazione. La Figura 4.29 mostra la variazione della pressione di transizione solido-vapore e l'errore quadratico tra i dati sperimentali e i risultati della regressione. Ulteriori informazioni sono disponibili nell'Appendice C. Risulta che, a una pressione di 2,45 bar, la temperatura di transizione solido-vapore è -66,61 °C. Pertanto, per garantire un margine di sicurezza, si impone un minore carico frigorifero al condensatore (al posto di RR). La scelta del carico influisce sui risultati della simulazione. Nella Figura 4.30, è evidente che una minore rimozione di calore porta a prestazioni inferiori. Fortunatamente, grazie alla piccola variazione richiesta, purezza e recupero non sono significativamente influenzati da questa modifica. In sintesi, i parametri liberi fissati sono i seguenti: (1) Pressione in testa a 2,45 bar; (2) Numero di stadi teorici fissato a 5; (3) Alimentazione al quarto stadio teorico; (4) Rapporto B/F fissato a 0,75; e (5) Carico del condensatore parziale fissato a -288,7 W (a cui corrisponde una temperatura del condensatore di -60°C).

La prima considerazione per dimensionare l'apparecchiatura è la scelta del tipo di colonna. In questa applicazione, date le modeste portate in gioco, è stato deciso di procedere con una colonna a riempimento. Gli step utilizzati sono: (1) Scegliere un diametro e determinare le portate specifiche di vapore e liquido; (2) Scegliere un tipo di riempimento e analizzare i profili idraulici e termici della colonna; (3) Calcolare le perdite di carico, verificare l'efficienza del riempimento alle condizioni

idrauliche date e determinare l'altezza della colonna. Il diametro della colonna (D_c) è stato fissato a 3 centimetri, e le portate volumetriche specifiche della fase liquida (V_s^l), della fase di vapore (V_s^v) e il fattore caratteristico del riempimento (F-factor) vengono determinati utilizzando le Equazioni da 4.12 a 4.14. Successivamente, viene selezionato un riempimento appropriato. In generale, il materiale solido interno mira a massimizzare l'interfaccia tra le due fasi fluide [17], [18]. Le principali caratteristiche includono le dimensioni del riempimento (d_p), la frazione di volume vuoto (V_{void}) e l'area specifica (a_p). Data una geometria del riempimento, la riduzione delle sue dimensioni porta ad un aumento dell'area specifica e ad una diminuzione della frazione di vuoto. Inoltre, in condizioni costanti dal punto di vista fluidodinamico (valori costanti del fattore F e della portata di liquido), aumentando l'area specifica si osserva un miglioramento delle prestazioni, mentre la riduzione della frazione di vuoto porta ad un aumento delle perdite di carico. Pertanto, la scelta deve essere un compromesso tra efficienza e perdite di pressione.

In virtù di ciò, si è scelto di utilizzare riempimenti strutturati di laboratorio DX (figura 4.31) di Sulzer Chemtech AG, le cui proprietà e curve caratteristiche sono rispettivamente presentate nella Tabella 4.14 e nelle Figure 4.32 e 4.33. La Figura 4.32 mostra HETP/m in funzione del F-factor. Questo grafico può essere considerato una delle specifiche di progettazione più importanti. Infatti, il numero di stadi teorici (N) e il valore di HETP/m sono utilizzati per determinare l'altezza del letto di riempimento (Z). Per fare ciò, è necessario: (1) Scegliere un valore di partenza (ragionevole) della perdita di carico; (2) Valutare l'F-factor; (3) Trovare il valore corrispondente di HETP dalla Figura 4.32; (4) Calcolare l'altezza totale del riempimento come somma di HETP utilizzando l'Equazione 4.15. In seguito, utilizzando la Figura 4.33 e gli stessi valori del F-factor, è necessario calcolare, nello stesso modo, le perdite di carico per metro di colonna. Infine, è possibile calcolare la perdita di pressione totale (ΔP) come somma delle perdite di pressione per metro ($\Delta P/Z$) moltiplicata per l'altezza totale del letto di riempimento (Z) (Eq. 4.16).

Questo processo deve essere eseguito iterativamente poiché l'F-factor è una funzione della velocità e della densità del gas, che a loro volta dipendono dalla pressione. Fortunatamente, il simulatore Aspen Plus è in grado di eseguire questa iterazione semplicemente selezionando l'opzione di aggiornamento delle perdite di pressione (impostando la pressione iniziale a 2,45 bara). Quindi, vengono inserite le caratteristiche del materiale di riempimento scelto (Tabella 4.14) e si calcola un valore medio del F-factor. Successivamente, viene selezionato un valore di HETP

dalla regione blu nella Figura 4.32. In particolare, il valore medio calcolato del F-factor è 0,82, che corrisponde a un HETP di circa 0,05-0,07 m^{-1}. Con queste informazioni, viene avviata la simulazione finale e si ottengono i risultati mostrati nelle Tabelle da 4.15 a 4.17. Pertanto, l'altezza totale teorica del riempimento (Z) risulta di 0,21 m. Per stimare l'altezza totale della colonna, è necessario fare le seguenti considerazioni [19]: (1) Aumentare l'altezza teorica trovata per tenere conto degli errori di simulazione e garantire un margine di sicurezza. In questo caso, si è deciso di raddoppiarla a 0,4 m; (2) Aumentare ulteriormente l'altezza per garantire una distribuzione adeguata del liquido in discesa e del gas in salita. Pertanto, si applica un ulteriore aumento del 25% ottenendo un'altezza totale del riempimento di 0,5 m; (3) Garantire spazio aggiuntivo per il distributore di liquido, il supporto per il riempimento e potenziali coni di redistribuzione. Si stima un'altezza aggiuntiva di 0,1 metri per la colonna.; (4) L'altezza relativa all'hold-up di liquido viene calcolata impostando un tempo di residenza e moltiplicandolo per la portata di liquido "in uscita" dal quarto stadio. Ciò restituisce un volume di liquido, che, diviso per la sezione trasversale della colonna, porta a un'altezza di 0,28 m; (5) Infine, assumere 0,3 metri sopra il riempimento per l'ingresso del liquido e il trascinamento di eventuali particelle liquide, e una quantità uguale al di sotto del riempimento per garantire l'uniformità del flusso di vapore proveniente dal ribollitore. In sintesi, si avranno 0,6 metri per la zona di riempimento e ulteriori 0,9 metri per la zona libera, per un'altezza totale (trascurando la testa e i fondi bombati) di 1,5 metri.

Una volta che la colonna è stata completamente dimensionata, si procede con il condensatore, in cui il flusso in ingresso è costituito dal vapore proveniente dal secondo stadio e i flussi in uscita sono il distillato e il riflusso. Le condizioni di temperatura, composizione e portata sono presentate nella Tabella 4.18. Uno schema semplificato è mostrato nella Figura 4.34. Note le condizioni in ingresso e le specifiche in uscita, si imposta una simulazione "shortcut" con le seguenti caratteristiche: (1) Il fluido refrigerante utilizzato è etanolo (usato nella macchina termica acquistata) a -80°C e 1 bar; (2) La temperatura di "pinch", essendo uno scambio gas-liquido, è fissata a 20°C; (3) Il coefficiente globale di scambio termico (U) è impostato a 340 (W/m^2K) [19]. L'obiettivo è raggiungere le condizioni termiche specificate dei flussi di distillato e riflusso come indicato nella Tabella 4.18. L'area di scambio termico richiesta è di 0,02 m^2 quando la portata del refrigerante è di 0,7 kmol/h. In realtà, lo scambiatore di calore selezionato è stato significativamente sovradimensionato per accomodare non idealità e future possibili espansioni, e il

dimensionamento finale è stato gestito direttamente dal produttore [20]. Infine, nota la portata di riflusso e assumendo un tempo di residenza del liquido di 15 minuti (τ_{RD}) nel serbatoio del riflusso, è possibile calcolare il volume occupato dal liquido in condizioni nominali. Supponendo che il volume del liquido occupi, in condizioni nominali, circa il 30% del volume totale disponibile, il serbatoio di riflusso viene dimensionato utilizzando le Equazioni 4.17 4.18 (impostando il diametro interno del serbatoio uguale al diametro nominale della flangia di chiusura). Le dimensioni e la geometria del serbatoio del riflusso sono riportate nella Figura 4.36. Il dimensionamento del ribollitore segue una procedura simile; per questa ragione i passaggi non saranno descritti. L'unica differenza è che, a causa della minore richiesta termica e di una temperatura di vaporizzazione vicina a 20°C, è stato deciso di semplicemente inserire una camicia riscaldata elettricamente. Le Figure 4.39 e 4.40 mostrano una foto e lo schema tecnico del ribollitore.

Terminato il design e l'ottimizzazione dei parametri di progetto si passa allo studio del comportamento dinamico della colonna. Per fare ciò, si deve prima definire un sistema di controllo idoneo. Un sistema di controllo svolge un ruolo cruciale per mantenere le variabili di processo ai loro valori stazionari. Ciò è essenziale per garantire non solo la qualità del prodotto ma anche la sicurezza stessa dell'impianto. Si viene ora alla descrizione della logica di controllo scelta per il sistema in questione. In seguito, utilizzando Aspen Dynamics, mostreremo gli effetti che le deviazioni nelle variabili di ingresso, come portata, temperatura e composizione dell'alimentazione, hanno sulle variabili di uscita, come la purezza del distillato e del prodotto di fondo.

Tra i loop di controllo, il più comune è il cosiddetto meccanismo a feedback. Il controllo a retroazione mira a mantenere una variabile di processo di uscita (PV) al valore di set point (SP) attraverso il seguente meccanismo: (1) Misurare la variabile di uscita in risposta a una perturbazione; (2) Confrontare questa variabile con il set point, derivando l'errore (ERR); (3) Inviare un segnale al sistema di controllo e all'attuatore (di solito espresso come OP poiché modifica la posizione di apertura di una valvola), che regola la variabile di ingresso per ridurre al minimo l'errore (definito dall'Equazione 4.19). In generale, la scelta di un sistema di controllo, deve garantire un compromesso tra prestazioni (velocità di risposta) e robustezza (la capacità di riportare il sistema al set point in modo stabile). In pratica, maggiore è il guadagno, più veloce è la risposta. Di contro, aumentare indefinitamente il guadagno porterebbe a un regime di risposta instabile. Ci sono quattro tipi di controllori a retroazione: (1) Controllore On/Off, utilizzato per manipolare variabili

che oscillano tra due stati; (2) Controllore Proporzionale (P), il quale comporta una risposta proporzionale alla deviazione della variabile di controllo (Eq. 4.20); (3) Controllore Proporzionale-Integrativo (PI), dove il termine integrale è usato per eliminare l'offset tipico di un controllore P, di contro esso rallenta il processo di smorzamento con cui la variabile di processo viene portata a set point (4.21); (4) Controllore Proporzionale-Integrativo-Derivativo (PID), usato quando la risposta di PI non è sufficientemente veloce. Infatti, il termine derivativo tiene conto del tasso di variazione (derivata) dell'errore e rende l'azione correttiva più rapida (4.22).

Dopo questa breve introduzione, è necessario: (1) Scegliere le variabili controllate e manipolate; (2) Selezionare i tipi di controllore e regolarne i parametri; (3) Testare la risposta del sistema a eventuali disturbi o variazioni del set point. Idealmente, un sistema di controllo efficace mira a garantire che le composizioni dei flussi in uscita dalla colonna siano costanti ed uguali ai valori di stato stazionario. Nella pratica, il controllo continuo della composizione presenta due problemi principali: il costo estremamente elevato dei sensori e la difficile gestione dovuta al ritardo intrinseco causato dai lunghi tempi caratteristici di tali sensori. Pertanto, si è optato per un sistema in grado di mantenere costanti le condizioni termodinamiche e un profilo termico il più vicino possibile allo stato stazionario. Nel caso preso in considerazione (Figura 4.42), è stato deciso di controllare le seguenti variabili: (1) Portata dell'alimentazione, misurata e regolata con flussimetro; (2) Il livello del liquido nel drum di riflusso e nel drum del ribollitore, grazie a sensori continui di livello (regolati rispettivamente da una valvola di regolazione e da un flussimetro); (3) La pressione in testa, misurata da un sensore e controllata regolando l'apertura di una valvola sulla linea del distillato; (4) Il profilo termico in colonna, monitorato da una serie di sensori di temperatura e mantenuto stazionario variando la potenza termica fornita dal ribollitore. Per informazioni più dettagliate si faccia riferimento alla sezione 4.5.6. Si noti che è stato deciso di non regolare la quantità di calore rimosso al condensatore. Al momento della stesura di questo testo, l'unità di refrigerazione non è ancora stata consegnata dal fornitore. Per questo motivo, si lascia aperta la possibilità di modificare la struttura di controllo in futuro.

Stabilita la logica di controllo, si selezionano i singoli controllori e i relativi parametri di tuning. Il tuning è stato fatto utilizzando il software Aspen Dynamics, che consente di creare simulazioni transitorie, regolare diverse strutture di controllo e, soprattutto, verificare la capacità del sistema di rispondere a disturbi esterni. I parametri dei controllori sono elencati nella Tabella 4.19. Tali valori sono stati

determinati tramite tuning ATV [22] o aumentando manualmente il guadagno fino al limite di instabilità. Per verificare il loop di controllo, sono state condotte una serie di simulazioni dinamiche in risposta a disturbi esterni. In particolare, sono stati simulati i seguenti scenari: (1) Aumento della temperatura della miscela in ingresso (da 25 a 35°C); (2) Due variazioni nella composizione dell'alimentazione. Nel primo caso, è stata presa in considerazione una miscela più povera in C_4F10 rispetto alle condizioni nominali (frazione molare da 0,769 a 0,6). Nel secondo caso, è stata considerata una miscela più ricca (frazione molare da 0,769 a 0,9); (3) Variazione del flusso molare in ingresso da 50 a 60 mol/h.

Analizziamo l'effetto di un aumento dell'entalpia della miscela in ingresso. Il disturbo viene introdotto nel sistema nella quarta ora della simulazione. Nella Figura 4.43, si osserva che un aumento della temperatura dell'alimentazione comporta un aumento della pressione e della temperatura nel piatto pilota (corrispondente al secondo stadio teorico, dove il salto termico è molto pronunciato). I controllori rispondono aprendo la valvola sulla linea del distillato e riducendo la potenza termica fornita al ribollitore. Il sistema ritorna rapidamente e stabilmente a un nuovo stato stazionario. Nella Figura 4.44 si osserva che le variazioni di livello nel ribollitore e condensatore sono trascurabili. In ogni caso, la risposta del sistema è stabile. D'altra parte, la Figura 4.45 mostra le variabili chiave. Si nota che la purezza e le portate di distillato e prodotto di fondo variano di pochi punti percentuali. La figura a destra evidenzia un leggero aumento della quantità di decafluorobutano perso nella fase di vapore. In altre parole, si verifica una piccola riduzione del recupero. In generale, si può affermare che il sistema funziona bene in risposta a una perturbazione termica in ingresso.

La seconda perturbazione testata è una diminuzione della frazione molare di C_4F_{10} nell'alimentazione. La Figura 4.46 evidenzia una variazione significativa della pressione in testa a causa di un aumento della volatilità media della miscela e una improvvisa diminuzione della temperatura del piatto pilota. In risposta alla perturbazione, la valvola sulla linea del distillato viene aperta, e si osserva un aumento della potenza termica fornita al ribollitore (per riportare la temperatura al valore di set point). Il sistema torna a un nuovo stato stazionario. In riferimento alla Figura 4.47, la variazione di livello è, in questo caso, più pronunciata. Nonostante ciò, la risposta è stabile e abbastanza veloce. La Figura 4.48 mette in luce come la purezza del prodotto di fondo sia migliore rispetto al caso nominale. Nonostante l'aumento del flusso di distillato, l'effetto dell'aumentata purezza ha un impatto

maggiore. Questo fenomeno è evidente osservando la diminuzione della quantità C_4F_{10} perso. In sintesi, il sistema risponde bene quando la miscela in ingresso è arricchita di anidride carbonica. Ciò era già stato evidenziato nella Sezione 4.5.3, in cui è stata discussa la performance del sistema durante le fasi di riempimento e svuotamento. La terza perturbazione testata è un aumento della frazione molare di C_4F_{10} nell'alimentazione. Le Figure 4.49 e 4.50 mostrano il comportamento dei dispositivi di controllo a seguito delle perturbazioni. In questo caso, è stata introdotta una perturbazione alla seconda ora (frazione molare di C_4F_{10} passa da 0,769 a 0,85) e una seconda perturbazione alla quarta ora (da 0,85 a 0,90). La Figura 4.51 mostra come la purezza del prodotto di fondo peggiori. Fortunatamente, la riduzione del flusso di distillato compensa parzialmente l'aumento della quantità di decafluorobutano perso. In effetti, il comportamento del sistema è diametralmente opposto a quanto visto nel caso precedente.

Infine, ci si chiede quale potrebbe essere la risposta del sistema a seguito di una richiesta di aumento della produttività. In altre parole, si desidera studiare il comportamento della colonna a seguito di un aumento della portata alimentata. Per cui, si impone un aumento del flusso da 50 a 55 mol/h (terza ora di simulazione) e da 55 a 60 mol/h (settima ora). Una maggiore quantità di fluido in colonna comporta un leggero aumento della pressione e un aumento sostanziale della temperatura. In pratica, poiché non è possibile controllare il calore rimosso dal condensatore, l'unico modo per ridurre la temperatura della colonna è ridurre la potenza termica generata dal ribollitore (grafico a destra della Figura 4.52). L'incapacità del sistema di ripristinare un profilo termico è la ragione per cui non è possibile stabilire un nuovo stato stazionario che consenta di raggiungere specifiche vicine ai valori nominali. Questo fenomeno è molto evidente nella Figura 4.55. È chiaro che nel tempo il profilo termico tende verso una linea piana. Con entrambe le unità termiche inattive, il sistema raggiunge uno stato di equilibrio in cui la colonna raggiunge la stessa temperatura della miscela in ingresso. In particolare, più bassa è l'inerzia termica del sistema, più rapido sarà questo meccanismo di appiattimento.

In conclusione, le simulazioni indicano che un sistema di controllo basato sulle logiche precedentemente descritte si comporta in modo stabile di fronte a varie perturbazioni imposte dall'esterno. Sulla base di questi risultati, è in atto la stesura logica di controllo che verrà implementata in collaborazione con i membri del team gas EP-DT-FS del CERN.

Contents

List of Figures

List of Tables

Nomenclature

Roman Symbols

A_c Column cross section area (m^2)

a_p Specific surface area of the packing (m^2/m^3)

B Bottom molar flowrate (mol/s)

B/F Bottom to Feed molar ratio

C_{s1} First fitting constant for evaluation of P_{ss}

C_{s2} Second fitting constant for evaluation of P_{ss}

C_{s3} Third fitting constant for evaluation of P_{ss}

D Distillate molar flowrate (mol/s)

D_c Column internal diameter (m)

D_{RD} Internal diameter of the reflux drum (m)

F Feed Molar Flowrate (mol/s)

H Enthalpy associated to the vapor stream (J/mol)

h Enthalpy associated to the liquid stream (J/mol)

H_{RD} Height of the reflux drum (m)

$HETP$ Height Equivalent to Theoretical Plate ($1/m$)

J Enthalpy associated to the feed stream (J/mol)

k_g Correction factor taking into account the non-ideality of the gas mixture

k_T Correction factor taking into account specific volume variation with temperature

L_{C4F10} Quantity of C_4F_{10} lost

$Lost_I$ Mass of C_4F_{10} lost during *Filling I* Phase (kg)

$Lost_{II}$ Mass of C_4F_{10} lost during *Filling II* Phase (kg)

N Number of equilibrium stages

N_c Number of components

N_p Number of Experimental Data Points

N_{hours} Total number of operating hours of the filling process

P Pressure (bar)

P_s Vapor pressure (bar)

$P_s^{SV}(T)$ Experimental saturation pressure of solid CO_2 ($kPa5$

P_{C4F10} N-decafluorobutane purity specification

P_{op} Operative Pressure of the Accumulation Tank ($bara$)

Q Heat flux exchanged between the system and the surroundings (J/s)

R Reflux flowrate (mol/s)

R_R Reflux Ratio

R_{C4F10} N-decafluorobutane recovery specification

Rec_I Mass of C_4F_{10} recovered during *Filling I* Phase (kg)

Rec_{II} Mass of C_4F_{10} recovered during *Filling II* Phase (kg)

T Temperature (K)

T_{op} Operative Temperature of the Accumulation Tank (K)

U Overall heat transfer coefficient (W/m^2K)

V_D Design Volume of the Accumulation Tank (m^3)

V_i Volumetric flowrate during the i^{th} hour of the filling

V_m Specific molar volume of the mixture (m^3/mol)

V_n Required volume of the accumulation tank at normal condition (Nm^3)

V_s Specific volumetric flow rate $(m^3/s/m^2)$

V_{reflux} Volume of the liquid in the reflux drum in nominal conditions (m^3)

V_{void} Void fraction espressed as the % of the column volume free from solids $(1/m)$

x Molar Fraction in Liquid Phase (mol/mol)

x_i % in volume of C_4F_{10} in the tank during the i^{th} hour of the filling

y Molar fraction in vapor phase (mol/mol)

Z Total height of the packing bed (m)

z Molar Fraction of the Feed (mol/mol)

c Molar Concentration (mol/m^3)

L Liquid Molar Flowrate (mol/s)

r Free Geometric Path (m)

Greek Symbols

$\Delta P/Z$ Pressure drops per meter of column height $(mbar/m)$

ΔP Total pressure drop along the packing bed $(mbar)$

ε_c Molar Extinction Coefficient (m^2/mol)

ε_t Threshold on n-decafluorobutane lost after first liquefaction stage

η_I Efficiency of the *Filling I* Phase

η_{II} Efficiency of the *Filling II* Phase

γ Chemical activity coefficient

μ Chemical Potential

ω General Data point

Φ Chemical fugacity factor

ϕ Chemical fugacity coefficient of a species in the mixture at [T,P]

ϕ_{sat} Chemical fugacity coefficient of a species in the mixture at saturation condition

ρ Density (kg/m^3)

τ_{RD} Residence time of the reflux in the reflux drum (s)

Superscripts

exp Experimental Data superscript

id Superscript indicating ideal condition

l Liquid phase superscript

$model$ Model Retrieved Data superscript

v Vapor phase superscript

Subscripts

j Component Index

j Indicates the j^{th} component in the mixture

n Indicates the n^{th} stage of equilibrium

Acronyms / Abbreviations

$ATPS$ Accumulation Tank and Pumping Station subsystem

$CFRP$ Carbon Reinforced Polymer

DC Distillation Column recovery subsystem

DSE Double Stage Equilibrium subsystem

ECAL Electromagnetic Calorimeters

EOS Equation of State

ERR Process Error (SP+-PV)

GC Gas Cromatograph

HCAL Hadron Calorimeters

HOC Hayden-O'Connel

LBL Lambert-Beer Law

LHC Large Hadron Collider

NRTL Non Random Two Liquids

OP Opening Position of a valve

PLC Programmable Logic Controller

PR Peng-Robinson

PS Proton Synchrotron

PSB Proton Synchrotron Booster

PV Process variable

RICH Ring Imaging Cherenkov Detector

RK Redlich-Kwong

RMSD Root Mean Square Deviation

RMSE Root Mean Square Error

SG Surface Room

SP Set Point variable

US Service Room

UX Experimental Cavern

$VELO$ Vertex Locator

VLE Vapor Liquid Equilibrium

Chapter 1

CERN, Accelerating Science

1.1 Introduction to CERN

The European Center for Nuclear Research, or CERN, was founded in 1954 and it is the most significant entity in Europe for studies concerning particle physics. CERN is situated near Geneva, close to the Swiss-French border. In particular, it hosts the Large Hadron Collider (LHC) and other accelerators designed to collide protons beams. By colliding antiparallel high-energy and high-intensity beams, LHC allows deep understanding of phenomena that occurred during the birth of the Universe. The CERN complex is massive and it begins with the Linear Accelerator, or LINAC, which speeds up primary protons. In order to be ready to enter the Proton Synchrotron Booster (PSB), where the negative hydrogen is stripped off its electrons and is left with only protons, these protons must reach an energy level of 160 MeV. The PSB steps up protons energy up to the 2 GeV needed for the next accelerator, the Proton Synchrotron (PS), where protons travel up to 26 GeV. They are then introduced into the Super Proton Synchrotron (SPS), where they undergo a speed increase up to 450 GeV. The LHC's two beam pipes, one of which rotates clockwise and the other counterclockwise, are then used to deliver the protons. There, they circulate inside the LHC for many hours until they achieve their maximum energy of 6.5 TeV. Here the two beams are brought into collision inside four specific points of the ring: ALICE, ATLAS, CMS, and LHCb.

1.2 LHCb - Large Hadron Collider Beauty

One of the four studies being run in the LHC at CERN is LHCb. The LHCb detector is 21 meters long, 10 meters high, and 13 meters wide, and it is located 100 meters underground, close to the French town of Ferney-Voltaire (Figure 1.1). By examining entities known as "beauty quarks" or "b quarks" the LHCb experiment seeks to understand the distinctions between matter and antimatter. The relevance of these experiments originates not only from interest in elementary particle physics, but also from cosmology, which seeks to explain the dominance of matter over antimatter witnessed in our universe [1]. LHCb is a single-arm spectrometer divided into several subsystems:

- The Vertex Locator (VELO) is built around the proton interaction region. It is used to precisely identify the points of interaction of the protons (primary vertex) and of decaying of the mesons (secondary vertex). The system consists of two detector planes (TT) placed before a dipole magnet, and three planes placed in series with the latter (T1, T2 and T3). The planes guarantee a measurement of the trajectory of the charged particles and of their momentum thanks to the curvature induced by a magnetic field.

- The Ring Imaging Cherenkov Detectors (RICH) [2] system has the task of identifying charged particles over the momentum range of 1-150 GeV/c. The system consists of an upstream detector (RICH-1) with silica aerogel and C_4F_{10} gas radiators, and a downstream detector (RICH-2) with a CF_4 gas radiator, located behind the magnet and the tracking system. Due to its extremely low density and high refractive index, a silica aerogel is used because it is suitable for the detection of low momentum particles (of the order of a few GeV/c). Fluorocarbons, on the other hand, can withstand larger momenta in absolute terms (10–65 GeV/c for C_4F_{10} and 15–150 GeV/c for CF_4). Particles produced during the collisions travel through the mirrors of RICH-1 prior to reaching measurement components downstream. To reduce scattering the mirrors are made of carbon-fiber reinforced polymer (CFRP), rather than glass. As RICH-2 is located downstream of the VELO-Magnet system, glass can be used without compromising measurements [24].

- The energy held by electrons, photons, and hadrons traveling through the detector can be detected by the Electromagnetic Calorimeters (ECAL) and

Hadron Calorimeters (HCAL). Muon detectors come next. They primarily consist of detection tracers with thick iron walls separating them to screen out any unwanted particles [3].

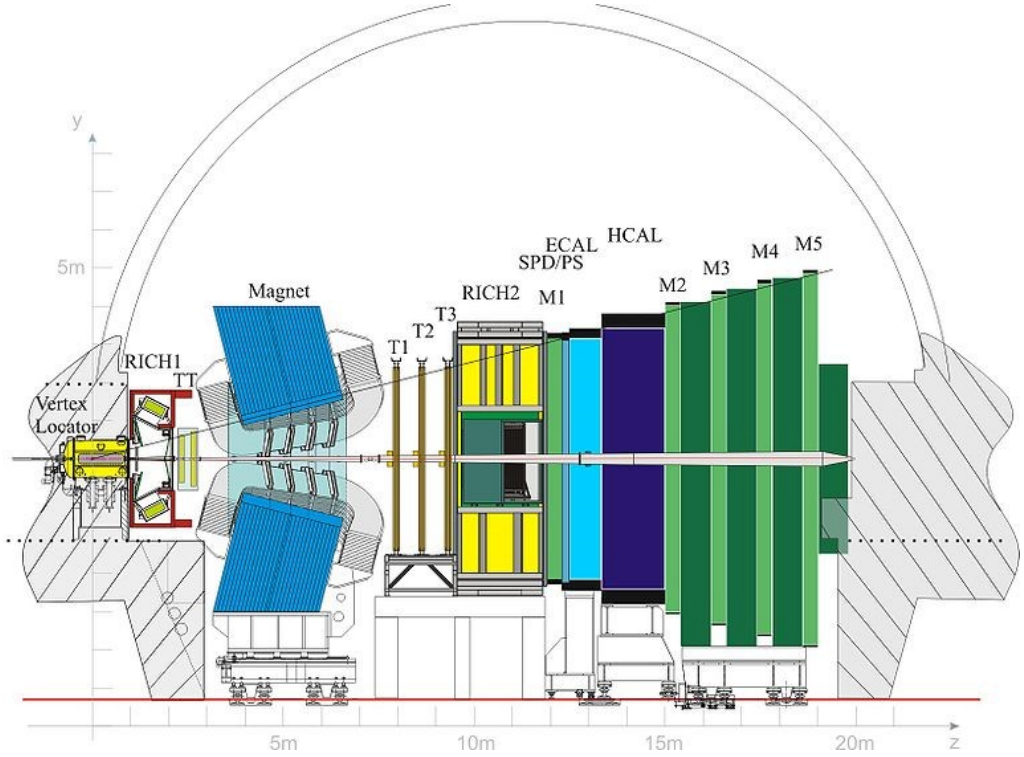

Fig. 1.1 LHCb's structure [1].

1.3 RICH-1 Detector

Figure 1.2 depicts the RICH-1's engineered construction, allowing all its components to be observed. The Cherenkov effect, for which a medium is polarized when crossed by charged particles (at a speed greater than the speed of light in the medium itself), produces electromagnetic radiation with a distinctive blue color, serves as the basis for the working theory. The spherical and flat mirrors in the RICH-1 reflect the particles produced by a charging track in the two C_4F_{10} radiators. After passing through the quartz glass, the reflected particles are at last picked up by the HDPs [4] [5].

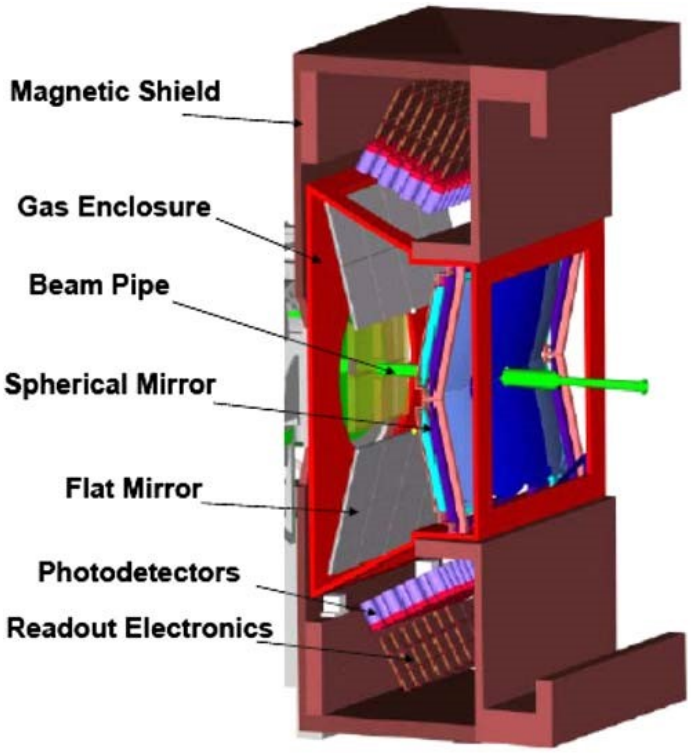

Fig. 1.2 RICH-1's structure and components [4].

One of the most crucial components of the entire device is the radiator. In order to determine which gas was best for experiments, numerous test beams have been conducted over the years. The following properties must be guaranteed by a satisfactory radiator:

- High and stable refractive index (up to 200 nm)
- Good trasparency
- Long radiation lenght

Among the numerous fluids tested, the n-Perfluorocarbon family satisfies the aforementioned characteristics. Based on the length of the carbon chain, this class of fluorinated hydrocarbons provides a wide range of refractive indices. In fact, it has been noted [6] that as the molecular weight of the tested molecule increases the refractive index n and the molar extincion coefficient ε_c growth (Fig 1.3). Given that, n-Decafluorobutane is a great trade-off between high refractive index and transparency.

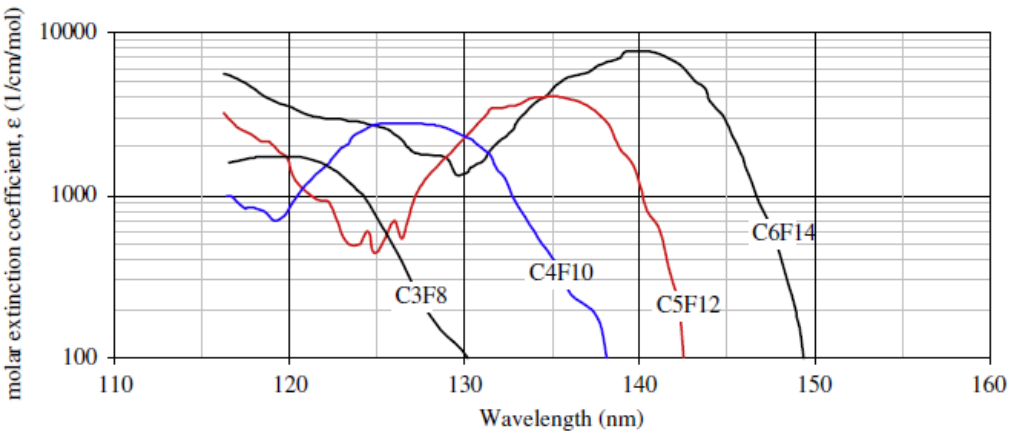

Fig. 1.3 Extinction coefficient as a function of wavelength for different fluorocarbons [6].

Additionally, contaminants like water, oxygen, and carbon dioxide inside the tunnel cause an unfavorable rise in absorbance, A, (Fig 1.4), which, according to the Lambert-Beer law, takes the following form:

$$LBL: \quad A = \varepsilon_c \, c \, r \tag{1.1}$$

Where ε_c is the molar absorption coefficient (m^2/mol), c is the molar concentration (mol/m^3) e r the free geometric path (m).

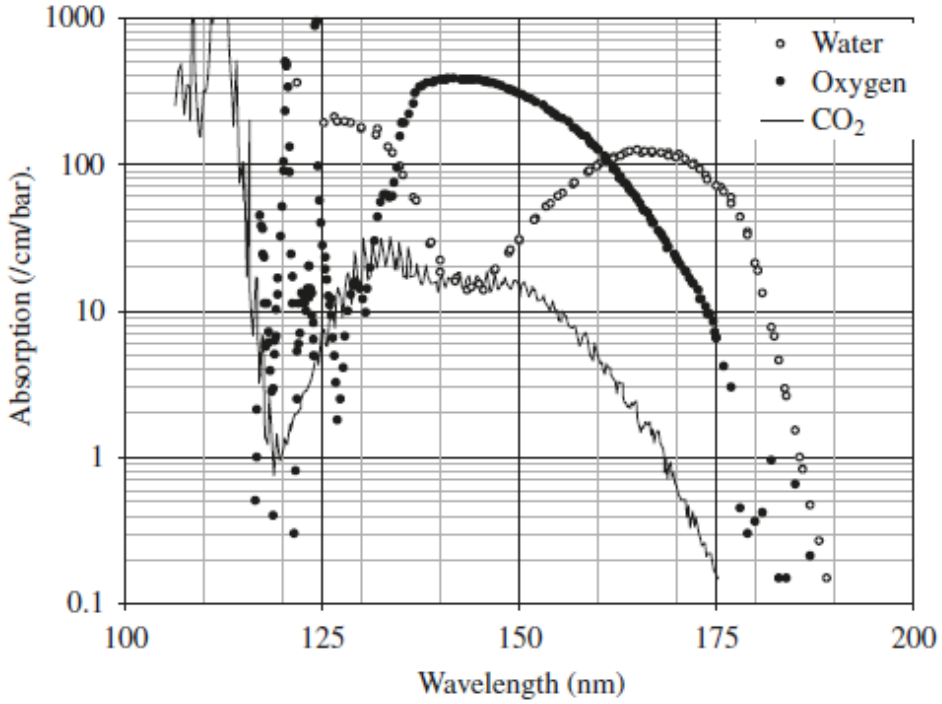

Fig. 1.4 Absorption coefficient at different wavelengths of the contaminants (CO_2, H_2O, O_2) [6].

Hence, to minimize impurities inside the circuit, several solutions have been adopted during the last years.

1.4 Gas System for the RICH-1

To provide a high quality and high stability of the gas mixture, all gaseous detectors require a carefully designed gas system. The gas mixture, which is supplied by dozens of dedicated gaseous streams with a maximum extension of several hundreds of meters, is the key parameter for the detectors' efficiency and safety. The design of the gas system is modular so that it might be adapted to meet the needs of each gaseous detector while maintaining a framework. Each module is implemented by a PLC (Programmable Logic Controller), which makes it simple for authorized employees to monitor and manage operation. The architecture for the gas system is divided into three sections, each with a specific purpose. All the units that require immediate access are situated in the Surface Room (SG). The Experimental Cavern

(UX), which is the efficient detailed distribution to each detector, and the Service room (US), which hosts the pre-distribution system. The whole plant can be additionally divided into unitary blocks each with its own function:

- *Gas Supply Monitoring System*: two parallel paths are used to supply the gas streams into the system. It is possible to use only one part of the driving arrangement while leaving the other in stand-by thanks to their independency. This modularization enables upkeep tasks to be completed without pausing nominal operations.
- *Mixer Module*: within this module, the liquid stream that will become the feed for the detector is vaporized, mixed and sent downstream. The installation of mass-flow controllers allows for constant control of the mixer's output streams.
- *Gas Distribution*: this section is partly located in the US reside pre-deployment modules. Finally, the actual distribution is hosted in the underground area of the cave-UX.
- *Pumping Module*: this module serves as a re-compression section. In order to restore the head lost throughout the circuit, the gas exiting the detector must actually be recompressed.
- *Exhaust Module*: in order to reintroduce fresh gas and maintain a consistent gas volume inside the circuit, the gases contaminated by the existence of any impurities are purged into the atmosphere.
- *Recovery Module*: in this module several attempts to separate perfluorocarbons from inert gases have been investigated. Indeed, the cost of the C_4F_{10} used in the RICH-1 detector can reach 930 CHF/m^3 [25]. Most significantly, n-perfluorocarbons are distinguished by 100-year GWP up to 9200 tons of CO_2 [26].

For the aforementioned reasons, the primary goals of this thesis work are the optimization of the existing system and the ex-novo design of a facility for the separation of n-decafluorobutane from carbon dioxide.

Chapter 2

N-Decafluorobutane Recovery System

2.1 Introduction to Recovery Phases

CERN has implemented several strategies due to the extremely high costs and substantial environmental harm caused by the release of process gases into the atmosphere. It is essential to describe the stages that define the operation of the experiment conducted on the LHCb before moving onto the various measures that have been taken. The whole procedure is actually divided into phases, which are listed below in chronological order:

- *Filling*: this operation consists in flushing CO_2 via the injection of C_4F_{10} inside the circuit.
- *Cleaning*: the perfluorobutane supply ends once the majority of the carbon dioxide has been drawn out. Right after, a purification process involving adsorption through specialized molecule sieves starts.
- *Emptying*: : the sequence of activities is completed at this stage. In a nutshell, emptying represents the filling's opposite procedure. The detector (RICH-1) is refilled with carbon dioxide after the LHCb tests are complete in order to expel the exhaust C_4F_{10}.

Each procedure will be thoroughly clarified in the following paragraphs to make sure the reader can grasp the key points and challenges faced during the decision process.

2.2 Filling

Sending an inflow of process gas to flush the carbon dioxide out of the circuit is what the filling phase entails. As a fact, for the majority of the year, CO_2 is used to keep the circuit and the cave at a small overpressure (1.3 bar), ensuring the mechanical stability of the RICH-1. Hence, the n-decafluorobutane is collected from a tank and sent to the mixer. At atmospheric pressure, C_4F_{10} boils at a temperature of about 271.2 K. Therefore, inside the vessel, at room temperature, and at a pressure of about 3 bar, the fluorinated hydrocarbon is present as a liquid phase. The following figure shows that the vapor pressure of C_4F_{10} is smaller than the pressure inside the tank (Figure 2.1). The VLE experimental data for pure n-decafluorobutane are valid for a short range of temperatures (233.27-269.24 K) [27], Peng-Robinson Equation of State (EOS) has been use to extend the plot. As one can notice the two curves are almost overlapped.

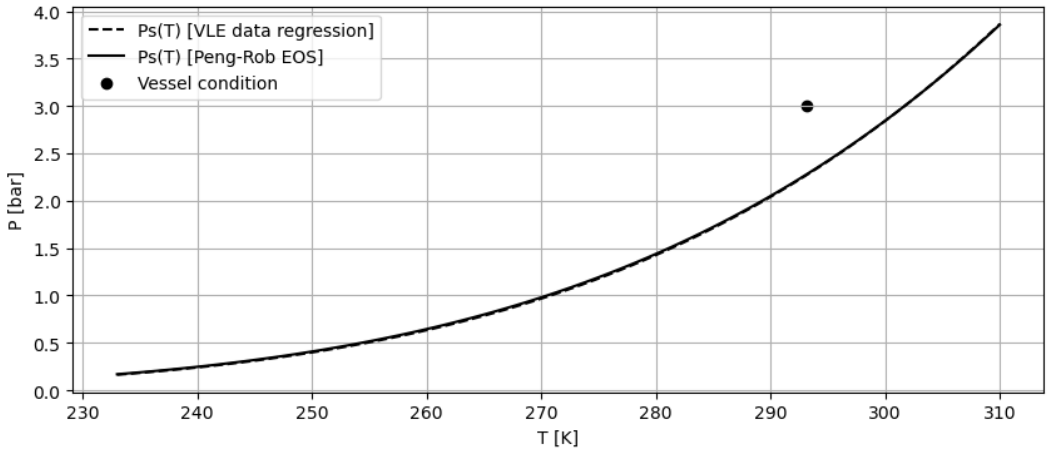

Fig. 2.1 Vapor pressure of C_4F_{10} (bar) as a function of temperature (K): comparison between experimental data and Peng-Robinson predictiveness.

The CO_2 flushing process lasts several hours, ending only when a given molar fraction of C_4F_{10} is present into the circuit streams. It is important to point out that, in contrast to the conditions previously described, the volume of the accumulation tank has been contaminated with CO_2 and traces of air as a result of previous attempts to recover n-decafluorobutane during filling and emptying operations. Because of this, references to a non-pure filler gas that is in a blend will now be made consistently. The volumetric flowrate fed to flush out CO_2 ranges between 0.11-0.16 m^3/h (at

P and T respectively around 1.3 bar and 20°C). The flushing process takes several hours to complete (50-100 hours). The molar composition of the gaseous mixture that is measured in the "Pumping" module is clearly variable during this time period. A CO_2-only gas stream with remnants of air is detected during the first eight hours (by Gas Chromatography). A non-negligible C_4F_{10} concentration is first noticed about 10 hours after the measurements kick off, and in the following 20 hours a pseudo-exponential rise is experienced. After an outlier peak, that was likely caused by a Gas Chromatograph (GC) calibration error, a nearly linear trend with a weak slope can be observed (Figure 2.2). It must be specified that the molar fraction of air has been neglected for graphical reasons.

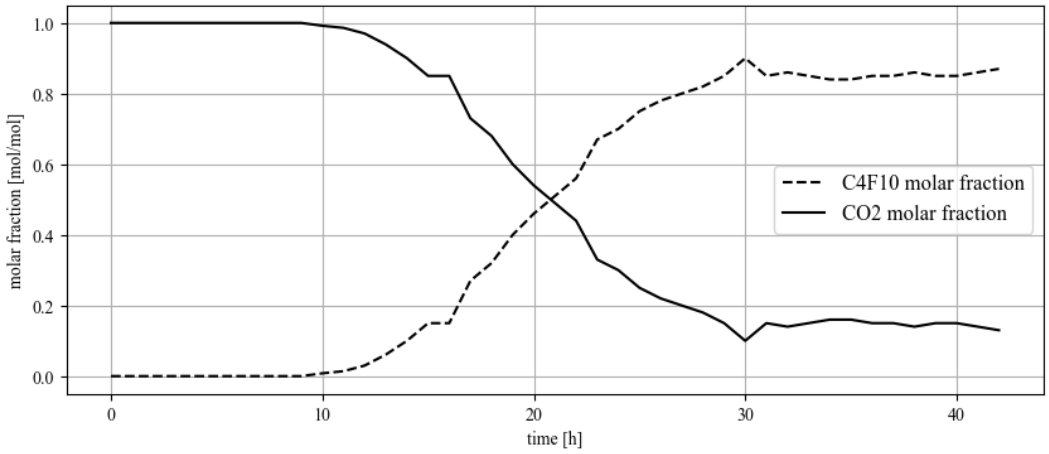

Fig. 2.2 Molar fraction of CO_2 and C_4F_{10} after the Pumping module at different times during the start-up of the filling procedure.

The current recovery system is triggered when the C_4F_{10} volume fraction hits about 10%. The apparatus currently consists of a series of heat exchangers whose feature is to pre-cool the inbound gaseous mixture and a partial condensation stage called *Liquifier*, where a fraction of the incoming gas is liquefied. The remainder of the flow fed is discharged (into the atmosphere) from the apparatus's head. (Fig. 2.3). Note that the earlier P&IDs labels nitrogen as the exhaust gas. This is incongruence is due to the fact that the flushing gas in the early years was N_2, which was later changed to CO_2 due to its lower impact on detection quality.

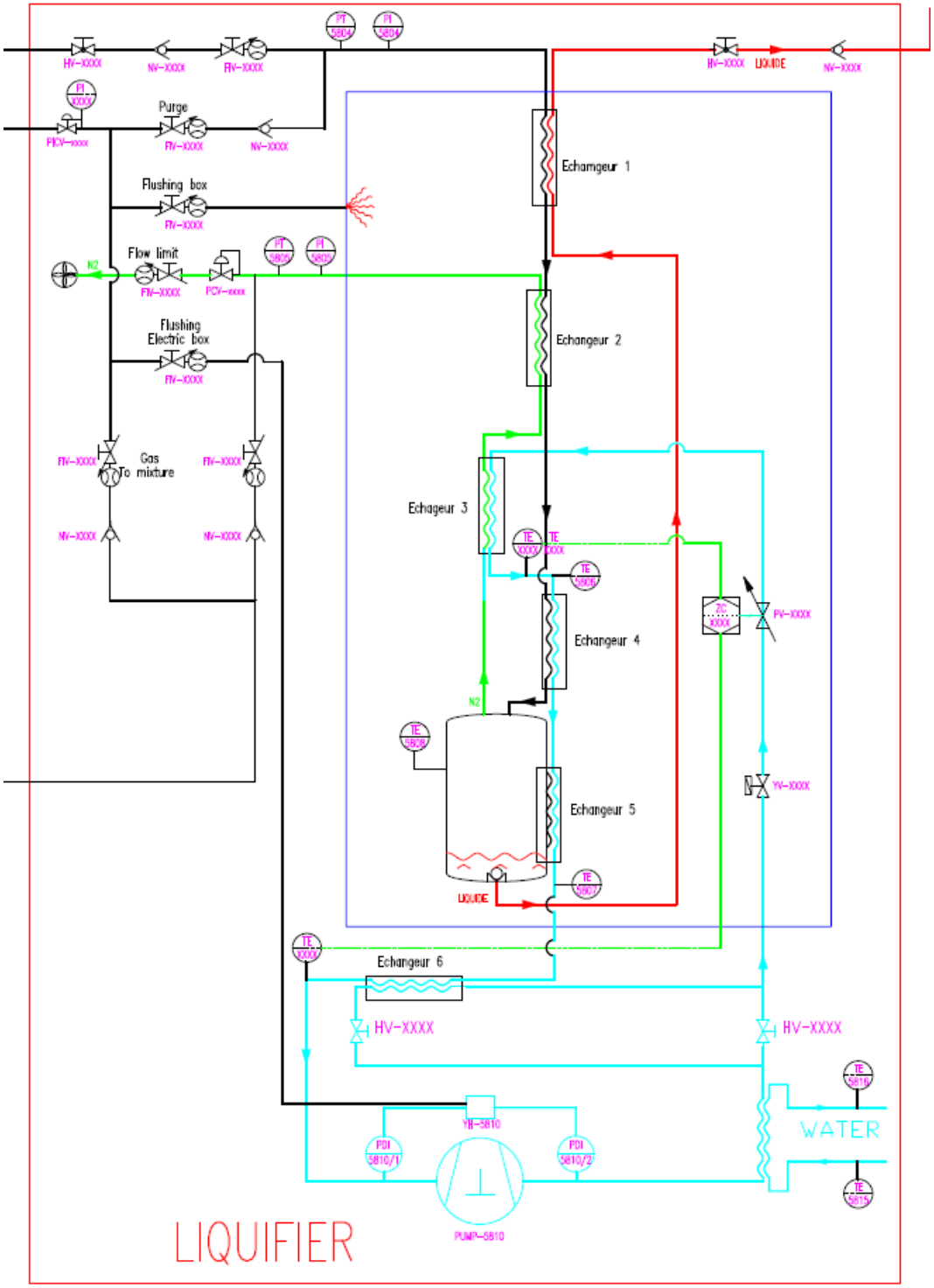

Fig. 2.3 Small portion of the actual C4F10 recovery system: *Liquifier* section.

The presence of this condensation system makes it possible to improve the composition of the gaseous mixture in the circuit. On the other hand, there are several inefficiencies on which it is deemed necessary to improve.

1. No control methods can be employed to change the apparatus working temperature (-25 °C). Moreover, increasing or decreasing the flow rate of the exhaust gas is the only way to directly change the pressure. Pressure, that, must be higher than 3 bar so that the liquid product can flow into the C_4F_{10} tank.

2. The composition of the stream supplied to this device changes over time. In reality, it evolves from a stream of carbon dioxide only (with traces of air due to circuit leaks) to a mixture that is very rich in perfluorobutane in the ending phases. As a result, the process specifications will change as the operation progresses, including the liquified flowrate and the molar compositions exiting the separation stage. Additionally, these are completely uncontrollable.

3. The time required to reach a molar composition of C_4F_{10} equal to 95% vol, at which it is possible to start the cleaning operation, is extremely long. It actually, takes several days, if not weeks (Fig. 2.4). This statement could seem an incongruence with the 50-100 hours duration previously stated, but the operations are not continuous.

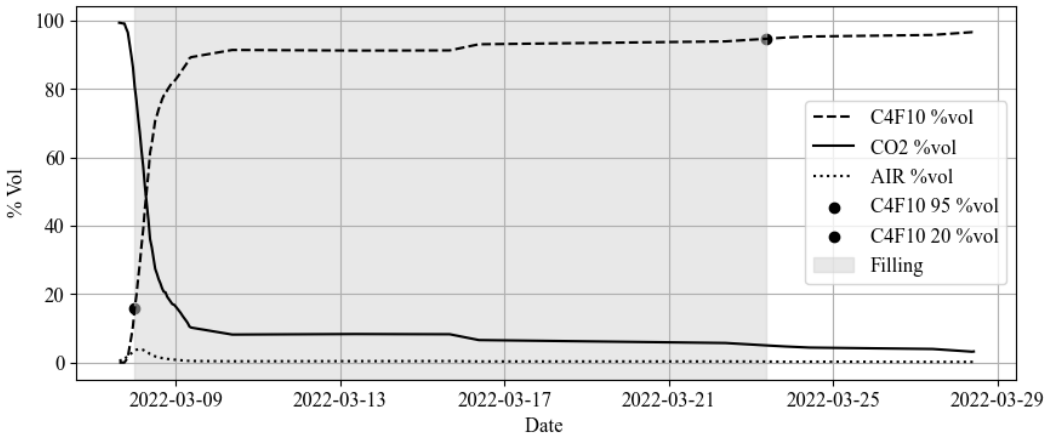

Fig. 2.4 Molar fraction of CO_2 and C_4F_{10} after the *Pumping* module at different times during the entire filling procedure.

2.3 Cleaning

The branch through which the process gas is transported is closed after the filling operation is complete. Now, a closed loop is operating throughout the entire system. The elimination air and of the last quantity of carbon dioxide makes up the cleaning process. Two adsorption columns filled with specific solids that have a high specific area are used for the capture. To be able to run constantly, specifically two adsorbent beds have been constructed in a parallel configuration. Actually, one column performs its function while the other regenerates.

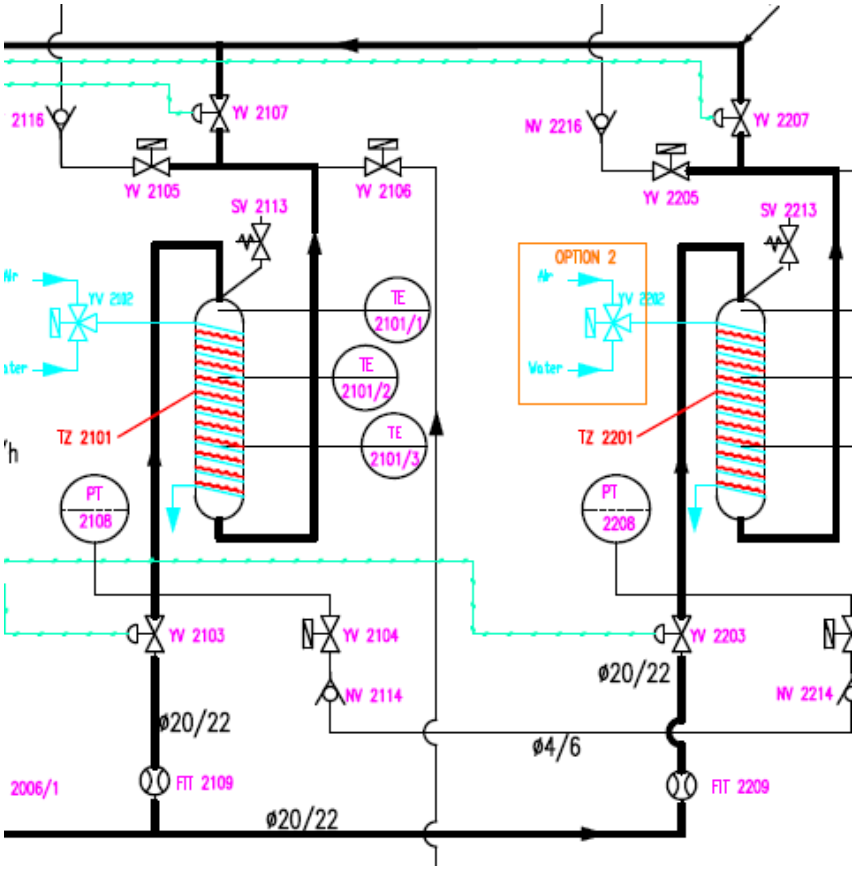

Fig. 2.5 Small portion of the actual C_4F_{10} recovery system: *Purifier* section.

In reality it must be underlined that the *Liquifier* and the purification system (*Purifier*) are both turned on at the same time. However, because the bed is already pre-saturated with CO_2 at this point, its main function is to remove the water that is present in the leaked air as humidity. In the partial condensation system, failure to

remove water would result in the production of ice, which would reduce the effective heat exchange area and, ultimately, the efficiency of the entire system.

2.4 Emptying

A full cycle comes to an end with the emptying phase. It is effectively the opposite process from filling, which involves pumping pure CO_2 into the circuit to empty it of the depleted C_4F_{10}. In this instance, the concentration measurements within the circuit show a trend that is essentially symmetrical to the one shown in Figures 2.2 and 2.4.

Chapter 3

Investigation of the Gas Mixture: Equilibrium and Phase Behavior

3.1 Definition of the Goal

After outlining the steps that control the gases utilized by the RICH-1, the current C_4F_{10} recovery technique is now discussed. The recovery method, which was discussed in the previous chapter, exploits the relative volatility of the various molecules in the mixture, which, at atmospheric pressure, have the following boiling temperatures and sublimating (Table 3.1).

It is necessary to look into the thermodynamic balances between n-decafluorobutane and carbon dioxide in order to comprehend the efficiency of the current system, which will now be expressed in terms of Recovery (R_{C4F10}) and Purity (P_{C4F10}) of the C_4F_{10} extracted from the tail of the partial condenser (Equations 3.1 and 3.2). In fact, a binary mixture can be assumed for separation purposes, with CO_2 serving as thelight

Table 3.1 Transition Temperatures at atmospheric pressure of the species present in the gas mixture.

Molecule	T (K)
C_4F_{10}	271.2
CO_2	194.7
O_2	90.2
N_2	77.4

key component. As a result, in the exhaust stream, the lighter molecules (O_2 and N_2) will be virtually entirely eliminated.

$$R_{C4F10} = \frac{L_{C4F10}}{F_{C4F10}} \times 100 = \frac{L \cdot z_{C4F10}}{F \cdot x_{C4F10}} \times 100 \tag{3.1}$$

$$P_{C4F10} = x_{C4F10} \times 100 \tag{3.2}$$

Where L and F stand for the molar flow rates (mol/s) that are retrieved from the bottom and supplied to the separation stage, respectively. While the molar fractions of C_4F_{10} in the aforementioned currents are represented by x and z (mol/mol).

3.2 VLE: Analysis and Modelling

Now, the details about the method used to develop a thermodynamic model that can forecast the liquid-vapor equilibrium of a mixture of CO_2 and C_4F_{10} are explained. The condition of vapor-liquid equilibrium (VLE) is expressed through the equality of the chemical potentials (μ) in the two phases, therefore, for the j^{th} component in the mixture, one can write:

$$\mu_j^l = \mu_j^v \tag{3.3}$$

And the chemical potential associated with the liquid and gas phase (Equations 3.4), can be, respectively expressed as:

$$\mu_j^l = x_j \, P_{s,j} \, \gamma_j \qquad\qquad \mu_j^v = y_j \, P \, \Phi_j \tag{3.4}$$

Where μ_j^l and μ_j^v are the chemical potentials of the j^{th} component respectively in liquid and vapor phase. P and $P_{s,j}$ are the pressure of the system and the vapor pressure of the j^{th} component (bar). The term γ_j represent the activity coefficient and Φ_j is a term that follows:

$$\Phi_j = \frac{\phi_j}{\phi_{sat,j}} \, e^{\frac{V_i^l \ (P - P_{s,j})}{R \ T}} \tag{3.5}$$

Where ϕ_j is the fugacity coefficient of j^{th} species in the mixture at [T,P] condition, $\phi_{sat,j}$ at saturation conditions and, lastly the exponential term is the Poynting Factor [17].

Most of the time, the fugacity coefficient is believed to be unitary in systems with low pressure. On the other side, it's frequently a very strong assumption to ignore the activity coefficient. In fact, the second assumption suggests that there is absolutely no interaction between the molecules in the liquid phase. In the present instance, it is quite helpful to put several thermodynamic models to the test and confirm them by comparing them with experimental evidence. Finding equilibrium data for the binary system under study in the literature has shown to be quite challenging. Several authors have focused on the particular CO_2 absorption capabilities of fluorinated hydrocarbon solvents. Costa Gomes et al. [8] have highlighted how the different solubilities of CO_2 in n-hexane and n-perfluorohexane reside in the different distributions of the cavities. In fact, the fluorinated alkanes have greater dihedral angles and C-C distances than the corresponding hydrogenated alkanes. This results in an increase of absorption capacity of the solvent. These results show that, on average, the solubility of CO_2 is double in perfluoroalkanes compared to the corresponding reference alkanes (study conducted on C_{6+} only).

The findings previously given are supported by Benoit Gwinner et al. [9]. This study emphasizes the importance of two factors in comparing carbon dioxide's solubility in various organic solvents. In reality, a solute's solubilization into a liquid phase can be described as a two stages mechanism: (1) Formation of cavities into the solute. In this step the solvent-solvent interactions have to be broken; (2) Insertion of solute into cavities and formation of solute-solvent interactions. As regards the first step, the Hildebrand solubility parameter can be used to estimate the energy required to break the solvent-solvent bonds. In summary, the greater this parameter, the higher the energy necessary to build the host cavities and, as a result, smaller the liquid phase's absorption capacity. The investigation suggests that the fluoroalkanes have a lower Hildebrand solubility parameter than the reference alkanes (a reduction of roughly 20–30%). Meanwhile the solute–solvent interactions seem to have little influence as the first step turns out to be the controlling phenomenon.

Unfortunately, among the various articles analyzed it was not possible to obtain concrete data regarding the solubility of CO_2 in n-perfluorobutane. Finally, the impossibility of building a set up for the determination of Henry's constants on site has forced the use of models solely focused on the liquid-vapor equilibria. Since fugacity is calculated using equations of state and the activity coefficients are evaluated using semi-empirical equations, the equilibrium relations employed are based on equations of state (Peng-Robinson [14]) or predictive models as the following ones:

- Non-Random Two Liquids [11] coupled with Redlich-Kwong [13] EOS (NRTL-RK).
- Non-Random Two Liquids coupled with Hayden-O'Connel [12] EOS (NRTL-HOC).

Isothermal measurements are the subject of all available data. The following temperatures were specifically tested: 263.15, 283.00, 303.12, 308.19, 323.20, and 338.2 K [10]. Figure 3.1 shows the *Pxy* diagrams produced using the aforementioned experimental data.

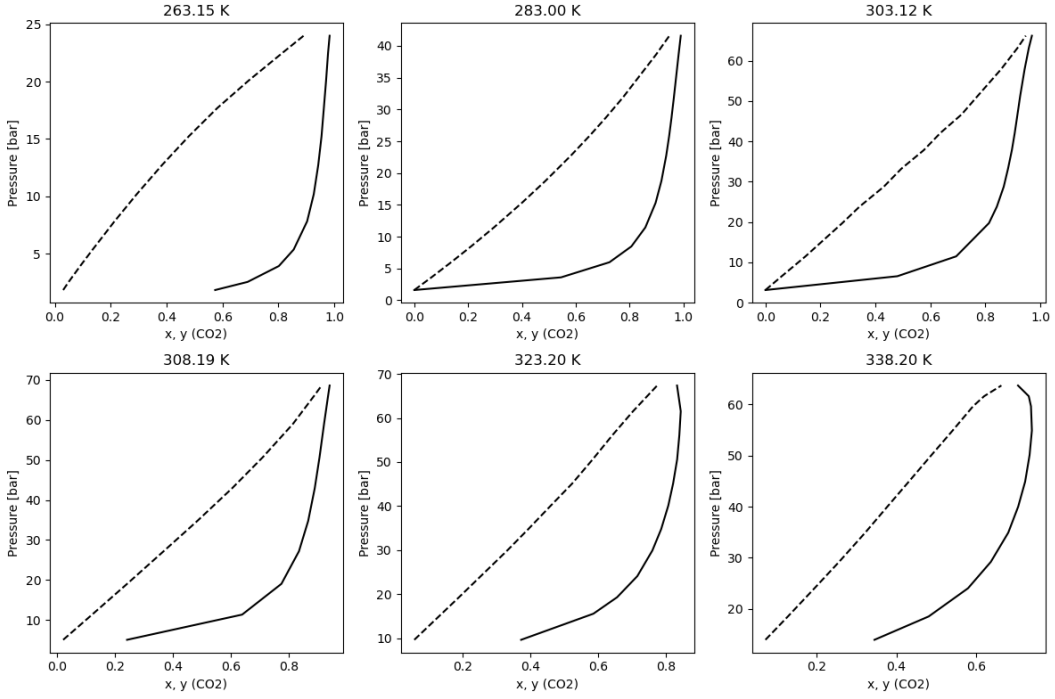

Fig. 3.1 *Pxy* diagrams of the binary mixture at 263.15, 283.00, 303.12, 308.19, 323.20, and 338.2 K produced by using A. Valtz et al. experimental data [10].

According to a preliminary study of the charts, the mixture deviates from ideality positively at low temperatures (Raoult's law [28]), but the divergence turns negative as the temperature rises. Actually, the CO_2 and C_4F_{10} activity coefficients exhibit a positive deviation ($\gamma > 0$) at low temperatures. The activity coefficients estimated using the Aspen Plus process simulator are depicted in the figure below (Fig. 3.2) as a trend.

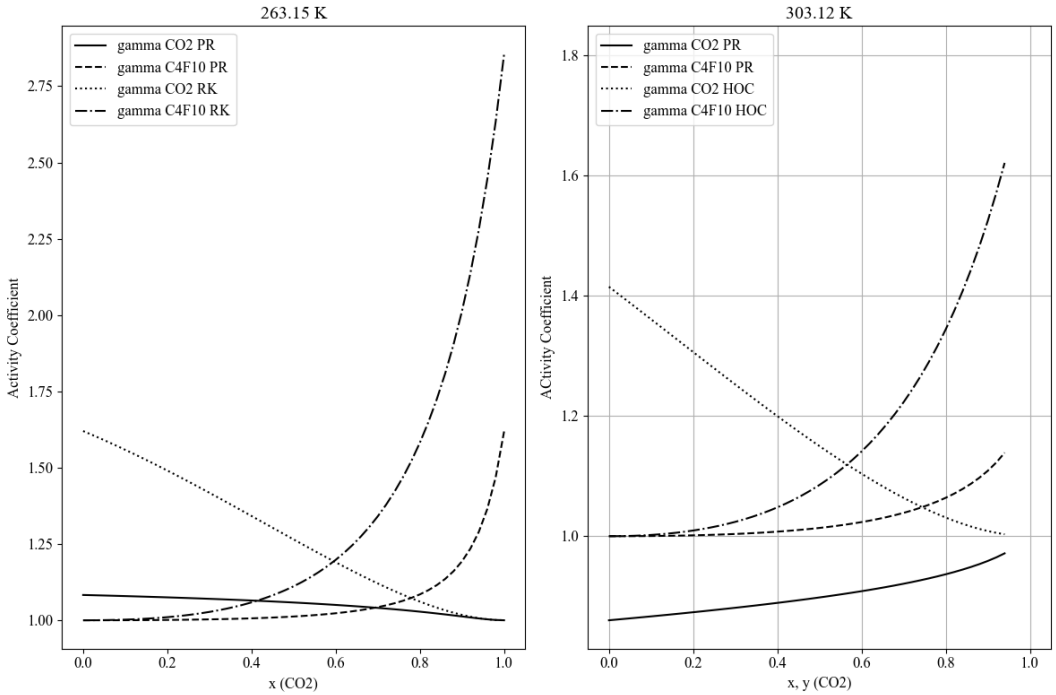

Fig. 3.2 Activity coefficients of CO_2 and C_4F_{10} retrieved using *Aspen Plus* at 263.15 K (left) and 303.12 K (right).

Following the determination of the activity coefficients using the aforementioned models (PR, NRTL-RK, and NRTL-HOC), it was easy to derive the relative equilibrium diagrams at various temperatures by using the simulator. Obviously from Figure 3.3, a model that relies exclusively on equations of state (PR) fails to forecast the equilibria in a substantially non-ideal solution with any degree of accuracy. On the other hand, models that incorporate semi-empirical relationships to calculate the activity of the molecules in the mixture coherently approach the treated system. Bearing in mind that the NRLT-HOC model is more accurate at conditions near to room temperature (303.12 K), whereas the NRTL-RK pair almost exactly matches the experimental data at low temperatures (263.15 K).

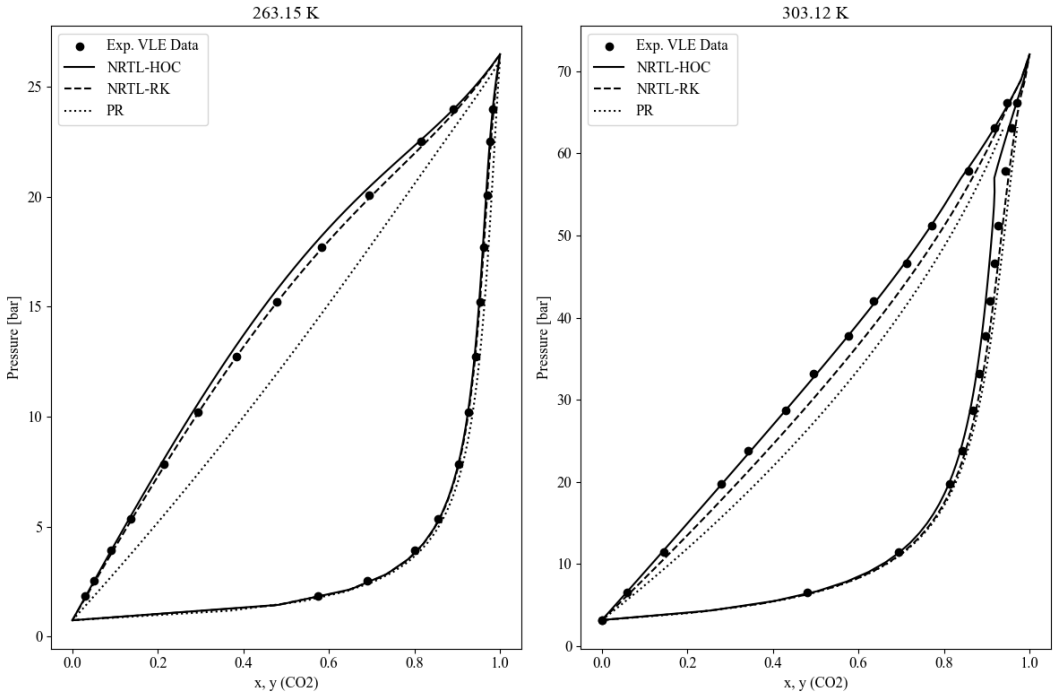

Fig. 3.3 *Pxy* diagrams: a comparison between experimental data [10] and predictive models (PR, NRTL-RK, NRTL-HOC) at 263.15 K (left) and 303.12 K (right).

3.3 RMSE: Choice of the Most Suitable Model

It was necessary to analyze the experimental equilibrium data by comparing them with each of the models mentioned above in order to determine which thermodynamic framework would be most suitable to simulate the current system and to determine a new separation process capable of obtaining a liquid stream of pure C_4F_{10}. Particularly, temperatures close to the key component's boiling point have been studied. The Root Mean Square Error (RMSE), often referred to as the Root Mean Square Deviation (RMSD), was used for the purposes of this comparison. The quadratic mean of the difference between observed and expected values is represented by the RMSE:

$$RMSE = \sqrt{\frac{\sum(\omega^{exp} - \omega^{model})^2}{N_p}} \tag{3.6}$$

Where N_p is the number of experimental data points and ω^{exp}, ω^{model} represent, respectively, the experimental and model-retrieved data.

The mixture's corresponding vapor pressure values and the CO_2 molar fractions in the vapor phase were computed after the CO_2 molar fractions in the liquid phase were fixed. The experimental values were next compared with these predictions. The figures below display the pressure and vapor phase composition errors at three distinct temperatures (263.15, 283.00, and 303.12 K). In particular, the comparison was performed by computing the errors and quadratic errors for the vapor phase's composition (Figures 3.4 and 3.5), while for pressures, the graphs have been normalized using the equivalent experimental pressure values (Figures 3.6 and 3.7).

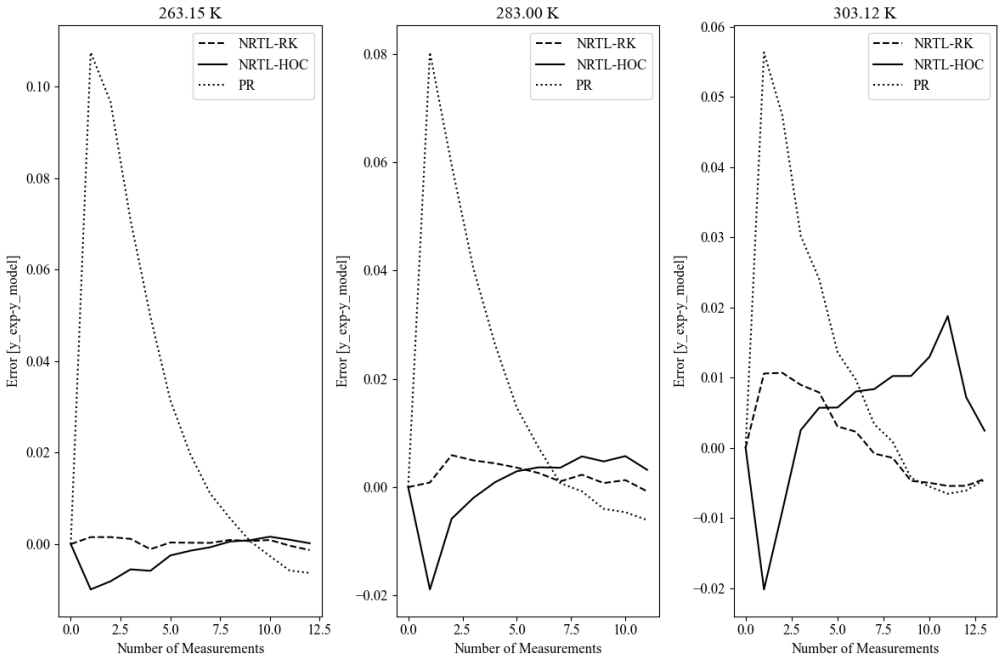

Fig. 3.4 Error between experimental data [10] and calculated vapor phase fraction (y) in equilibrium with the liquid (x) at a given pressure (P).

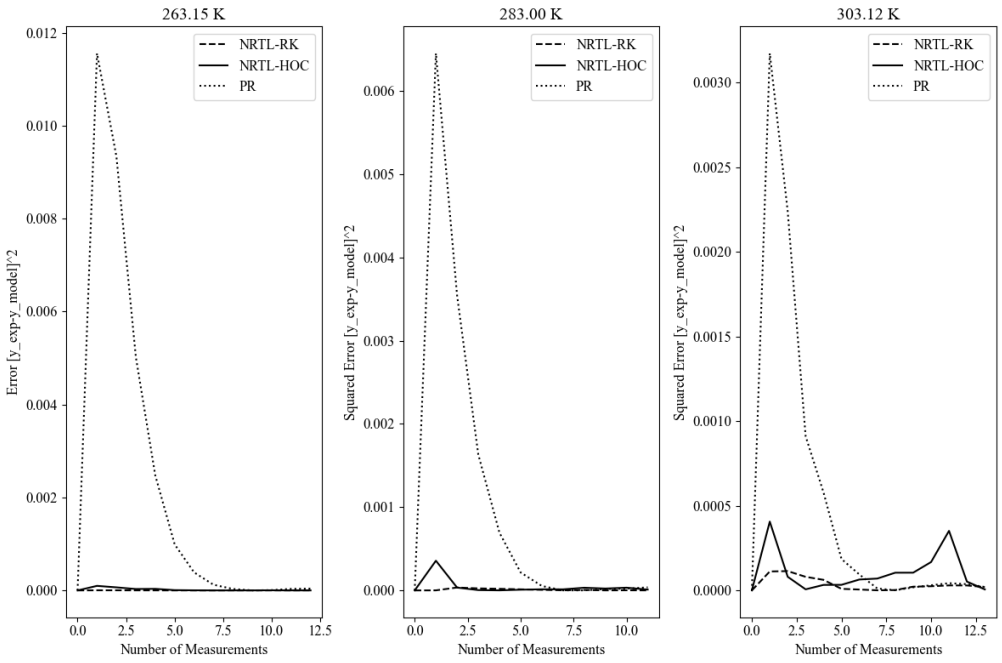

Fig. 3.5 Squared error between experimental data [10] and calculated vapor phase fraction (y) in equilibrium with the liquid (x) at a given pressure (P).

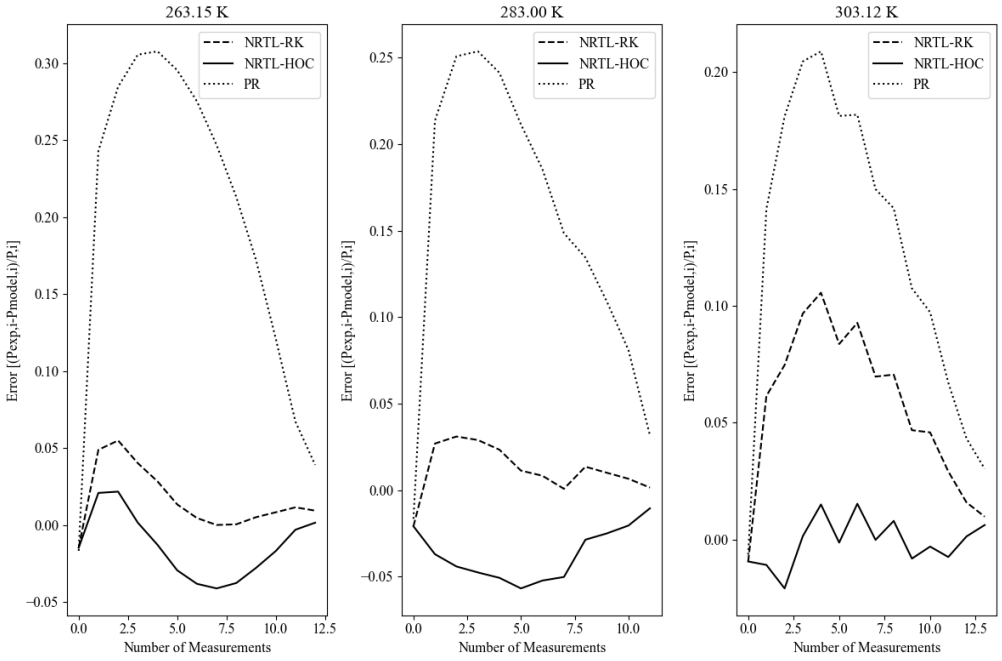

Fig. 3.6 Normalized error between experimental data [10] and calculated pressure (P) at a given x-y equilibrium.

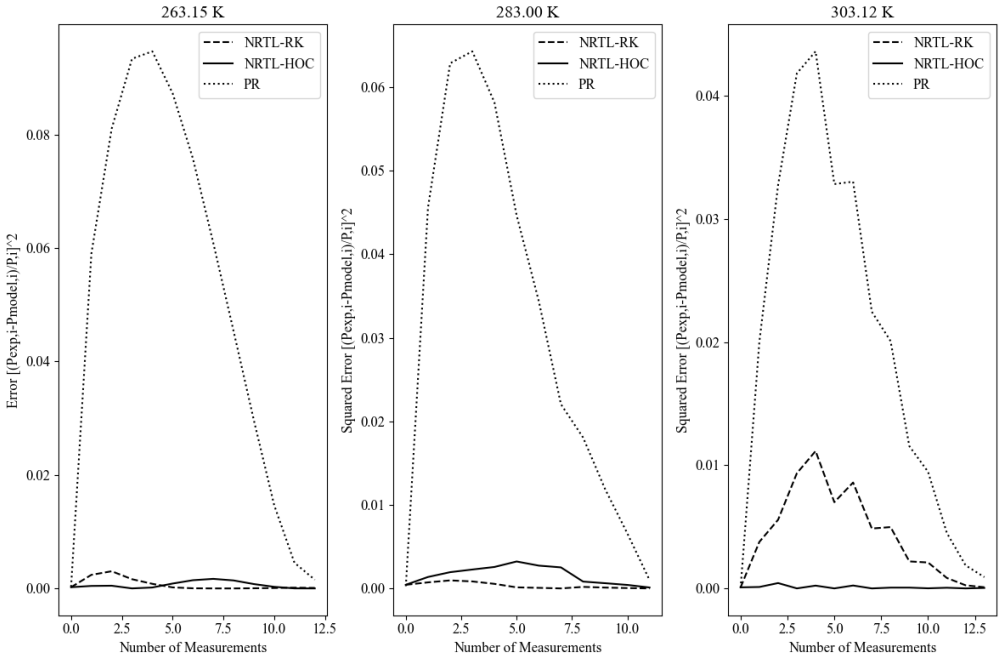

Fig. 3.7 Normalized squared error between experimental data [10] and calculated pressure (P) at a given x-y equilibrium.

The graphs demonstrate how the NRTL-RK approach may more accurately predict the experimentally recorded values at low temperatures (263.15 and 283.200 K). At conditions above or close to room temperature, the combination of NRTL with the HOC virial equation provides greater accuracy. In fact, deciding to use a single EOS, as Peng-Robinson, turns out to be the poorest alternative. Figures 3.6 and 3.7 display high peaks in terms of normalized errors and normalized squared errors at each tested temperature. The tables used to calculate the RMSE for the pressure RMSEP (Tab. 3.2), and NRMSEP (Tab. 3.3), and for the composition of the vapor in equilibrium, RMSEY, with the different models tested (Tab. 3.4), are presented here in order to provide confirmation. The equations used to compute tables and charts are reported in the Appendix A.

In conclusion, it becomes apparent from the analysis and comparison of the experimental data with some of the available models in *Aspen Plus* that using NRTL-RK is the most reliable model.

Table 3.2 Root Mean Square Error for the pressure.

RMSEP	Temperature (K)		
Model	263.15	283.2	303.13
PR	2.0921	3.0998	4.2245
NRTL-RK	0.1376	0.2448	2.0007
NRTL-HOC	0.3003	0.7935	0.2571

Table 3.3 Normalized Root Mean Square Error for the pressure.

NRMSEP	Temperature (K)		
Model	263.15	283.2	303.13
PR	0.232	0.183	0,145
NRTL-RK	0.026	0.018	0.068
NRTL-HOC	0.025	0.041	0.010

Table 3.4 Root Mean Square Error for the vapor composition.

RMSEy	Temperature (K)		
Model	263.15	283.2	303.13
PR	0.048	0.032	0,023
NRTL-RK	0.001	0.003	0.006
NRTL-HOC	0.004	0.007	0.023

Chapter 4

Design and Simulation of a New Separation Process

It has been quite helpful to fully understand the issues regarding the current separation system from the earlier chapters. The goal of the project is the development of a new recovery process that can increase C_4F_{10} purity (Eq. 3.2) while maintaining a high recovery rate (Eq. 3.1). Due to these circumstances, the new system's concept has born out of a necessity to solve current issues and fulfill key requirements. The following essential aspects must be taken into account in order to respect the targets that CERN has set for this work.

Any system, and specifically the equipment designed for the separation of components in mixtures, has historically worked most effectively in steady state in the chemical process industry. Attaining stationary conditions is not only required to ensure consistent compliance with specifications, but it is also critical to the design and management of control and protection systems. As a fact, multiple tiers of control and protection are provided in order in to return the system to stationary conditions (also known as nominal or design conditions). In fact, their duty is to measure the variables that need to be controlled and, when necessary, perform systemic corrections to bring the deviating parameters within a certain range of values or to an agreed-upon setpoint.

Therefore, the key element of any separation apparatus is the requirement of steady state conditions. The existing recovery system lacks this attribute since it feeds a gas stream whose composition and flow rate change significantly over time. Therefore, even if the existing system were flawlessly constructed and, in principle, the conditions of thermodynamic equilibrium were achievable, one would still end up with a fluctuating product purity and recovery. Moreover, for a significant percentage of the operating time, the product would not meet specifications.

4.1 Assessing the Performances of the Current System

The current recovery is based on a partial condensation of the gaseous mixture, as mentioned in previous sections. It is useful to take a look at another binary equilibrium diagram to acquire a more accurate portrait of the conditions of the condensate leaving the separation stage. The dynamics of a binary mixture as its composition, pressure, and temperature change are described by the *Txy* diagram, which is frequently used in fractioning technologies. Namely, it is an isobaric diagram, in which the vapor, biphasic lens, and liquid are differentiated as the standard three areas.

The *Txy* diagram for the system under investigation is displayed in Figure 4.1. The *dew curves* and *bubbling curves* are displayed specifically at pressures of 1, 2, 3, 4, and 5 bar. The system is biphasic within the center lens, which is generated when these curves are joined. There are therefore two phases in equilibrium when the pressure, for instance, is fixed at 3 bar and the temperature is set between the boiling points of the two constituents of the mixture. The intersection between an isotherm and the dew and bubbling curves describes, respectively, the composition and the quantity of both the vapor and liquid phases.

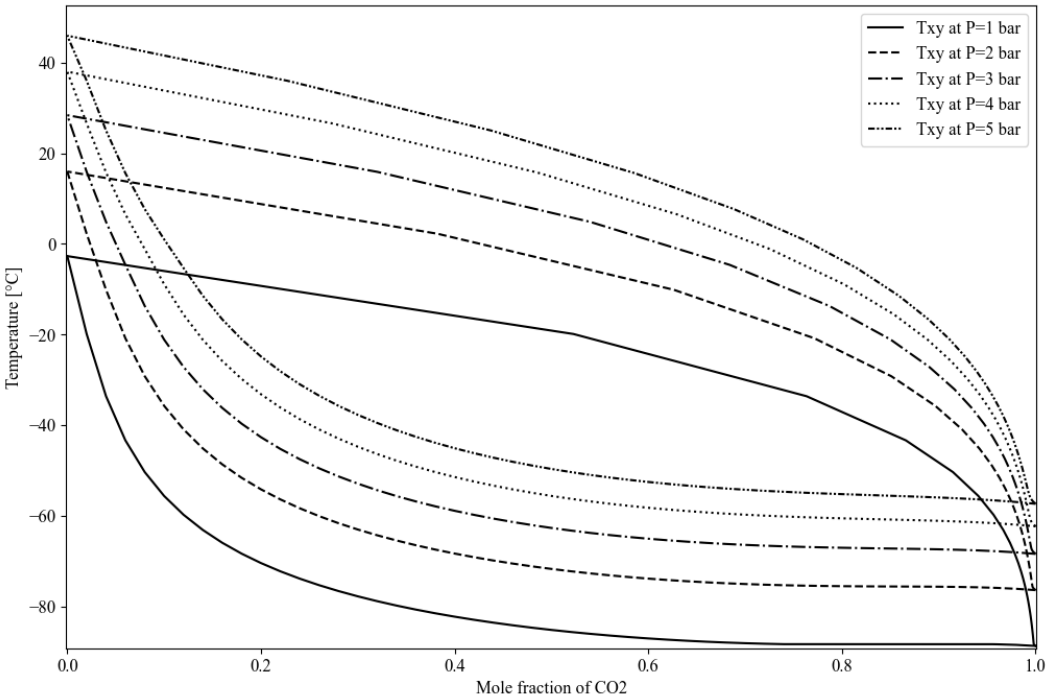

Fig. 4.1 *Txy* diagrams for the $CO_2 - C_4F_{10}$ binary mixture at 1, 2, 3, 4, 5 bar (NRTL-RK method).

It is possible to determine the compositions of the two phases by setting T and P, respectively, at -25°C (nominal operating temperature of the current partial liquefaction stage) and 3 bar (Fig. 4.2). Being a bivariate region, fixing two parameters (T, P), the composition of the two phases can be, independently from the starting composition, uniquely identified (point A corresponds with point D, and point B with E). However, by selecting a different starting vapor composition, different quantitative ratios (in terms of mass) between the two phases will be achieved. For instance, if we start with a vapor containing 30% mol of CO_2 at about 25° and begin to remove heat down to -25° (left-side diagram), we will end up with a two-phase mixture. The vapor phase will have a composition of 90% mol CO_2 (point B) and the liquid in equilibrium with it will be 12% mol CO_2. However, the lever rule is used to calculate the amount of vapor and liquid in terms of moles. As a result, the ratio between the lengths of the segments AC and BC provides the relationship between the moles of vapor and liquid.

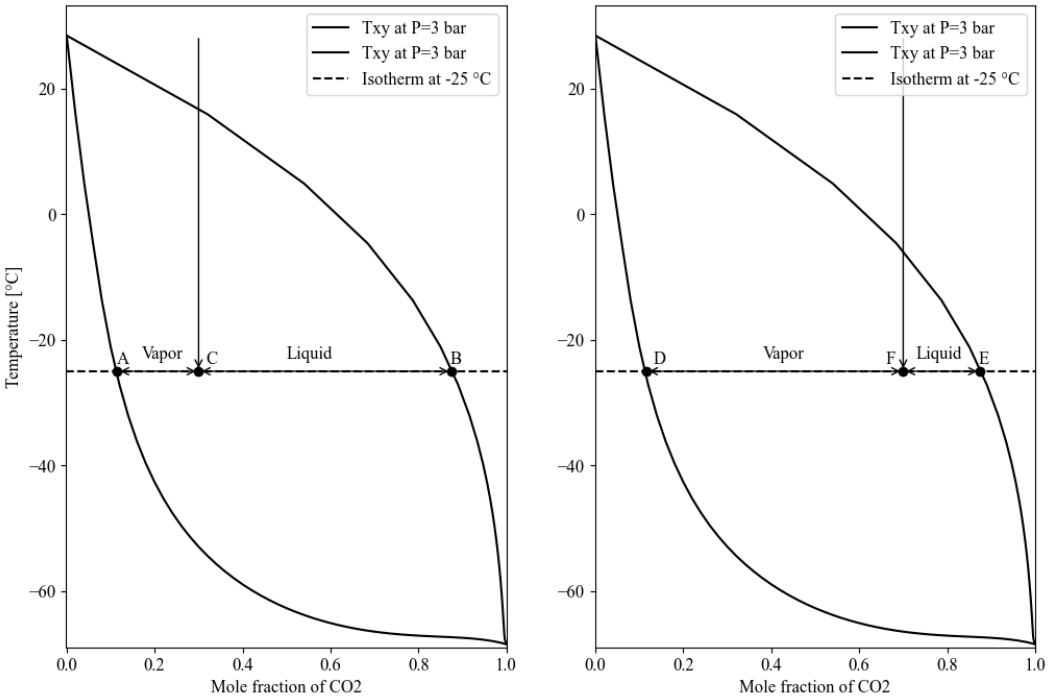

Fig. 4.2 *Txy* diagrams for the $CO_2 - C_4F_{10}$ binary mixture at 3 bars (NRTL-RK method). Left-side diagram represent a cooling process starting from a vapor mixture 30% mol (CO_2) while the right-side diagram the same process starting with a 70% mol.

This brief explanation helps us to comprehend that the liquid phase's purity is not quite as flawless as CERN had hoped (over 99% mol in C_4F_{10}). Due to this, the *Filling* phase is followed by an adsorption phase (*Cleaning*). Secondly, C_4F_{10} recovery in the liquid phase fluctuates based on the input composition's variability.

Data related to the operations that took place in the first semester of this year (2023), which supports this quick assessment, are available. The filling procedure took place between 07/03/2023 and 28/03/2023, as had been anticipated in section 2.2. This procedure then needs to be split down into two steps, which will be referred to as *Filling I* and *Filling II* for ease of reference.

The filling I is the phase that Figure 2.2 emphasizes. It has been observed that when the concentration of the mixture after the pumping module has a non-negligible molar fraction in C_4F_{10}, the recovery system is triggered while the mixture rich in C_4F_{10} present in the accumulation tank is pumped inside the system. The system has been specifically engaged on 07/03/2023. The gaseous phase present inside

the accumulation tank has been initially used as a flushing stream. The supplied mixture had the following molar composition: 55.7% C_4F_{10}, 38% CO_2, and 6.3% *Air*. After a few hours, the system's composition is such that it is necessary to begin pumping the liquid phase into the tank that is richer in C_4F_{10}. This first phase last for approximately 50 hours, until 09/03/2023. A weight variation of the accumulation tank equal to 60,5 kg has been recorded during this initial phase, and 65,5 kg of the mixture have been fed inside the circuit. Overall, 9 kg sent as a vapor phase, and the remaining 56,5 kg as liquid (vaporized into the Mixer module). Table 4.1 displays the molar and mass compositions of the two phases.

Table 4.1 Molar and mass composition of the liquid and vapor phase in equilibrium into the tank.

Component ID	Molar Fraction, x_m (mol/mol)	Molecular Weight, MW (g/mol)	Mass Fraction, x_w (g/g)
		Vapor	
C_4F_{10}	55.7%	238.03	87.7%
CO_2	38.0%	44.01	11.1%
Air	6.3%	28.96	1.2%
		Liquid	
C_4F_{10}	95.0%	238.03	99.0%
CO_2	5.0%	44.01	1.0%
Air	0.0%	28.96	0.0%

Once the compositions are known, it is straightforward that around 63,7 kg of C_4F_{10} have been introduced into the system, whereas less than 5 kg have been recovered (conceivably recoverable mass if the condensate were pure in C_4F_{10}, Rec_I^{id}). With a net loss of 8,7 kg of mixture via the exhaust stream. The average composition at the exhaust is displayed in Table 4.2. As a result, since 5,42 kg of C_4F_{10} are lost ($Lost_I$), the ideal liquefier efficiency (η_I^{id}) during Filling I is roundly 38%. Figure 4.3 resumes these results.

$$\eta_I^{id} = \frac{Rec_I^{id}}{(Rec_I^{id} + Lost_I)} \tag{4.1}$$

Table 4.2 Average Molar and Mass Composition of the Exhaust Stream

Component ID	Molar Fraction, x_m (mol/mol)	Molecular Weight, MW (g/mol)	Mass Fraction, x_w (g/g)
C_4F_{10}	22.88%	238.03	62.27%
CO_2	70.82%	44.01	35.64%
Air	6.30%	28.96	2.09%

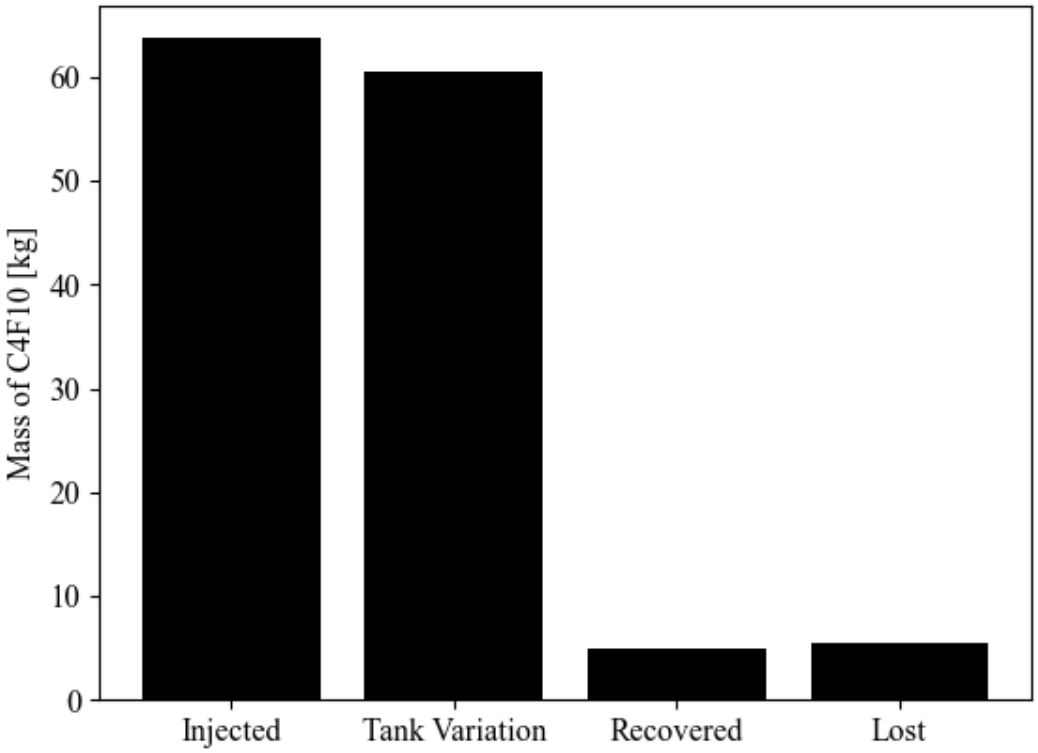

Fig. 4.3 Resumed results of filling I process.

On March 15^{th}, 2023, the second phase (Filling II) begins. The stretch of time between the conclusion of Filling I and the beginning of Filling II is set aside for cleaning the accumulation tank. In fact, it is necessary to deliver a flushing stream cleaner (richer in C_4F_{10}) than the previous conditions once the molar fraction of C_4F_{10} in the circuit reaches a value greater than 85%. Cleaning is done in a semi-closed cycle, meaning that the main circuit is not connected to the separation system. The vapor that is already in the vessel is fed at this step and sent to the customary

partial liquefaction stage. The vapor compositions inside the tank at the start of this process (10/03/2023) and the end (14/03/2023) are shown in Table 4.3.

Table 4.3 Molar composition of the vapor phase inside the accumulation tank and the beginning and at the end of the tank cleaning.

Component ID	Starting Molar Fractions (mol/mol)	Ending Molar Fractions (mol/mol)
C_4F_{10}	55.70%	76.40%
CO_2	38.00%	22.20%
Air	6.30%	1.40%

After this quick phase, the actual Filling II starts, during which a molar fraction of C_4F_{10} in the detector reaches 95%. The ways in which this step takes place are identical to those described several times, so the discussion is here neglected. However, even in this situation, it would be helpful and quite fascinating to go over the data collected this year. The trends of the molar fractions of and CO_2 within the circuit are depicted in Figure 4.4 over virtually the entire month of March (noted that the total of these fractions does not sum to one because there is a small percentage of air that was ignored for visual purposes).

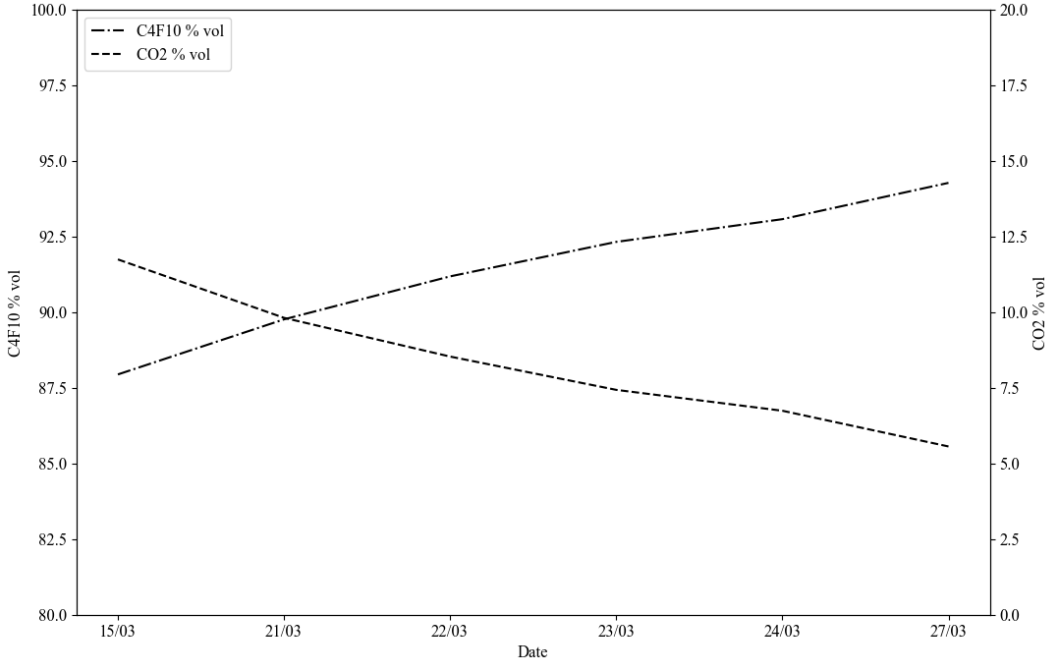

Fig. 4.4 Molar composition after the Pumping module during the Filling II process.

As regards the performance of the second filling phase in terms of efficiency (η_{II}^{id}) it can be highlighted how, differently from Filling I, the situation is less critical. Figure 4.5 reports the estimates of the mass of C_4F_{10} recovered and lost in the exhaust stream obtained in the six days in which the system was active. On the right side of the graph, on the other hand, it is possible to observe the totality of n-decafluorobutane recovered and lost in the aforesaid period. The ideal efficiency in this second scenario is 88.3%.

$$\eta_{II}^{id} = \frac{Rec_{II}^{id}}{(Rec_{II}^{id} + Lost_{II})} \tag{4.2}$$

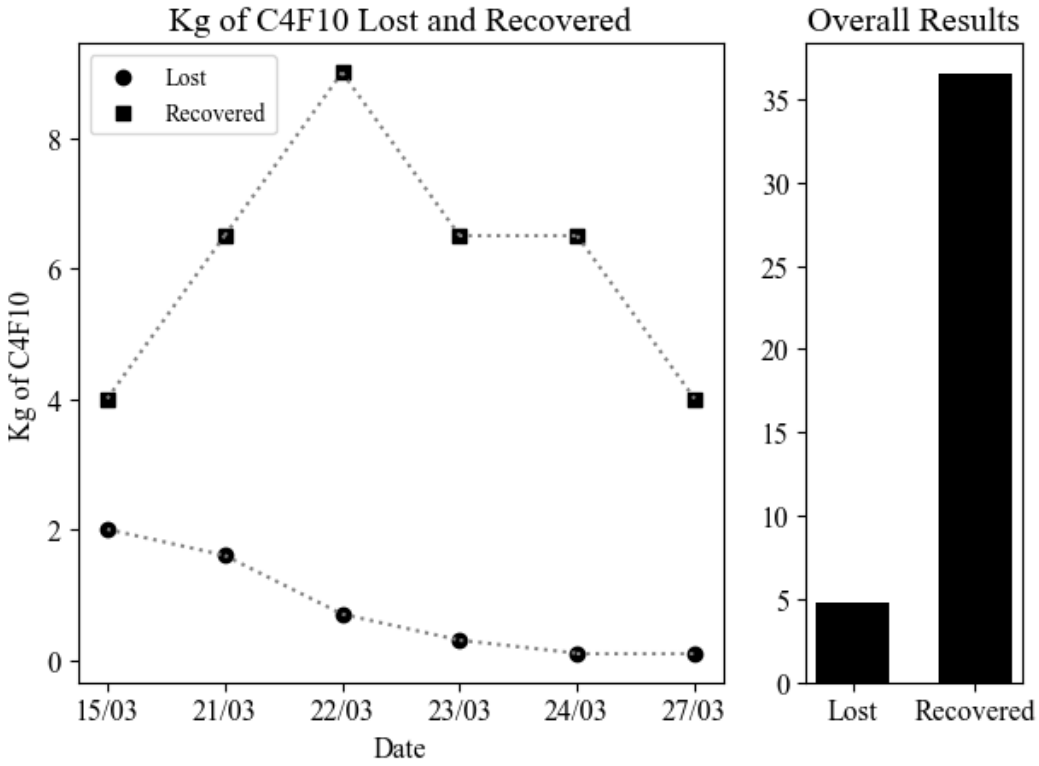

Fig. 4.5 Trend of C_4F_{10} recovered and lost (left-side) and overall results (right-side) during the Filling II process.

This higher efficiency can be explained physically by the fact that a mixture that is already extremely rich in C_4F_{10} is injected into the partial condensation stage. Feeding a mixture lean in CO_2 causes the fraction of liquid formed (under constant process conditions) to be much greater than that of the gas leaving as exhaust.

Calculating the efficiency over the course of single days and examining this pattern confirms this effect. Notice that the efficiency trendline (Fig. 4.6) increases as it gets closer to the filling process's conclusion.

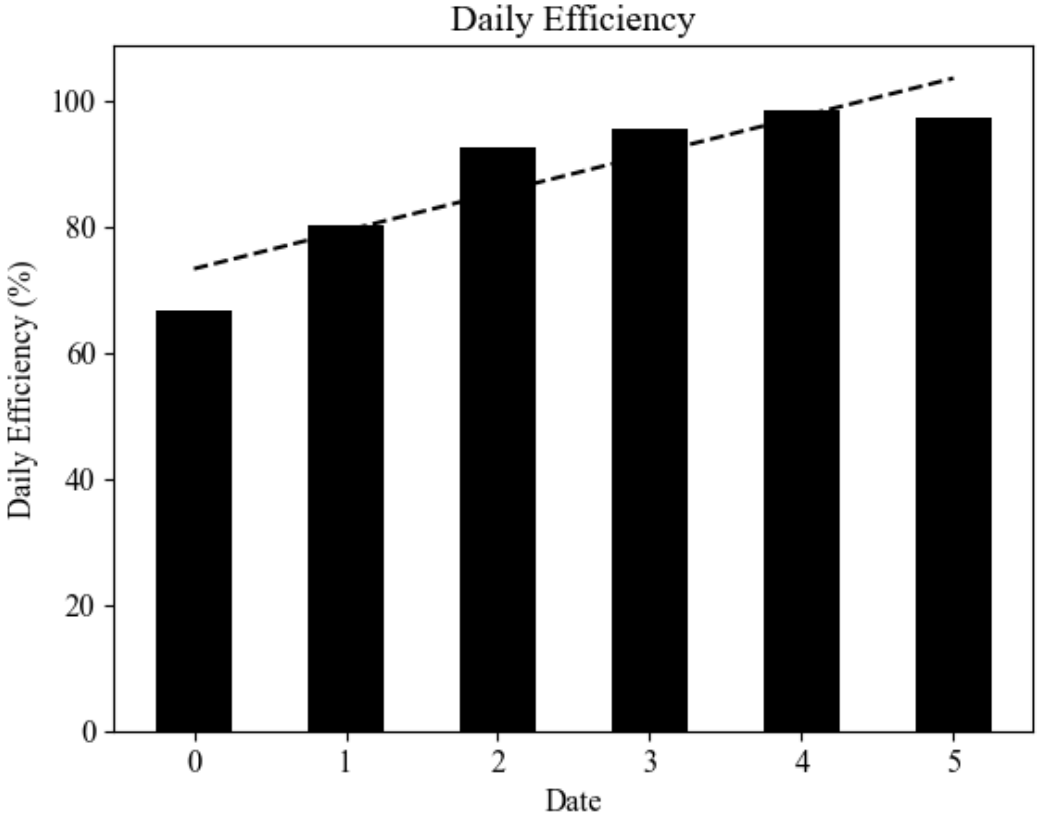

Fig. 4.6 Daily efficiency during the Filling II process.

In conclusion, it can be stated that the total mass of C_4F_{10} recovered during the two operations is approximately 41.5 kg, but the losses are significantly larger. Additionally, the condensate's purity is far below the desired levels. The next chapter's goal is to lead the reader through the design of two parallel systems in order to increase the key product's purity and recovery efficiency.

4.2 Design of the New Plant

The reasons for using the NRTL-RK thermodynamic model have been thoroughly explained in section 3.2. The design phase is shown once a set of equations capable

of accurately forecasting (with minor errors) the behavior of the mixture under investigation has been obtained.

As previously reported, the boiling points of the two molecules under study—carbon dioxide and perfluorobutane—are quite different from one another. In addition, to draw parallels with the current separation technology (partial condensation), it was chosen to construct two systems that, while utilizing the same separation principles, are unique in their own ways. The two systems are:

- *System I*: Double equilibrium stage
- *System II*: Distillation column

In order to guarantee the system's reliability, these two unique solutions have been designed simultaneously. Unfortunately, the change of composition and flow rate that characterizes the current stage of condensation affects both equally. The research of an equalization tank had been planned in order to guarantee a feed stream with a constant flow rate and composition. This tank collects the gaseous stream that exit the detector during the *filling* and *emptying* phases. The plant can be divided into two distinct temporal periods—*accumulation* and *separation*— due to the presence of the tank. Finally, a small pumping station was installed in the facility to allow for fluid compression and movement.

The next sub-chapters are dedicated to the description, design, and simulations of the three subsystems (double stage equilibrium, distillation column, and accumulation tank and pumping station). Before proceeding with the reading, it is recommended to refer to Appendix B, where the *P&ID* of the entire system is provided along with a brief explanation of its general operation.

4.3 Design of the Accumulation Tank and Pumping Station

To understand the operation of the accumulation and compression section, it is useful to use the perspective of the gaseous mixture coming from the rest of the system. The mixture arrives from the left (line L0). Before entering the compression and boosting loop, there is a bifurcation that allows the extraction of gas for composition analysis. The loop consists of a single-cylinder piston compressor (CMP-10150) and two pressure sensors (PT-10170 and 10171) that play a role in measuring and transmitting the pressure difference upstream and downstream of the compressor in order to finely regulate the opening of various pneumatic valves present. Specifically, the two sensors are essential for regulating the gas flow exiting the loop through the recycle stream located in the upper part of the diagram. The recycle is composed of a back pressure valve (PCV-10140), which opens when the pressure in the inlet duct is greater than the sum of the pressure exerted by a spring (manually adjusted as needed) and the pressure exerted by the compressed air to which it is connected. The role of this PCV is to stabilize the pressure upstream of the pneumatic control valve (PV-10141), which is highly sensitive to pressure fluctuations.

Continuing downward, we find the accumulation tank, which serves as an equalization vessel for the mixture's composition. It's worth noting that both pressure and temperature sensors and indicators are present (PT-10173, PI-10172, TE-10180, and TI-10181) in order to constantly control these variables, both through software and visually. A three-way valve (HV-10114) connects two safety valves (PSV-10130 and 10131) to vent compressed gas in case of internal over-pressure. It is important to highlight that, for easy and safe maintenance activities, two safety valves are installed. Therefore, the three-way valve can easily isolate the one that needs to be repaired or replaced.

In the right part of the figure, there is a moisture detector (H2O) to monitor the presence of water within the circuit and prevent ice formation inside the separation systems operating under cryogenic conditions. Finally, another analysis point is installed to monitor the composition of the mixture fed to one of the two separation systems. Finally, the valve HV-10116 is the one that regulates the direction of the feed stream. When the flow goes upward, it it directed to the double stage system (4.4). Instead, when the gas flows left to right it is fed to the distillation system (4.5).

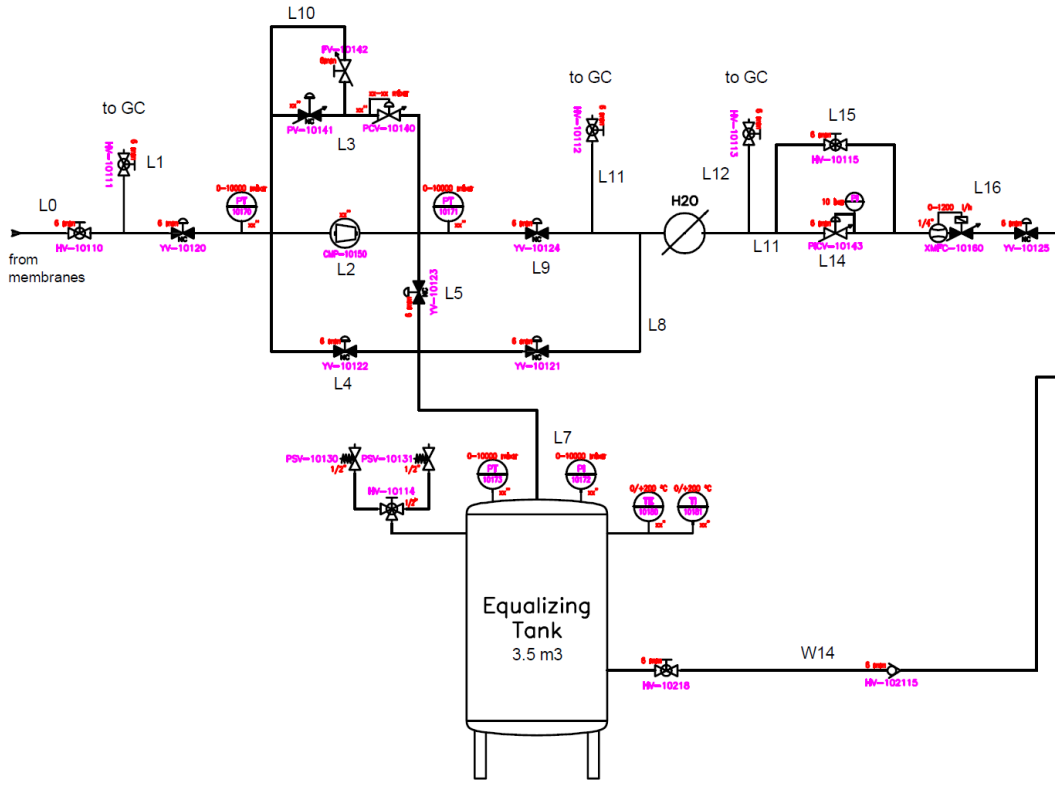

Fig. 4.7 Accumulation and Compression Section of the P&ID.

Let's now briefly discuss the different phases

- *Accumulation phase*: the gaseous mixture of variable composition arriving from line L0 (Figure 4.7's left side), is compressed and pushed into the tank following the path L0-L2-L5-L7. The pneumatic valves YV-10120 and YV-10123 and the manual valve HV-10110 are open, while the valves YV-10121, YV-10122, YV-10124 and YV-10125 are closed. To control the flow downstream of the compressor, a recirculation loop is designed in the line above the compressor that includes the PV-10141 and PCV-10140 valves (another loop where FV-10142 is present in order to regulate the loop manually in case of breakage of PV-10141).

- *Separation phase I*: The separation phase must be further separated into two distinct instants. When the tank is fully loaded during the initial phase (separation I), the nominal pressure of the two recovery systems is lower than that of the tank, therefore any movement will be "natural," or brought on by the difference in pressure between the two different parts of the plant. There is a mass

flow meter (XMFC-10160) located just before the accumulation-separation connection, which enables a consistent flow rate to be input. While the loop made of HV-10115 and PICV-10143 is required to stabilize the pressure upstream of XMFC-10160 (Which is higly sensible to pressure fluctuations). The valves YV-10121 and YV-10125 are open during this initial sub-phase, whereas YV-10120, YV-10122, YV-10123, and YV-10124 are closed.

- *Separation phase II*: The gas must travel through the compressor when the pressure inside the storage system is lower than the one downstream (separation II) in order to discharge the tank down to atmospheric pressure. Valves YV-10120, YV-10121, YV-10123 are closed, but YV-10122, YV-10124 and YV-10125 are all open.

Table 4.4 Resumes pneumatic and manual valves'position.

Table 4.4 Pneumatic valves positions during different phases

Valve ID	Accumulation	Separation I	Separation II
YV-10120	Open	Close	Close
YV-10121	Close	Open	Open
YV-10122	Close	Close	Close
YV-10123	Open	Close	Close
YV-10124	Close	Close	Open
YV-10125	Close	Open	Open

After briefly describing this section, the selection of the storage tank marks the start of the study and design. For tank sizing, a lot of information is needed, such as the design volume (V_D), operating pressure and temperature (P_{op} and T_{op}), maximum and minimum pressure and temperature, and mixture composition (particularly important for downstream separation). With relation to the volume required, this was assessed using the following data. The amount of used to flush the detector chamber (RICH-1) during the filling is around 16 Nm^3. Consequently, this is also the amount of gas to be held in the tank. In order to reduce the tank's size, it was decided to choose a design pressure of 7 bara. With this option, it is possible to choose a tank that is significantly smaller (dimensions are lowered by 7 times if the mixture is approximated as an ideal gas). Using the following correction factors k_g and k_T (Equations 4.3 and 4.4), the design volume of the tank was enlarged after

assuming, with a forced approximation, that the mixture was ideal and needing to account for variations in the specific volume (V_m) with temperature.

$$k_T = \frac{P_{atm}\, V_m(100C)}{P_{op}\, V_m(20C)} = 0.21 \tag{4.3}$$

$$V_D = k_g\, k_T\, V_n = 3.4\, m^3 \tag{4.4}$$

Where k_T and k_g are the correction factors accounting respectively for temperature variation and non-ideality of the mixture, $V_m(T)$ is the specific volume of the mixture (76% mol in C_4F_{10}) at temperature T as displayed in Table 4.5. P_{op} and P_{atm} are respectively operative and atmospheric pressures and V_n is the volume required at normal conditions.

Table 4.5 Specific Volume and Density of the Mixture (76% mol in C_4F_{10}, P_{op}) as a Function of Temperature.

Temperature (T, °C)	Density (ρ, kg/m^3)	Specific Volume (Vm, m^3/kg)
20	6.955	0.144
40	6.489	0.154
60	6.083	0.164
80	5.726	0.175
100	5.410	0.185
120	5.128	0.195
140	4.874	0.205
160	4.644	0.215
180	4.436	0.225
200	4.245	0.236

Furthermore, in Figure 4.8 is reported a technical draw of the accumulation tank.

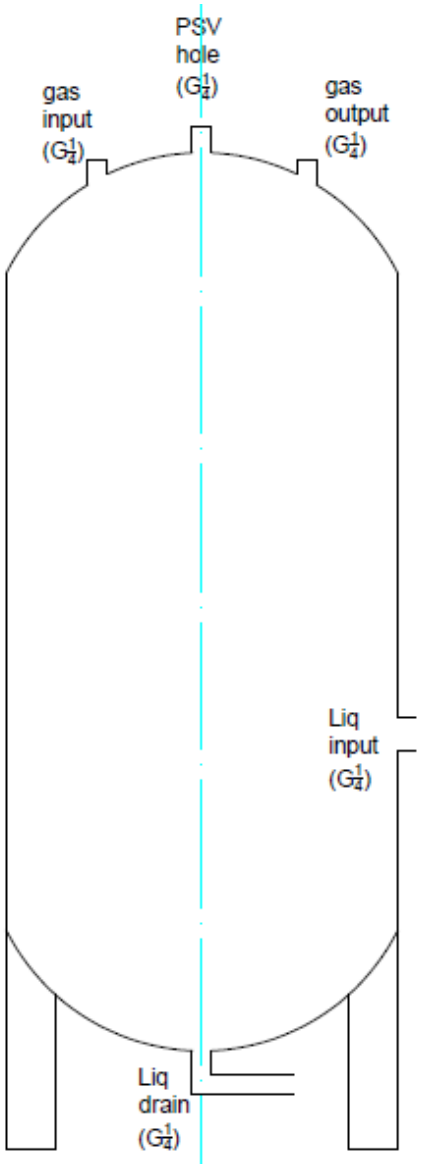

Fig. 4.8 Technical Sketch of the Accumulation Tank.

It becomes important to specify out that the post-compression conditions, which will be covered in the paragraph after this one, are what's responsible for such a significant temperature fluctuation. As there is a system that pre-cools the compressed gas before it enters the accumulation tank downstream of the compression, as a result, under normal working conditions, the maximum temperature of 100 °C is not reached. Moreover, the tank is connected to two pressure safety valves (PSV-10130 and PSV-10131) by a three-way valve (needed for maintenance) and can bear a maximum pressure (P_{max}) of 10 bar as a further layer of safety. The design

of the compression system follows the establishment of the storage conditions for the gaseous mixtures. This plant element consists of a compressor and several air to open pneumatic valves to regulate the lines opening and closing conditions. This section fulfills two purposes. Since the working pressure upstream of the separation system varies between 1.3 and 1.7 bar, the compressor's main task is to compress the gas before it flows into the tank (accumulation phase). Secondly, it serves as a gas booster during phase II of separation.

The compressor must be chosen while taking into account several needs. First off, the mixture's composition that has to be compressed changes instantly during the accumulation phase. In fact, at boundary conditions, the gas entering the inlet is, assuming its filling process, almost pure CO_2 during the early hours and pure C_4F_{10} at the closing hours. Important issues arise up in both scenarios.
At a pressure of 7 bar, a gas that almost entirely consists of C_4F_{10} condenses at temperatures below 62 °C. Therefore, it could be required to preheat the gas in line to prevent the production of liquid inside the volumetric machine. The following relations are produced (Figure 4.9) as a preliminary approximation assuming a polytropic compression with a 75% overall efficiency. Even though, this validation must be done experimentally.

When, instead, the mixture is almost totally CO_2, due to an extreme Joule-Thompson's effect [29], a massive heating phenomenon occurs (Figure 4.10). In this case a post-cooling is required to avoid feeding hot gas into the tank

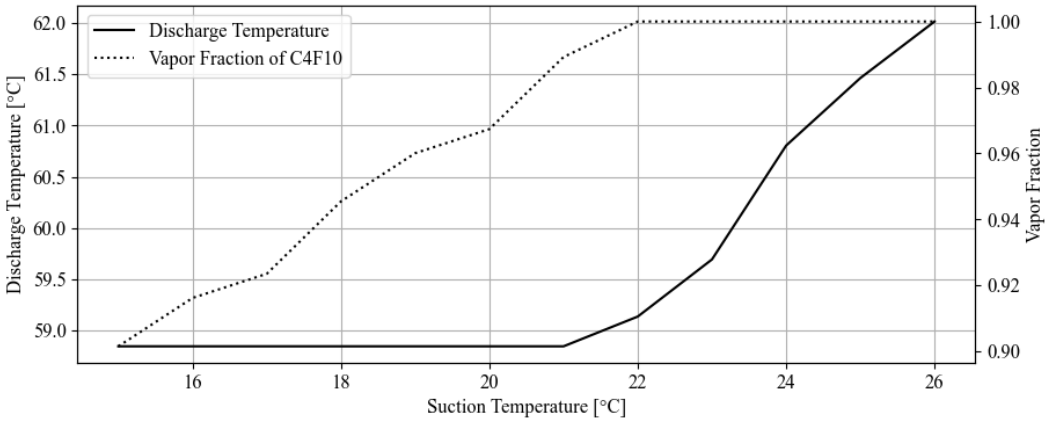

Fig. 4.9 Post-compression discharging temperature and vapor fraction of C_4F_{10} (when compressed from 1 to 7 bara) as a function of suction temperature.

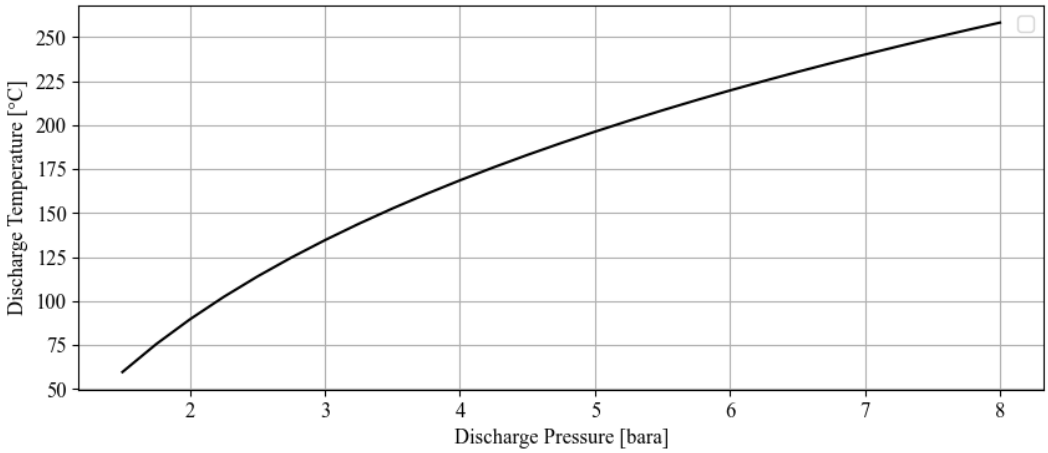

Fig. 4.10 Post-compression discharging temperature of CO_2 as a function of discharging pressure (when suction temperature is 25°C).

A compressor with an inter-refrigeration system might be purchased to address the second of the two criticalities. The compressor employed (Table 4.6) does not include a process fluid cooling system because it was decided to place more emphasis on the condensation issue. As a fact, the compressed gas will naturally cool down along the pipelines.

Table 4.6 Features of HAUG.Pluto 11E 26 D4 (SOGX 26-D4) Compressor

Compressor Model	HAUG.Pluto 11E 26 D4 (SOGX 26-D4)
Oil-Free	Yes
Power (kW)	0.55
Angular Speed (1/min)	1400
Min. Suction Pressure (bara)	0.8
Avg. Suction Pressure (bara)	2
Max. Discharge Pressure (bara)	11
Max. Flowrate at Avg. Suc. P. (m^3/h)	3.3

4.4 Design of the Double Equilibrium Stage

4.4.1 Introduction and Working Principles

As stated in the previous sections, it was decided to move on with the development of a parallel system while also designing a distillation column. The system is made up of a pair of equilibrium stages that operate at different thermal conditions; in reality, the first stage serves as a partial condenser. The condensate from the first stage that is richer in C_4F_{10} partially evaporates in the second stage. In order to illustrate how this system works, the process diagram in Figure 4.11 can be used.

The mixture exiting the accumulation tank reaches the separation system in the upper right part of the diagram (S0). Once it enters, the mixture continues to the left and enters a plate heat exchanger where it is cooled down and partially condensed. A series of temperature sensors (TE-10380, TE-10385, TE-10482, and 10483) are present to constantly monitor the temperature of the process stream and the incoming and outgoing refrigerant in the heat exchanger. The two-phase equilibrium mixture reaches the first buffer, also monitored by temperature and pressure sensors and indicators (TE-10381, TI-10382, PT-10371, and PI-10370). From the head of the first equilibrium buffer, the exhaust gas stream is obtained, and its flow rate is regulated by a back pressure valve (PCV-10340), which opens when the pressure monitored by PT-10371 exceeds its set point pressure. Finally, on the exhaust line, there is a pressure safety valve (PSV-10330) that puts the system into safety mode in case of overpressure and a line for analyzing the exhaust composition and to verify that the amount of exiting n-decafluorobutane is below predetermined thresholds.

The flow rate of the liquid exiting the bottom of the first equilibrium stage is controlled by the presence of a level transmitter (DPT-10390), which can monitor the liquid level by measuring the pressure difference at the top and bottom of the tank, and a control valve (YV-10320). The condensate then enters the second vessel (T-101), where, thanks to the presence of an electric resistance, it is partially vaporized. The supply of heat is intended to strip out the dissolved carbon dioxide in the liquid and obtain a bottom product rich in C_4F_{10}. Here too, pressure and temperature sensors and indicators allow for the monitoring of both variables. In particular,

sensor PT-10374, coupled with the re-compression loop, regulates the tank's pressure by varying the vapor flow rate expelled from the top.

The operating temperature of the vessels is crucial for managing the purity and recovery of the product. The thermal conditions of the bottom buffer are also essential for the recirculation flow rate. In fact, to maximize the purity of the liquid decafluorobutane, it is necessary to recirculate the overhead vapor. The greater the heat provided by the electric resistance, the greater the magnitude of recirculation. In this case, to ensure a constant pressure upstream of the system, the gas is re-compressed to the initial pressure conditions, and a check valve (HV-10318) prevents back-mixing between the fresh feed and the recirculated stream. Again, the compression loop is managed by pressure sensors and pneumatic valves, as described in the introduction of Section 4.3.

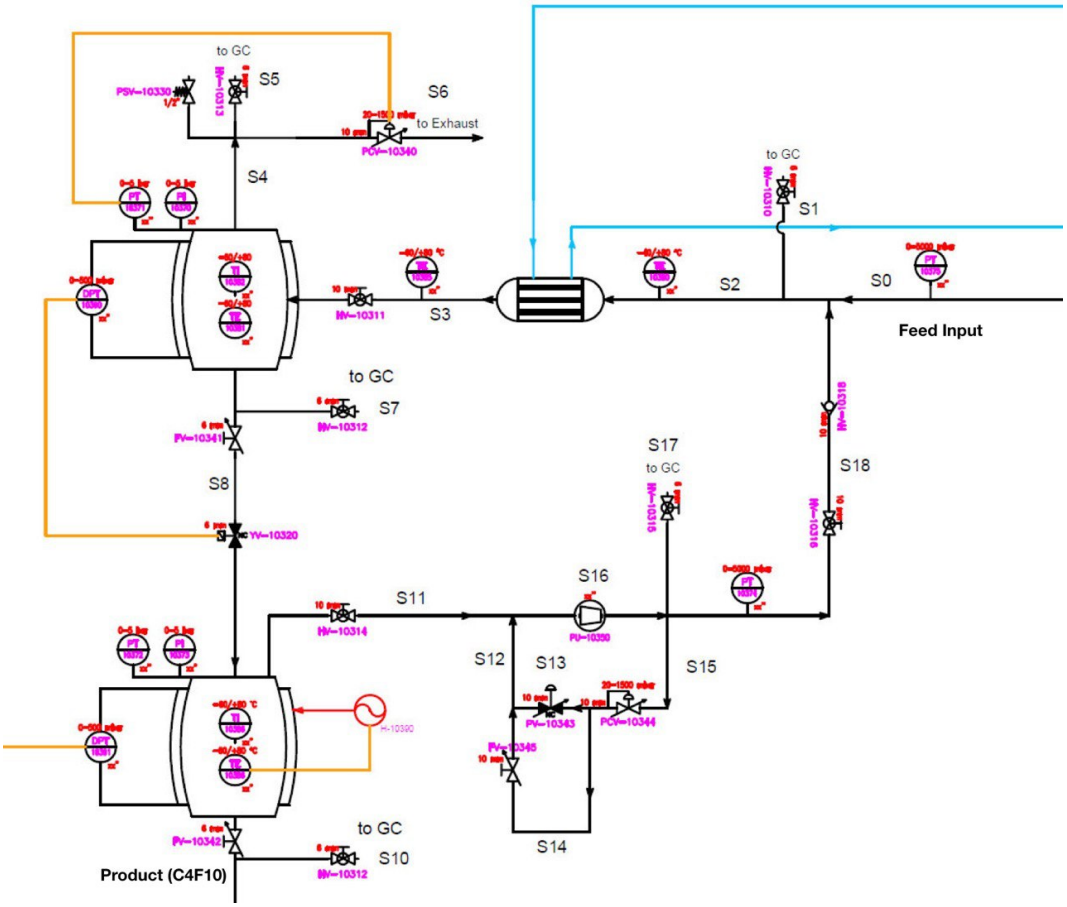

Fig. 4.11 New Double Stage Section (Appendix B).

4.4.2 Feed Conditions

Understanding the feed conditions is crucial before moving on with the design of the recovery systems. Given that the feed (F) comes from the storage tank, the state of the mixture inside the tank itself defines the nature of the current. Currently, a heat exchanger can be installed upstream of the systems, and the discharge pressure of the compressor can be adjusted to adjust pressure and temperature. However, it is impossible to predict in advance what the compositions will be at the end of the accumulation period. The feed's composition must then be estimated.

With filling information for the first half of 2023, the forecast was generated. In fact, both plenty of gas-chromatographic analyses of the C_4F_{10} flow rates input to the system as well as the current fed to the partial condensation stage are available. Given the flow rate fed and the volume percentage of C_4F_{10} during the filling phase (Figure 4.12) it is possible to produce cumulative curves that can be used to estimate both the volume of gas actually fed into the system and the fraction of C_4F_{10} that is likely to exist at end of the accumulation phase (Figure 4.13). The nominal volume is pretty close to the 16 Nm^3 that have been previously declared. Nominal volume (V_s) and volume fraction of C_4F_{10} (Z_s) are calculated as:

$$V_s = \sum_{i=1}^{N_{\text{hours}}} V_i = 16.21\,\text{m}^3 \tag{4.5}$$

$$Z_s = \frac{V_n}{\sum_{i=1}^{N_{\text{hours}}} (x_i V_i)} = 76.9\% \tag{4.6}$$

Where V_i and x_i are the volumetric flowrate (Nm^3/h) and the volume % of C_4F_{10} (mol/mol) in the i^{th} time interval, while N_{hours} is the number of operating hours

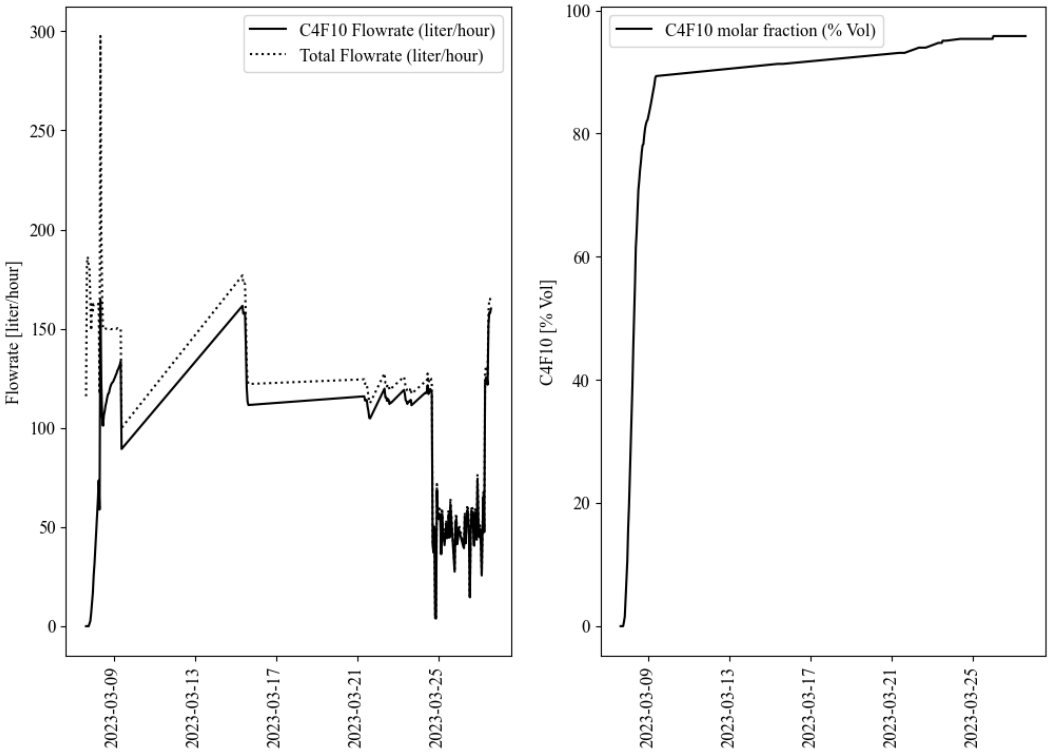

Fig. 4.12 Flowrates and compositions fed to the separation units.

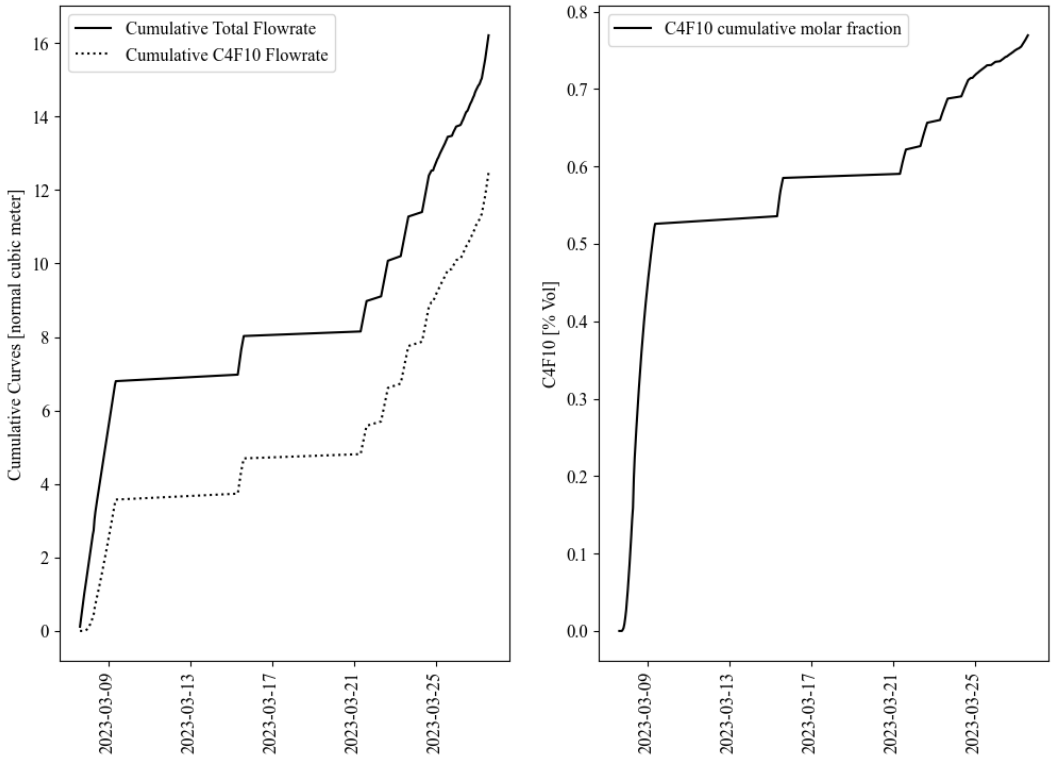

Fig. 4.13 Cumulative flowrates and C_4F_{10} volume percentage expected in the accumulation tank.

4.4.3 Simulation and Optimization

The temperature of the two buffers, as was noted in the system description, is the variable that has the most impact on the system's efficiency, as measured by the liquid product's purity (Eq. 3.1) and recovery (Eq. 3.2). In reality, a rise in temperature for a given input composition results in:

- An increase in the gas flow rate and a decrease in the liquid one.
- An increase in the molar fraction of C_4F_{10} in the liquid phase, with a corresponding rise in purity.
- A decrease in recovery due to an increase of C_4F_{10}'s fraction in the vapor phase.

Therefore, optimizing the temperature of the two buffers is the key element to maximize both initial requirements. Before defining the design specifications, in

order to clearly understand the effect of this variable on the system, we proceed with the illustration of some results obtained through the use of Aspen Plus. In fact, the choice of the optimal operating conditions has been obtained through a series of simulations that follow an algorithm described in Figure 4.14.

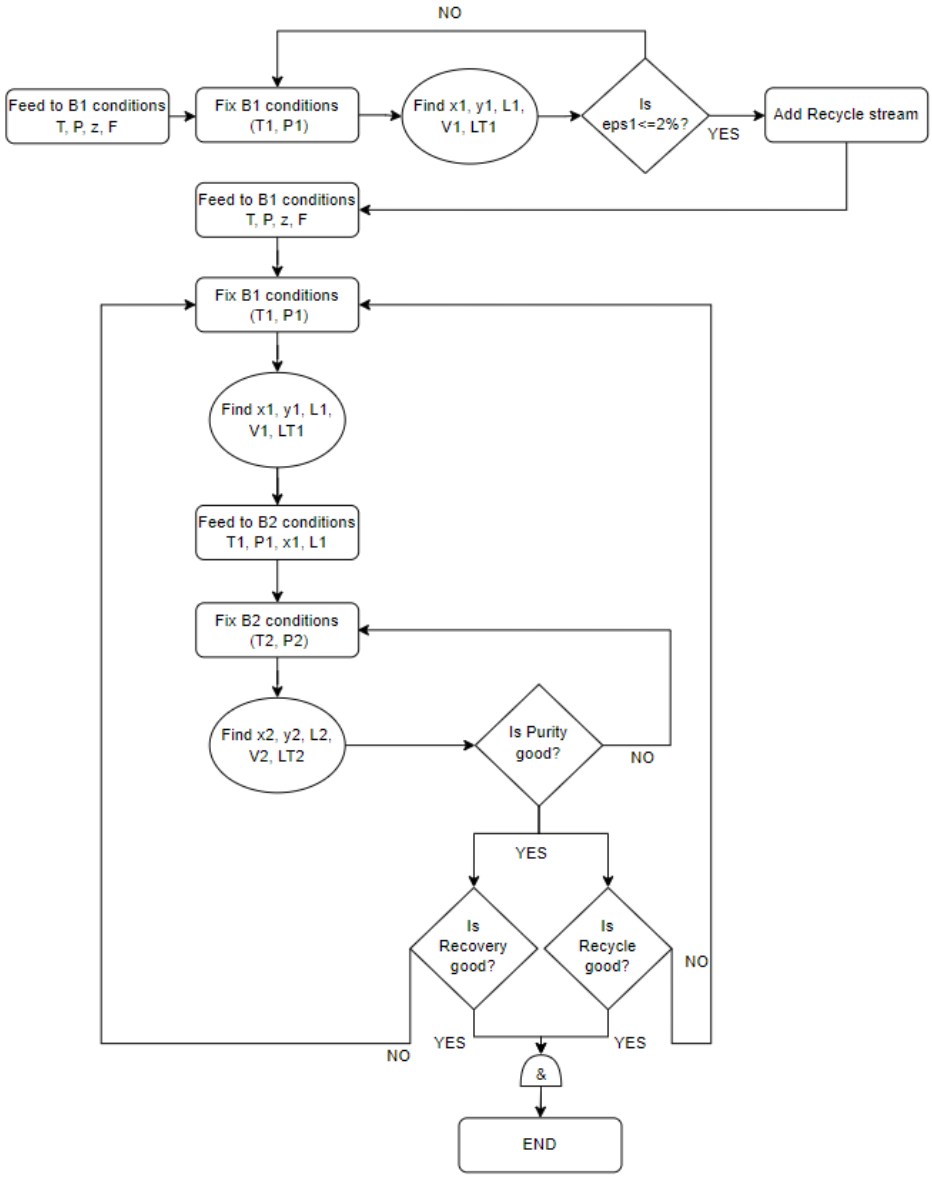

Fig. 4.14 Optimization algorithm defined to find out the best temperatures of the buffers.

The operating temperature of the first buffer (T_1) is set based on the inlet conditions (Table 4.7), which then affect the flow rates (V_1, L_1) and compositions (y_1, x_1) of the vapor and liquid streams leaving the first stage. The temperature in this situation must ensure that the amount of C_4F_{10} lost in the exhaust stream is less than a predetermined threshold, ε_t, set at 2%:

$$L_{C4F10} = \frac{y_1 \cdot V_1}{z \cdot F} < \varepsilon_t \tag{4.7}$$

Table 4.7 Fresh Feed Conditions

Fresh Feed Temperature (°C)	Fresh Feed Pressure (bara)	Fresh Feed C_4F_{10} Molar Fraction (z, mol/mol)	Fresh Feed Flowrate (F, mol/h)
25	2.5	0.769	50

It should be noted that the temperature range that satisfies this limitation only applies to situations without recirculation current. It's fascinating to see how temperature significantly affects the essential factors (Figures 4.15 and 4.16). As a result, a preset temperature of -40°C is used since it is impossible to predict the temperature in advance, and the algorithm's second cycle is forced by adding the recirculation current. The stream of vapor that exits the second buffer's head (V_2) and is blended with new feed before returning to the first buffer is the recycle.

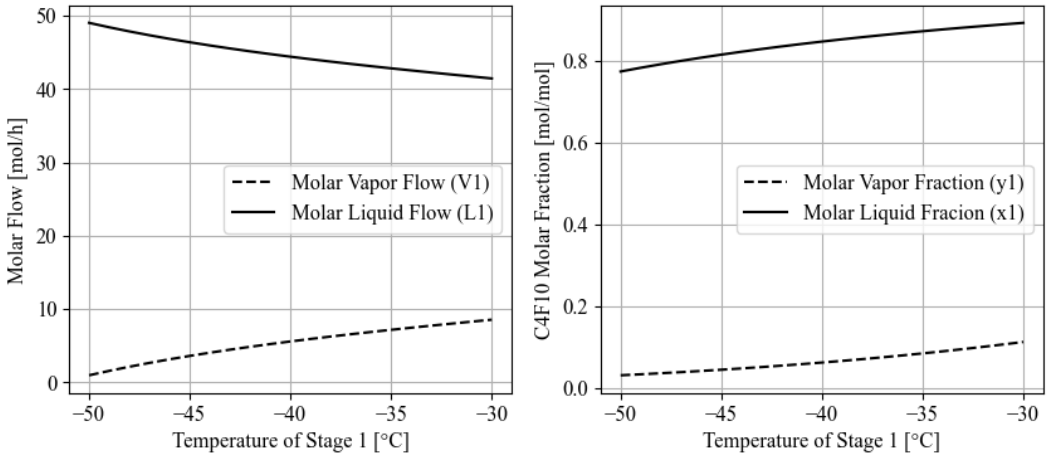

Fig. 4.15 Effect of First Stage Temperature (T_1) on Molar Flows exiting the first buffer (left-side chart) and on their compositions (right-side chart) when recycle stream is not present.

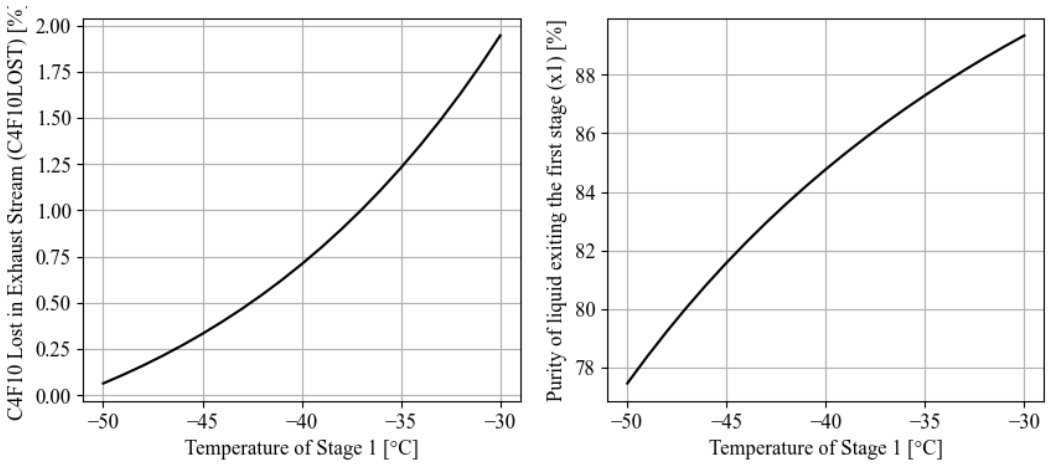

Fig. 4.16 Effect of First Stage Temperature (T_1) on C_4F_{10} lost in the exhaust stream (exhaust corresponding to V_1) and purity of liquid exiting the first stage (x_1) when recycle stream is not present.

Analyzing the contents of Figure 4.15 , it is possible to note that an increase in temperature of the first stage corresponds to:

- An increase in the exhaust flow (V_1) and a reduction, due to the material balance, in the liquid one (L_1).
- An increase in the molar fractions of C_4F_{10} both in the liquid phase (x_1) and in the vapor phase (y_1).

Even more interesting are the trends shown in Figure 4.16, which show that an increase in T_1 is associated with:

- A greater amount of C_4F_{10} lost. This occurs as the flow rate of exhausted steam (V_1) increases.
- Greater purity of the condensate at the first buffer, in fact the relative volatility between the two components favors the formation of CO_2 vapors compared to those of C_4F_{10}.

It is now interesting to investigate how the temperature of the second buffer affects the final requirements by turning on the loop stream (equivalent to V_2, head vapor of the second buffer). In practice, the first buffer is given three temperature values (T_1 equal to -35, -40, and -45 °C), and among these, fixing one at a time, the temperature of the second buffer (T_2) is varied and the change of the recycle (V_2) and product (L_2) currents as well as the relative molar fractions of C_4F_{10} (y_2 and x_2) are studied. Figures 4.17 and 4.18 show the outcomes of these simulations.

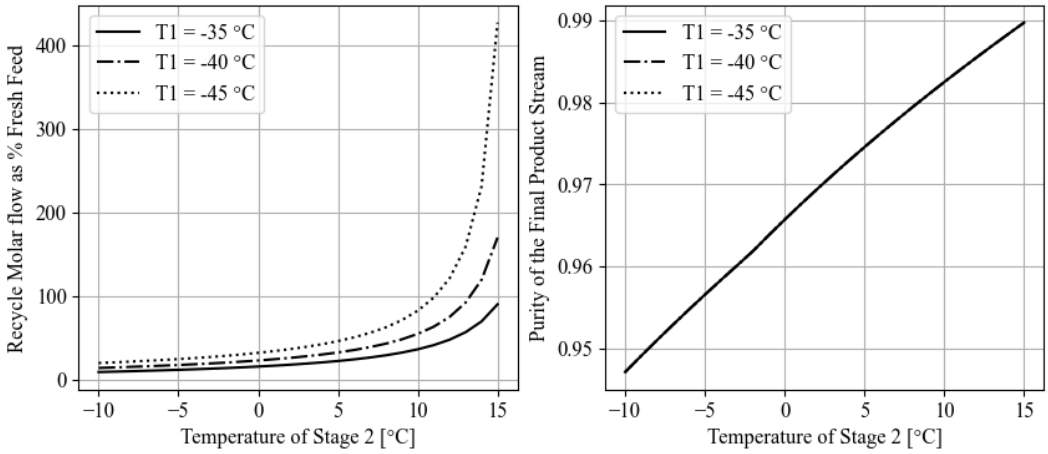

Fig. 4.17 Effect of Second Stage Temperature (T_2) on the ratio between the molar flow of recycle stream, V_2, and fresh feed (left-side chart) and purity of liquid exiting the second stage, x_2 (right-side chart) when recycle stream is turned on.

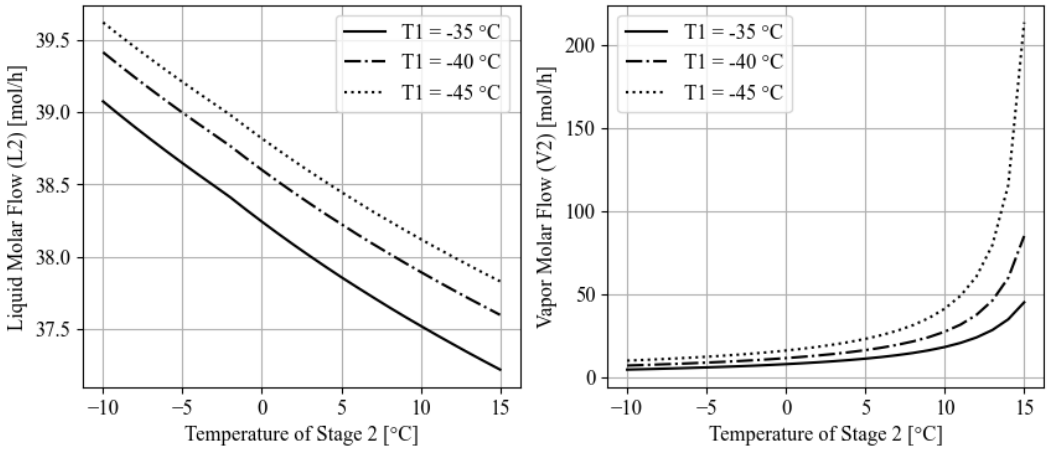

Fig. 4.18 Effect of Second Stage Temperature (T_2) at different temperatures of the first stage (T_1) on: (left-side chart) liquid molar flow exiting the second buffer (final product stream, L_2); (right-side chart) vapor molar flow exiting the second buffer (recycle stream, V_2) when the recycle is turned on.

These charts demonstrate that, for a given temperature T_1, an increase in T_2 results in a greater purity of the final product. On the other hand, greater purity necessitates a dramatic increase in recirculated flow, especially above the 10°C threshold where the curves transition from a linear trend to a strongly exponential one. On the other hand, fixing the operating parameters of the first buffer has an impact on the outcomes when the temperature of the second buffer is kept constant; in fact, at a given T_2:

- The linear-exponential transition of recirculation current's flow is anticipated with a decrease in T_1, and the rate of exponential growth is also accelerated. As a result, greater flow rates must to be handled, which will increase the cost of pumping and thermal energy for the condensation and partial vaporization stages.
- On the other hand, by decreasing T_1, productivity increases, as with constant T_2 and x_2, the liquid flow rate curves shift upwards, thus guaranteeing a greater quantity of C_4F_{10} produced per unit of time.
- Finally, it is observed that the purity of the product is almost a function of T_2 only. This can be explained by returning our attention to Figure 4.15 (right-side chart). It should be observed that between -35 and -45°C the variation

of the molar fraction of C_4F_{10} leaving with the condensate (corresponding to the mixture fed to the second buffer, L_1) is less than 5%. Therefore, the variation of the initial composition on the composition of the outgoing product is negligible compared to the effect associated with a change in temperature.

Following the end of these considerations, the chosen operating conditions and the final simulation results are displayed in the following table (Table 4.8).

Table 4.8 Designed Temperatures and Results with Aspen Plus

Stage 1 Temperature (°C)	Stage 2 Temperature (°C)	Recycle to Fresh Feed (molar) Ratio (R/F)	Recovery (R_{C4F10})(%)	C4F10 Lost in the Exhaust (L_{C4F10})(%)	Purity of the Product Stream (P_{C4F10})(%)
-42	12	409.60%	98.29%	1.71%	96.71%

The ultimate goal of this project is to optimize both the recovery and the purity of the product to the greatest extent, even if the final operational options have the highest costs in terms of energy and capital investment (since the flow rates to be processed are larger). As a result, in accordance with the requirements established and reviewed by the project team, the choice of these circumstances is still appropriate.

4.5 Design of the Distillation Column

4.5.1 Introduction to the Distillation Process

One of the most used separation techniques in the process industry is distillation. Inside a column, a mass transfer takes place between a liquid phase and a vapor, formed by supplying or subtracting heat from the starting mixture. The two phases move counter-current inside the apparatus in order to enrich the vapor of the more volatile components and the liquid of the heavy species. The splitting process is easier when the relative volatility of the components to be separated is high; in other words, given an operating pressure, the distillation process is more effective when the key components have remote boiling temperatures [18].

A distillation column has three key elements:

- *Reboiler*: This is a heat exchanger that enables continuous vaporization of column bottom liquid. Part of the liquid is extracted as bottoms product, while the remaining fraction it is vaporized, and reintroduced into the column (boil-up vapor).

- *Condenser*: This is a heat exchanger that connects to a volume (reflux drum) where the above product is either completely or partially condensed (total and partial condenser respectively). The overhead product splits into distillate and reflux after being condensed. The reflux to distillate ratio (R_R) is a significant metric.

- *Column*: The column is the primary structural element of the system and act to broaden the surface contact area between the two phases, ensuring higher mass and heat transfer capabilities. To ensure a high heat and mass exchange surface the internals of the columns are highly engineered and can be divided into two subgroups: (1) plate columns, and (2) packed columns. Since plate columns are utilized more frequently, the mathematical models discussed use the first sub-family. In Figure 4.19 a basic scheme of a trayed distillation column is reported.

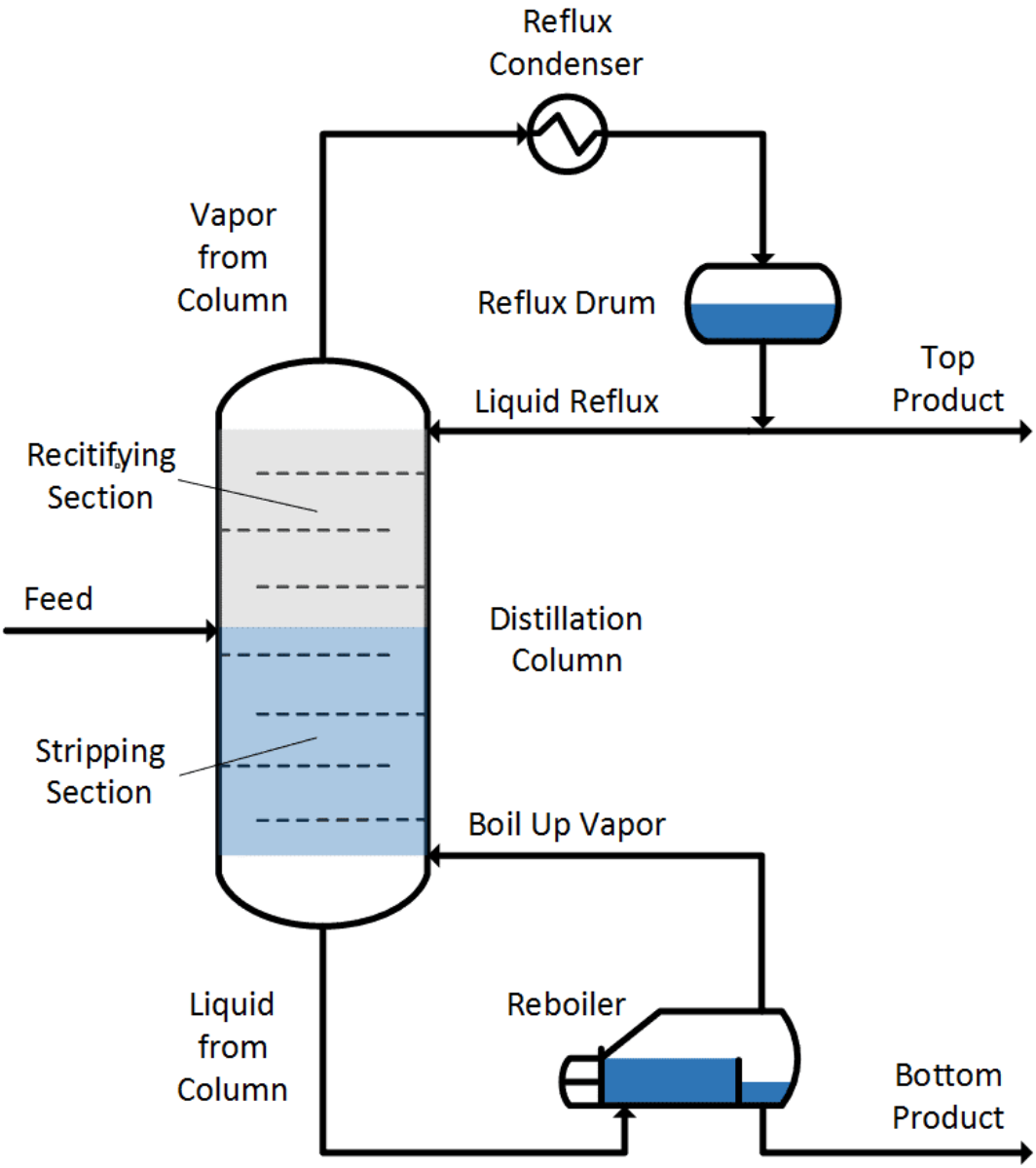

Fig. 4.19 Scheme of a trayed distillation column [30].

4.5.2 MESH Equations and Degrees of Freedom

Liquid-vapor equilibrium is the foundation of the distillation process (exhaustively discussed in section 3.1). Each plate in a column can be assimilated to a stage of theoretical equilibrium (Figure 4.20).

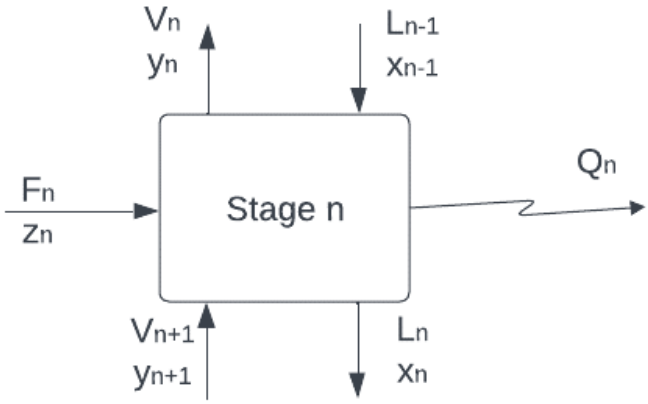

Fig. 4.20 Counter-current mass and heat flows in a generic stage of a distillation column.

Four equations can be written for each theoretical stage, n, and component, j. (MESH equations: Mass balance, Equilibrium, Summation and Heat balance) [15].

1. Mass Balance:

$$V_{n+1}\, y_{j,n+1} + L_{n-1}\, x_{j,n-1} + F_n\, z_{j,n} = V_n\, y_{j,n} + L_n\, x_{j,n} \tag{4.8}$$

2. Equilibrium Relationship: obtained by Equations 3.3, 3.4 and 3.5.

$$x_j\, \gamma_j\, P_{s,j} = y_j\, \Phi_j\, P \tag{4.9}$$

3. Summation: stating that the sum of the molar fractions of all the component is unitary in each phase.

$$\sum_{j=1}^{N_c} x_{j,n} = \sum_{j=1}^{N_c} y_{j,n} = 1 \tag{4.10}$$

4. Heat Balance:

$$V_{n+1}H_{n+1} + L_{n-1}h_{n-1} + F_nJ_n = V_nH_n + L_nh_n + Q_n \tag{4.11}$$

Where V_n and L_n are the vapor and liquid flowrate exiting from the n^th stage (mol/s), F_n is the molar flowrate of the feed (mol/s), z_n is the molar composition of

the feed (mol/mol). H_n and h_n are respectively the enthalpy of the vapor and liquid streams (J/mol), J_n the enthalpy of the feed stream (J/mol) and Q_n the heat flux exchanged between the column and the surroundings (J/s). Finally n represent the generic stage and N_c the total number of components.

Rigorous methods are built around this set of equations, which can be written for each stage, including the reboiler and the condenser. The estimation of the temperatures at each stage, on the other hand, requires the calculation of the liquid boiling and vapor condensation temperatures. In these conditions, it is necessary to saturate a number of degrees of freedom equal to the number of components plus six in order to define the problem univocally (Table 4.9).

Table 4.9 Number of variables influencing the design of a distillation column.

Variable	Number of Independent Variables	Design Phase
Feed Composition	$N_c - 1$	Known
Feed Flowrate	1	Known
Feed Enthalpy	1	Known
Pressure (head)	1	Fixed
Condenser Duty	1	Unknown
Reboiler Duty	1	Unknown
Composition of CO2 in Distillate	1	Fixed
Composition of C4F10 in Bottom	1	Fixed
Distillate Flowrate	1	Fixed
Bottom Flowrate	1	Fixed
Number of Stages	1	Unknown*
Reflux Ratio	1	Unknown*

*One must fix either the reflux ratio or the number of stages in order to solve the problem

4.5.3 Defining the Specifications and the Goals

As briefly introduced in Table 4.9, the design phase of a separation system based on the distillation principle requires knowledge of specific parameters. In the case under consideration, these parameters are the composition, flow rate, and thermal conditions of the feed. With these known, in order to constrain the degrees of freedom, it is necessary to fix other key parameters. The choice of these variables varies, but

as a general rule, it is customary to fix the operating pressure (with reference to the column's head), as well as the two desired outlet flows, namely the distillate (D) and bottom (B) flow rates. Finally, the reflux ratio or number of theoretical stages must be fixed. Clearly, the choice of which variable to fix remains somewhat arbitrary and depends on the objectives and specifications set. To obtain results as close to reality as possible, the simulation of the system under study was performed using Aspen Plus. Within the software, it is possible to simulate distillation processes based on the principles of thermodynamic equilibrium and, when possible, i.e., in the presence of experimental data, also based on kinetic modeling. Before proceeding with the description of the simulations conducted and the results obtained, it is important to understand the key variables involved.

In this project, the main objectives are: (1) to maximize the purity of the bottom product and (2) to achieve the highest possible recovery. For these reasons, among the various variables, it is evident that it is useful to fix, in addition to the pressure at the top of the column, the bottom column flow rate, or more precisely, the so-called bottom to feed ratio (B/F). Indeed, setting a B/F equal to the feed product flow rate is a wise choice. Assuming it is possible to obtain a pure bottom column product, a 100% recovery will also be achieved. In contrast to what was said earlier, in practice, it is typical to set initial values for the reflux ratio and the number of theoretical stages and then, iteratively, arrive at their optimal values. It is known that the minimum number of stages is obtained under conditions of total reflux (infinite reflux ratio), and conversely, increasing the number of stages results in decreasing values of the reflux ratio (while keeping all other specifications constant).

At this point, we proceed with the selection of these parameters. The choice depends on a set of considerations that will be described individually.

- *Operating Pressure*: The operating pressure plays a key role in the process. In general, higher pressure makes the separation more challenging. Increasing the pressure causes the dew and bubble lines described in the binary diagrams (Section 4.1) to approach each other. Conversely, the vaporization temperature of the components in the mixture increases with pressure. In applications like this, where the transition temperatures at atmospheric pressure are below zero degrees Celsius, operating at low pressures incurs high energy costs.

Therefore, we set an initial value of approximately 2.5 bara. This choice allows condensing the distillate at around -70°C and vaporizing the bottom product at about 20°C.

- *Bottom to Feed Ratio (B/F)*: Given the composition of the feed mixture (Section 4.4.2), a B/F equal to the molar fraction of C_4F_{10} in the feed is fixed.
- *Number of Equilibrium Stages (N) and Reflux Ratio (R_R)*: The number of equilibrium stages is determined iteratively. In this application, the minimum number of stages is firstly selected (three stages, where the first and third are the condenser and reboiler, respectively). After fixing the number of stages (which is increased at each iteration), the reflux ratio is varied and the impact of this sensitivity analysis on the purity and recovery of decafluorobutane is observed. The results of this sensitivity analysis are reported in Figures 4.21, 4.22, 4.23, and 4.24.

Before describing the figures below, it is important to make a brief digression. As mentioned in sections 2.2 and 2.4, the system must be able to handle both the filling and emptying phases. The composition during the filling phase has been extensively discussed, thanks to the availability of data from the first semester of 2023. However, for the management of the emptying phase, it is necessary to assume that the composition of the mixture to be processed is symmetric with respect to that of the filling phase. Therefore, an inlet mixture with a 24% molar fraction of decafluorobutane will be used. Since the column must be able to handle both conditions, it is necessary that: (1) the chosen number of stages (as a non-modifiable variable once the column is built) is sufficient to meet the specifications in the worst of the two cases, and (2) the B/F and R_R change depending on the case.

The selection of the number of equilibrium stages is now described in order to fulfill the following specifications: (1) P_{C4F10} greater than 99.9%, (2) R_{C4F10} greater than or equal to 99.5%. From Figures 4.21, 4.22, 4.23, and 4.24, it is evident that purity and recovery increase with the number of stages and reflux ratio. Specifically:

- In the emptying phase (Figures 4.21 and 4.22) the dependence of purity and recovery on the number of stages decreases as this parameter increases. In other words, there is no improvement in performance for a number of stages

greater than 5. The same applies to the reflux ratio. Once the number of stages is fixed, using a reflux ratio greater than 3 does not result in significant changes. In fact, the curves reach a horizontal asymptote.

- In the filling phase (Figures 4.23 and 4.24) similar trends are observed. The only difference is that the curve associated with a number of stages equal to 4 tends to overlap with the curves of 5 and 6 stages when the reflux ratio exceeds a value of 4.

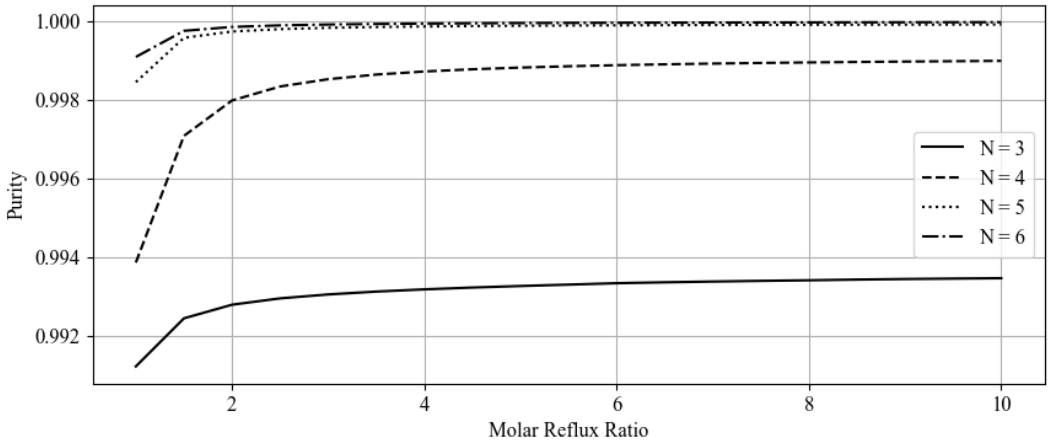

Fig. 4.21 Purity (molar fraction of decafluorobutane) of the bottom product during the emptying phase as a function of N and R_R.

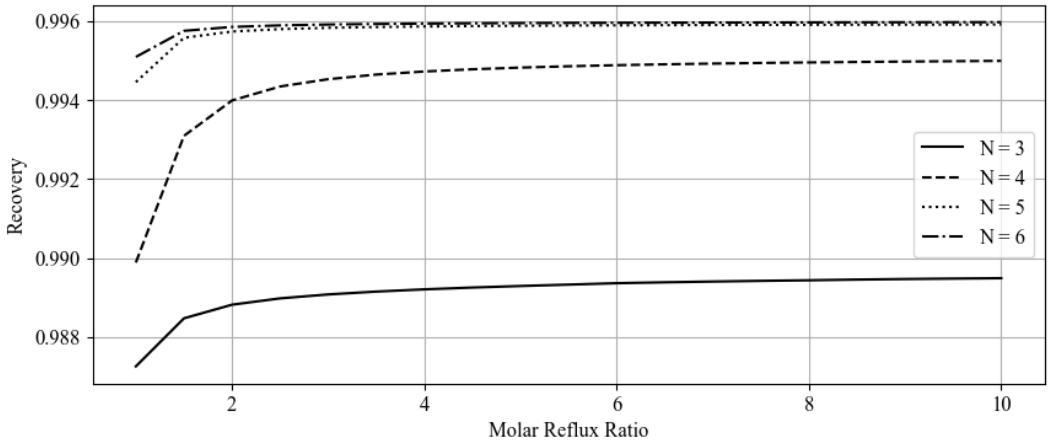

Fig. 4.22 Recovery during the emptying phase as a function of N and R_R.

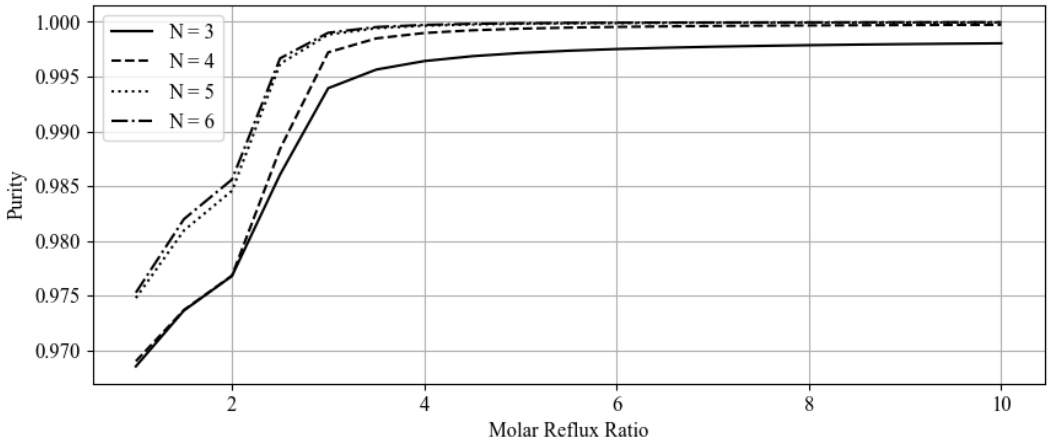

Fig. 4.23 Purity (molar fraction of decafluorobutane) of the bottom product during the filling phase as a function of N and R_R.

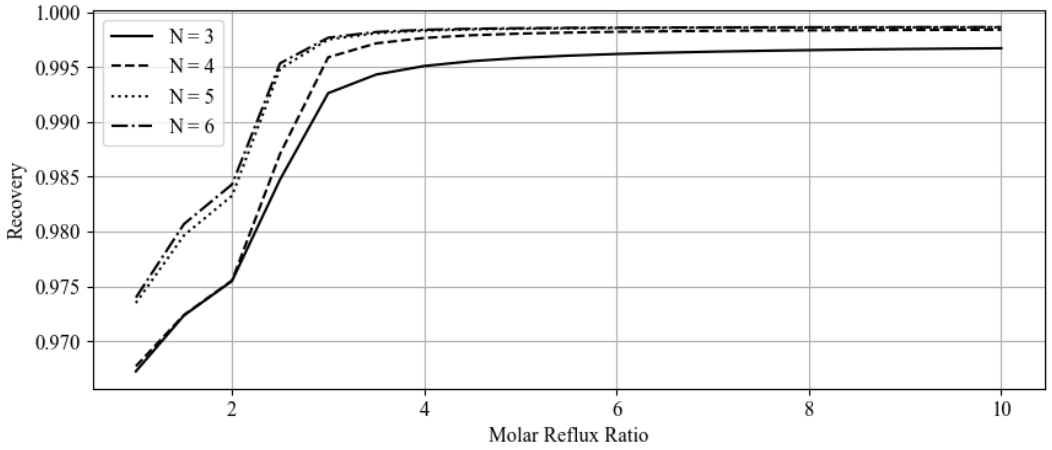

Fig. 4.24 Recovery of the bottom product during the filling phase as a function of N and R_R.

If one were to analyze only these graphs, it would be evident that increasing indefinitely N and R_R is the best choice. However, it is important to consider that: (1) an increase in the number of stages leads to higher capital costs, and (2) increasing the reflux ratio results in higher utility consumption and, consequently, higher operating costs. Assuming that the number of stages has no significant impact on the duties of the heat exchangers, it is clear that (Figures 4.25 and 4.26) a linear relationship between the reflux ratio and the thermal power to be supplied (or removed in the case of the condenser) exists.

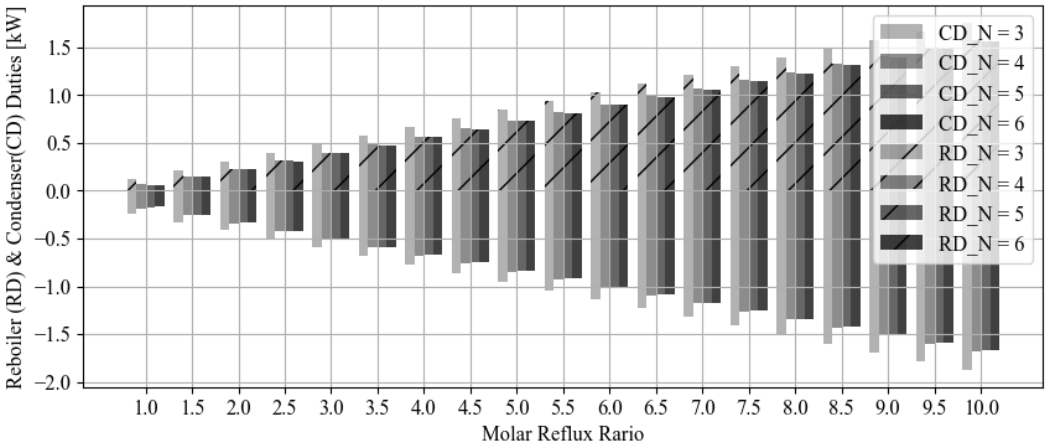

Fig. 4.25 Reboiler (RD) and Condenser's (CD) duties during the emptying phase as a function of N and R_R.

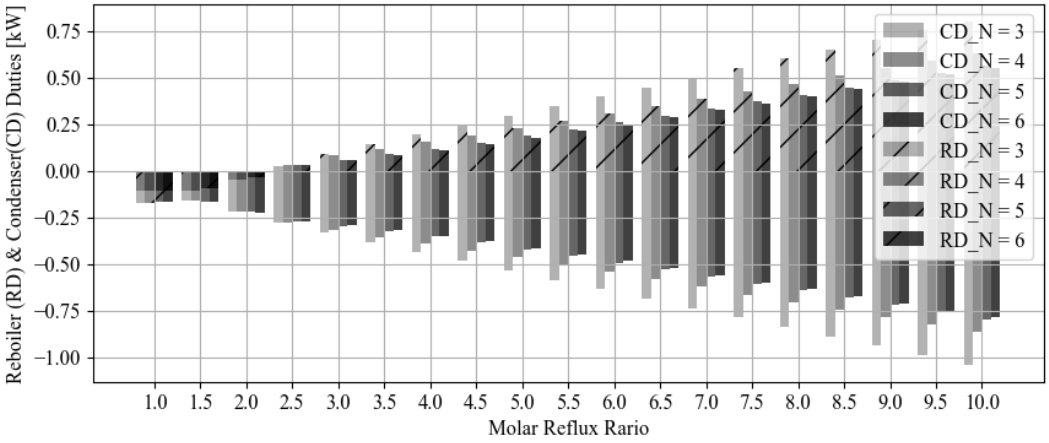

Fig. 4.26 Reboiler (RD) and Condenser's (CD) duties during the emptying phase as a function of N and R_R.

Taking these considerations into account, it has been decided to fix the number of stages at 5. In both phases, there is no observed improvement in performance by increasing the number of stages. The (theoretical) reflux ratio is set to 3, since at this value the curves reach a plateau. To ensure proper operation, it was decided to increase the reflux ratio to 4 through the addition of a correction factor. Tables 4.10 and 4.11 resumes the simulations' results.

* Purity and recovery refers to a simulation where $R_R = 3$.

Table 4.10 Input parameters and simulated specifications during emptying phase*

Number of Equilibirum Stages	Optimum Reflux Ratio	Corrected (operative) Reflux Ratio	Pressure (bara)	Bottom to Feed Ratio	Recovery (R_{C4F10})	Purity (P_{C4F10})
5	3	4	2.5	0.24	99.98%	99.58%

Table 4.11 Input parameters and simulated specifications during filling phase*

Number of Equilibirum Stages	Optimum Reflux Ratio	Corrected (operative) Reflux Ratio	Pressure (bara)	Bottom to Feed Ratio	Recovery (R_{C4F10})	Purity (P_{C4F10})
5	3	4	2.45	0.24	99.78%	99.75%

4.5.4 Sizing and Optimization of the Column

While the reasons behind the optimal selection of free parameters has been extensively discussed, the core of the simulation has been delved not yet. In fact, the productivity (expressed as the feed flow rate to be treated) and any operational constraints have not yet been specified. In this section, we will perform the sizing and optimization of the column with reference to the filling phase. The steps taken for the emptying phase are the same. First, let's outline the conditions of the incoming feed (Table 4.12).

Table 4.12 Feed conditions

Volumetric Flowrate (l/h)	Molar Flowrate (mol/h)	Molar fraction of decafluorobutane	Temperature (°C)	Pressure (bara)
464.6	50	0.76	25	2.5

After defining the inlet conditions (Table 4.12) and saturating all degrees of freedom (Table 4.11), it is necessary, before starting the simulation, to define: (1) the type of condenser, (2) the hydraulic and pressure drop profile inside the column, and (3) the feeding stage. Regarding the type of condenser, we opt for a partial condenser since there is no need to completely condense the overhead vapor. This

choice also results in a reduction of the thermal load removed by the refrigerant fluid. The hydraulic and pressure drop profile is initially assumed vary constantly, with a pressure drop of 50 mbar between the injection point and the pressure at the column's top. Finally, the feeding stage affects the separation performance, so a sensitivity analysis is necessary to select the best feeding point. The sensitivity analysis on the feed point is reported in the table below (Table 4.13). Note that the optimal choice is to feed the feed exactly in the middle of the column, i.e., at the third equilibrium stage.

Table 4.13 Influence of the feeding point on purity and recovery

Feeding Stage	Purity	Recovery
2	0.99804	0.99671
3	0.99884	0.99751
4	0.99765	0.99632

In this case the, assuming the column is adiabatic, the duties of the reboiler and of the condeser are respectively 60.02 W and -297.02 W. Moreover, the thermal, pressure and composition profiles along the column are reported here below in Figures 4.27 and 4.28.

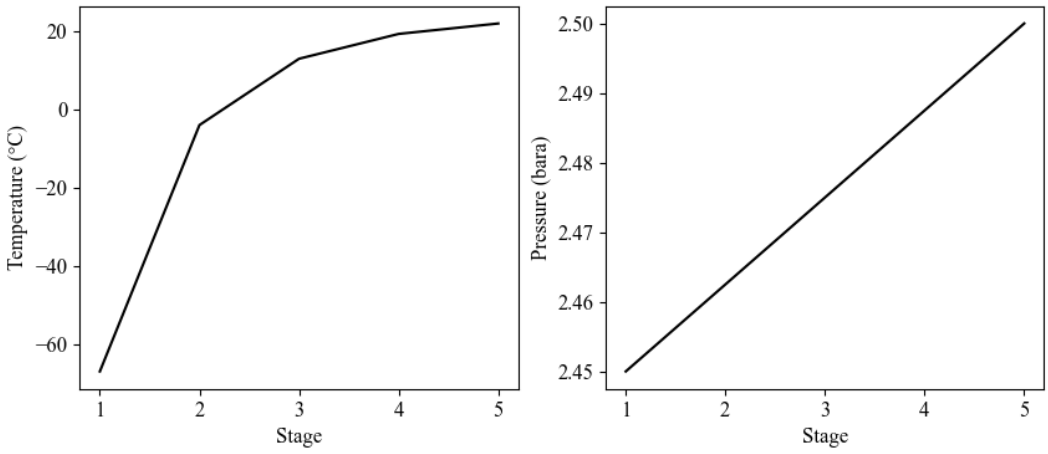

Fig. 4.27 Temperature (left-side) and Pressure (right-side) profiles along the column.

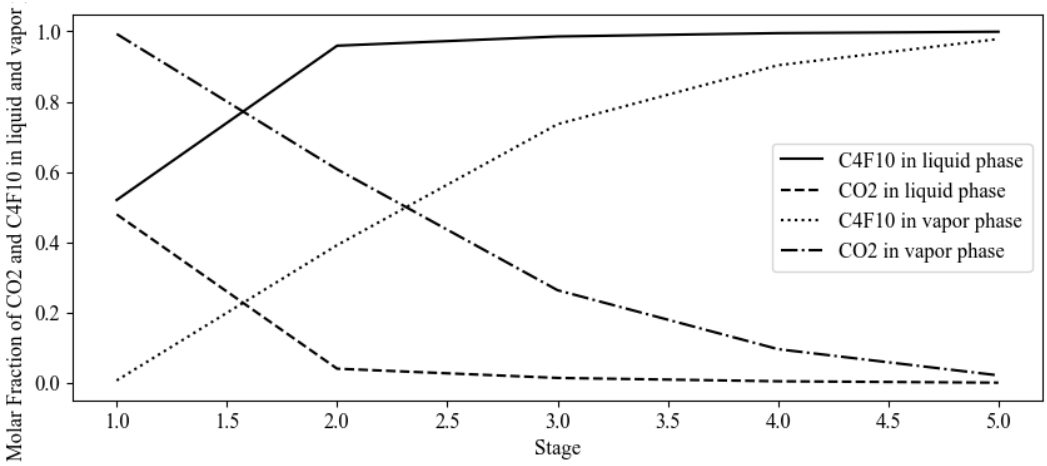

Fig. 4.28 Molar composition of the liquid and vapor phases along the column.

As can be seen from Figure 4.27, the partial condensation temperature of the mixture is very low, specifically -66.84 °C. This extremely cold condition imposes a strong operational constraint, not only in the choice of the refrigerant but also from a thermodynamic perspective. In fact, carbon dioxide exhibits a peculiar behavior around this temperature, undergoing a solid-vapor transition. The possibility of solidification represents a significant risk to the effectiveness of the separation process. The formation of solid CO_2 could lead to a partial reduction in the heat exchange area in the condenser and, in the worst case, complete clog of fluid flow.

This behavior requires maintaining a condenser temperature higher than the solid-vapor transition temperature of pure CO_2 at the pressure equal to the one of the column's head. By fitting experimental data [16], it is possible to determine the solidification temperature. Figure 4.29 shows the variation of the solid-vapor transition pressure and the squared error between the experimental data and the regression results. Further information on the regression can be found in Appendix C. This analysis reveals that at a pressure of 2.45 bar (the head pressure of the column), the solid-vapor transition temperature is -66.61 °C.

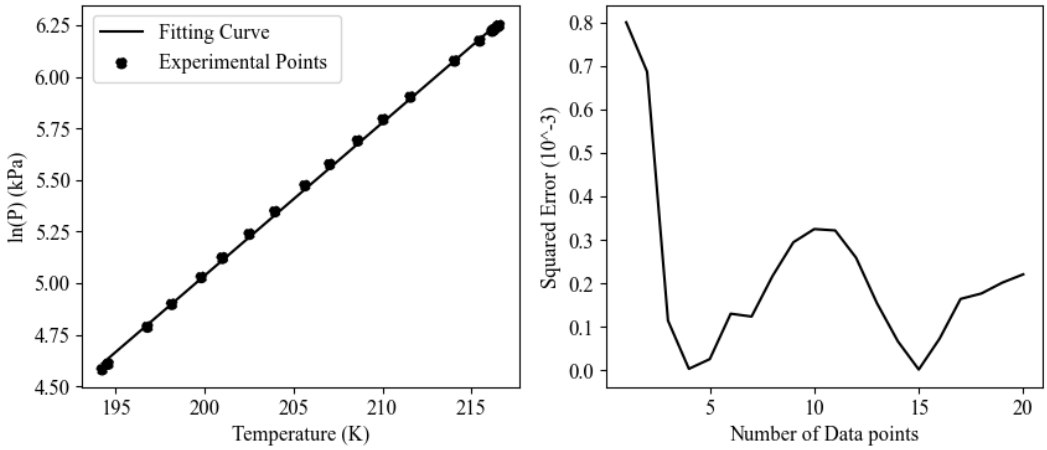

Fig. 4.29 Solidification Pressure of pure CO_2 as a function of temperature, data fitted Fernandez-Fassnacht E. ([16]) (let-side) and squared error of the regression (right-side).

The solidification temperature is slightly lower than the partial condensation temperature calculated by Aspen Plus. The reason for this discrepancy is that the simulator was not set up to account for the formation of solids. Therefore, in order to simplify the modeling and minimize computational costs, a constraint was imposed on the temperature of the first stage (partial condenser) instead of using a thermodynamic model that accounts for solid-vapor equilibrium. Specifically, the duty of the condenser was fixed in place of the reflux ratio. The choice of duty as a free parameter affects the simulation results. In Figure 4.30, it is evident that a lower heat removal leads to reduced performance and, naturally, a decrease in both the reflux ratio and the head temperature of the column. Fortunately, due to the small variation required, purity and recovery are not significantly affected by this modification. In summary, the fixed free parameters are as follows: (1) Head pressure at 2.45 bar; (2) Number of theoretical stages set at 5; (3) Feed at the fourth theoretical stage; (4) B/F ratio set to 0.75; and (5) Partial condenser duty fixed at -288.7 W (corresponding to a 2.8% reduction with respect to the one resulting from previous runs and a condenser temperature of -60°C).

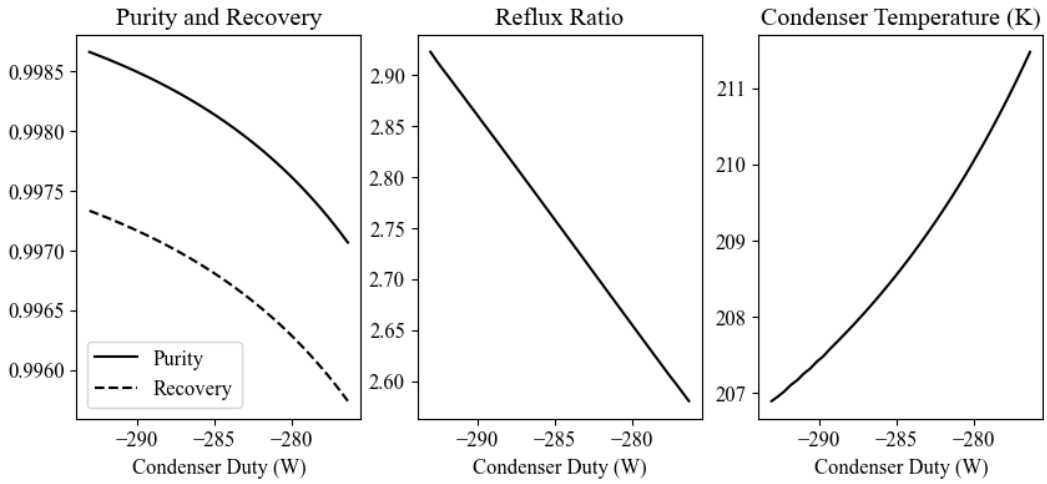

Fig. 4.30 Effect of variation of condenser duty on Purity and Recovery (left-side chart), Reflux Ratio (center chart) and Condenser Temperature (right-side chart)

The first consideration for sizing equipment is the choice of column. As discussed in Section 4.5.1, the distillation process is typically carried out in tray columns. In this application, we are dealing with a system of small dimensions, so the nominal diameter of the column is on the order of centimeters. Consequently, it was decided to proceed with the design of a packed column. The following steps are made:

1. Choose a diameter and determine the specific vapor and liquid flow rates, stage by stage.
2. Choose a type of packing and analyze the hydraulic and thermal profiles of the column.
3. Calculate pressure drops, verify the efficiency of the packing at the given hydraulic condition, and determine the column's height.

The diameter of the column (D_c) is fixed at 3 centimeters, and the specific volumetric flow rates of the liquid phase (V_s^l), vapor phase (V_s^v), and the F-factor (packing characteristic factor) are determined using the following relationships (Equations 4.12, 4.13, and 4.14):

$$A_c = \frac{\pi}{4} D_c^2 \tag{4.12}$$

$$V_s^l = \frac{V^l}{A_c} \; and \; V_s^v = \frac{V^v}{A_c} \tag{4.13}$$

$$F_{factor} = V_s^v \sqrt{\rho^v} \tag{4.14}$$

Where A_c and ρ^v represent the cross-sectional area of the column and the density of the vapor at temperature and pressure conditions within the column.

Next, an appropriate packing material is selected based on the described process conditions. The choice of packing material is one of the key steps in the project's realization. In general, the internal solid material aims to maximize the interface between the two counter-current fluid phases. This increases the surface area for mass and heat transfer, ensuring high performance. There are different types of packing materials, classified as structured and random packings [17], [18]. The main characteristics include the packing size (d_p), void volume fraction (V_{void}), and specific surface area (a_p), defined as the packing surface area per cubic meter of the column. Typically, for a given type of packing, decreasing its size leads to an increase in specific surface area and a decrease in void fraction. Additionally, under constant fluid dynamic conditions (constant values of F-factor and liquid flow rate), increasing specific surface area is observed to enhance performance while reducing void fraction increases pressure losses. Therefore, the choice must strike a balance between efficiency and pressure losses.

Taking these considerations into account, the choice was made to use laboratory structured packings DX^{TM} (figure 4.31) by *Sulzer Chemtech AG*, whose features and characteristic curves are respectively presented in Table 4.14 and Figures 4.32 and 4.33. Several issues with the supplier have been met during this choice. This lead to the impossibility of starting to build the distillation column's system.

Fig. 4.31 Picture of the DX_{TM} structured packing as reported by *Sulzer Chemtech AG* [21].

Table 4.14 Features of the DX^{TM} structured packing [23].

Diameter Range, D_c, (mm)	Specific Surface Area, a_p, (m^2/m^3)	Void Fraction, V_{void}, (%)
30-125	900	93.3

Figure 4.32 shows the HETP/m versus the F-factor. This chart can be considered one of the most important design specifications. As a fact, the number of theoretical stages (N) and the value of HETP/m are used to determine the height of the packing bed (Z). To do so, one has to:

- Choose a starting (reasonable value) of pressure drop.
- Evaluate the F-factor at each theoretical stage.
- Find the corresponding value of HETP from Figure 4.32.
- Calculate the total height of the packing as the sum of the HETP using Equation 4.15.

$$Z = \Sigma_i \, (HETP)_i \tag{4.15}$$

Then, using Figure 4.33 and the same values of the F-factor, one has to calculate, in the same fashion, the pressure drops per meter at each stage. Finally, it is possible to compute the total pressure drop (ΔP) as the sum of the pressure drops per meter ($\Delta P/Z$) times the total height of the packing bed (Z) (Eq. 4.16).

$$\Delta P = Z \, \Sigma_i \, (\Delta P/Z)_i \tag{4.16}$$

Where i goes from 1 to N.

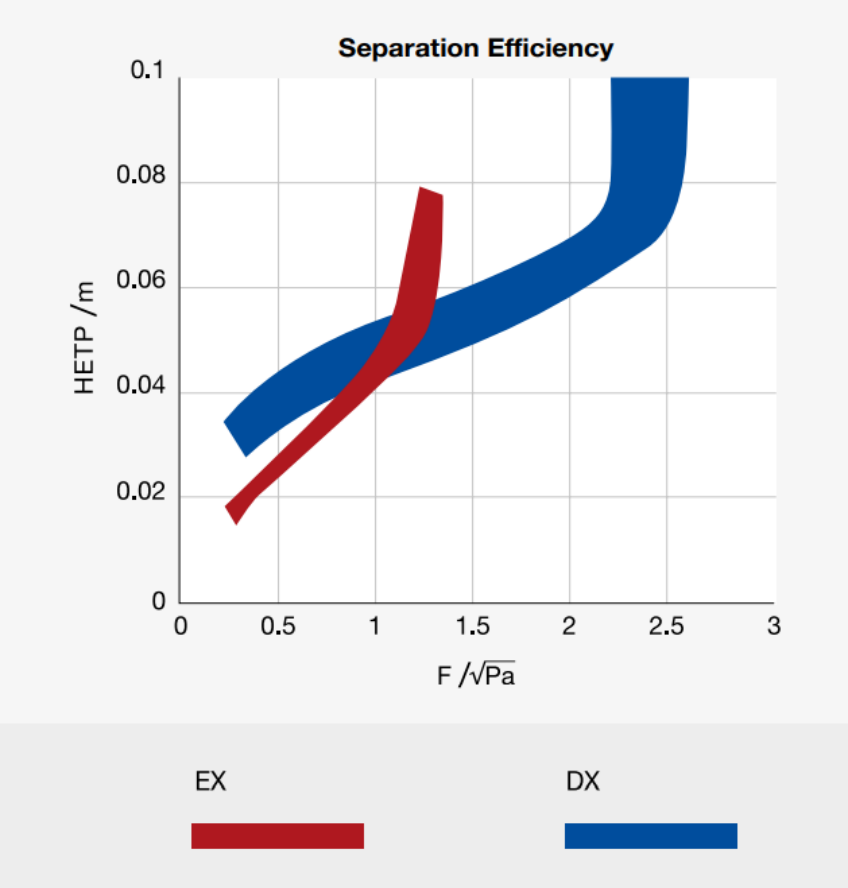

Fig. 4.32 Normalized Height Equivalent to Theoretical Plate (HETP) as a function of normalized F-factor as reported by *Sulzer Chemtech AG* [21].

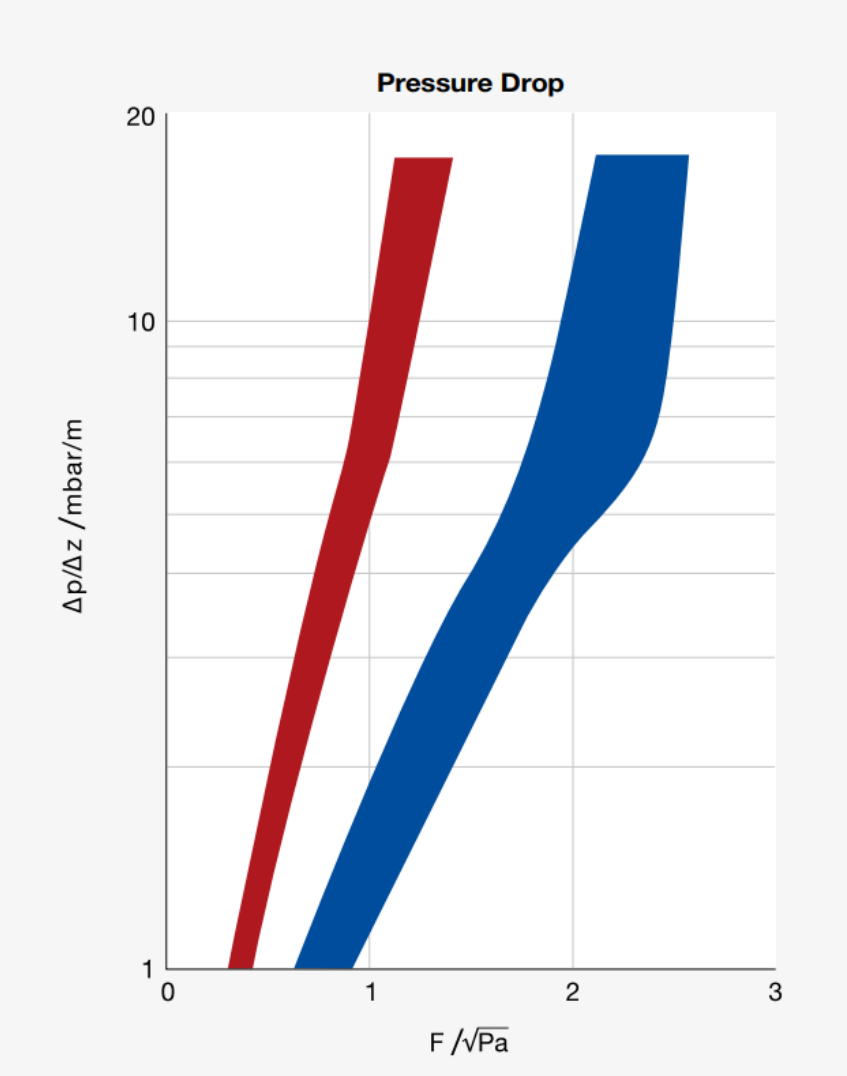

Fig. 4.33 Normalized Pressure drops per meter of column, $\Delta P/Z$, as a function of normalized F-factor as reported by *Sulzer Chemtech AG* [21].

This process must be done in an iterative mode since the F-factor is a function of gas velocity and gas density, which, in turn, depend on pressure. Luckily, the Aspen Plus simulator is able to iterate this process just by selecting the update pressure drops option (setting the head pressure at 2.45 bara).So, the features of the chosen packing material (Table 4.14) are entered, and an average value of the F-factor is calculated. Then, a value of HETP is selected from the blue region in Figure 4.32 (in this case, the lower limit of the blue band is chosen, which represents the worst-case scenario). Specifically, the chosen average value of the F-factor is 0.82, which corresponds to an HETP of approximately 0.05-0.06 m^{-1}. With this information, the

final simulation is initiated, and the results are obtained, as shown in Tables 4.15, 4.16, and 4.17.

Table 4.15 Molar liquid fraction and vapor fraction along the column.

Stage (N)	Molar fraction of CO_2 in the vapor phase	Molar fraction of C_4F_{10} in the vapor phase	Molar fraction of CO_2 in the liquid phase	Molar fraction of C_4F_{10} in the liquid phase
1	0.981	0.019	0.287	0.713
2	0.484	0.516	0.073	0.927
3	0.300	0.700	0.025	0.975
4	0.224	0.756	0.015	0.985
5	0.092	0.908	0.005	0.995

Table 4.16 Thermal profile (C), pressure profile ($mbara$), specific flows ($m^3/h/m^2$) and F-factor ($(m/s)Pa^{0.5}$).

Stage (N)	Stage temperature (°C)	Stage pressure ($mbar$)	Specific liquid flowrate ($m^3/h/m^2$)	Specific vapor flowrate ($m^3/h/m^2$)	F-factor ($(m/s)Pa^{0.5}$)
1	-57.51	2450	4.78	573.96	0.63
2	-10.25	2462.5	7.50	658.27	0.81
3	8.34	2462.6	9.06	725.95	0.91
4	13.05	2462.8	9.20	738.56	0.94
5	19.19	2463	8.28	0.00	0.00

Finally, it is specified that the HETP value calculated by the simulator is around 0.07 m^{-1} per stage, a value close to what is shown in Figure 4.32. Therefore, the theoretical total height of the packing (Z) is found to be 0.21 m. To estimate the total column height, the following considerations need to be made, as per [19]:

- Increase the theoretical height found to account for simulation errors and to ensure a safety factor. In this case, it was decided to double it, resulting in a packing height of 0.4 m.
- Increase the height further to ensure proper distribution of descending liquid and ascending gas. Typically, 1-2 meters are recommended for columns with overall heights in the order of tens of meters. Therefore, an additional increase

Table 4.17 Condenser and reboiler duties, purity and recovery of the rate based simulation with Sulzer Chemtech AG's DX^{TM} structured packing [23].

Condenser Duty (W)	Reboiler Duty (W)	Purity% (P_{C4F10})	Recovery% (R_{C4F10})
288.70	45.72	99.50	99.38

of 25% seems consistent with the guidelines. At this point, the packing height is 0.5 m.

- Allow extra space for the liquid distributor, support for the packing, and potential redistribution cones. In this case, an additional 0.1 meters of column height is estimated.
- The height related to the hold-up of liquid at the bottom of the column is calculated by setting a residence time and multiplying it by the liquid flow rate at the fourth stage. This yields a liquid volume, which, when divided by the column's cross-section, results in a height of 0.28 m.
- Finally, assume 0.3 meters above the packing for liquid inlet and the disengagement of any entrained liquid particles, and an equal amount below the packing to ensure the uniformity of vapor flow from the reboiler.

To summarize, there are 0.6 meters for the packing zone and an additional 0.9 meters for the free zone, for a total height (neglecting the head and dished bottoms) of 1.5 meters.

4.5.5 Reboiler and Condenser's Sizing

Once the column has been fully sized, the sizing procedure for the heating and cooling devices is carried out. We begin with the condenser, where the inlet stream consists of vapor from the second stage, and the outlet streams are the distillate and the reflux. The conditions of temperature, composition, and flow rate are presented in Table 4.18. A simplified schematic is shown in Figure 4.34.

Table 4.18 Condenser's input and output streams conditions.

Stream ID	Molar Flowrate (mol/h)	CO_2 mole fraction (mol/mol)	C_4F_{10} mole fraction (mol/mol)	Temperature (°C)
V_2	62.29	0.483	0.517	-10.25
D	17.47	0.987	0.0183	-57.60
R	44.82	0.289	0.711	-57.60

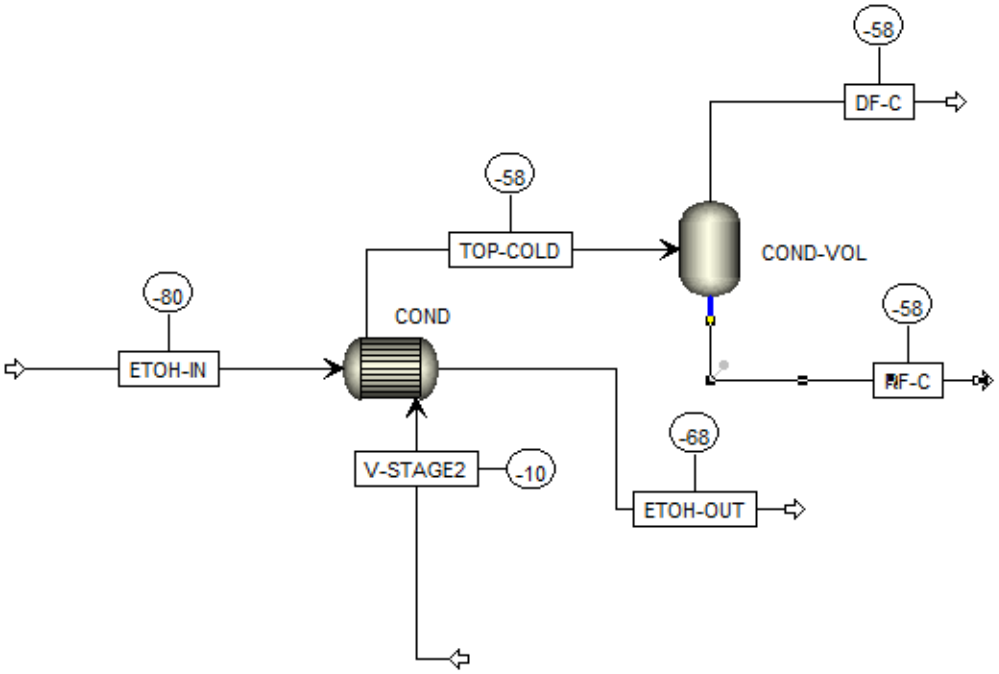

Fig. 4.34 Heax exchanger and reflux drum forming the condeser stage.

Now, with the given inlet conditions and outlet specifications, a shortcut simulation begins with the following specifications:

- The refrigerant fluid used is ethanol at -80°C and 1 bar.
- The pinch temperature, being a gas-liquid exchange, is set to be at least 20°C, and the overall heat transfer coefficient (U) is set to 340 (W/m^2K), following tables of organic vapor condensing by organic liquid in a counter-current heat exchange [19].

- The goal is to achieve the specified thermal conditions of the distillate and reflux streams as listed in Table 4.18.

From this shortcut simulation, it is determined that the required heat exchange area is 0.02 m^2 when the refrigerant flow rate is 0.7 $kmol/h$. It reality, the selected heat exchanger was significantly oversized to accommodate non idealities and future possible expansions, and the final sizing was handled directly by the manufacturer [20].

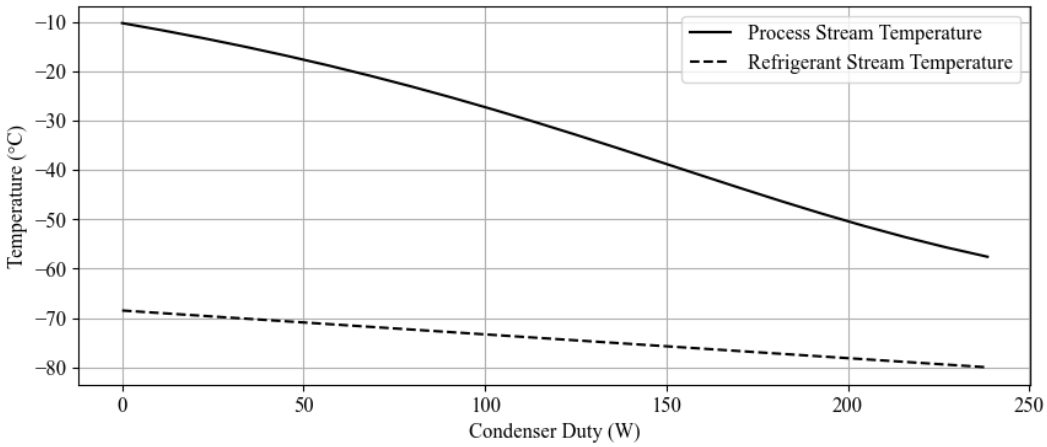

Fig. 4.35 Process stream and refrigerant stream temperature versus of heat exchanged.

Finally, with the known reflux flow rate and assuming a liquid residence time of 15 minutes (τ_{RD}) in the reflux drum, it is possible to calculate the volume occupied by the liquid under nominal conditions. Assuming that the liquid volume occupies, at nominal conditions, approximately 30% of the total available volume, the reflux drum is sized using Equations 4.17 and 4.18 (neglecting the volume of the bottom) and setting the internal diameter of the reflux drum equal to the nominal closure flange diameter.

$$V_{reflux} = R\ \tau_{RD} \tag{4.17}$$

$$V_{reflux} = 0.3\ V_{RD} = \frac{\pi\ D_{RD}^2\ H_{RD}}{4} \tag{4.18}$$

Where V_{reflux} is the volume of the reflux drum occupied by liquid at a given residence time (τ_{RD}), while H_{RD} and D_{RD} are the height and the internal diameter of the reflux

drum. Finally, V_{RD} is the volume of the reflux drum reported in Figures 4.36 and 4.37.

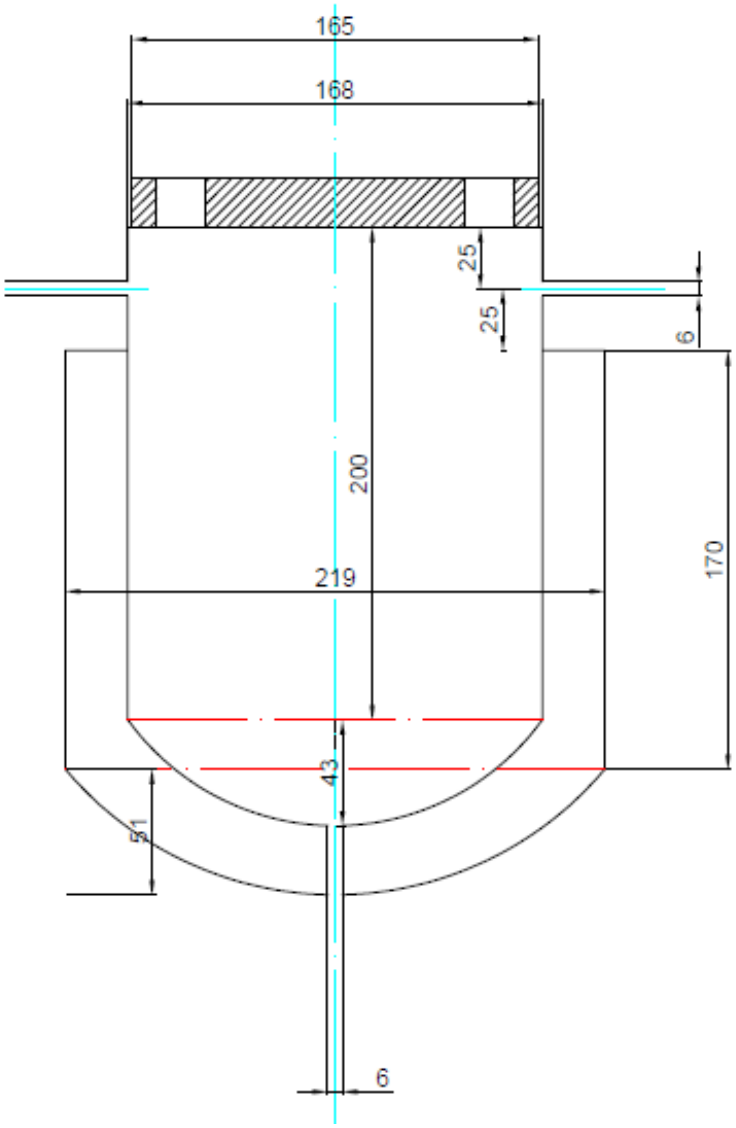

Fig. 4.36 Technical drawing of the Reflux Drum with D_{RD}, H_{RD} and V_{RD} respectively equal to 168 mm, 200 mm and 4.43 liters.

Figures 4.37 and 4.38 show actual pictures of the apparatuses. Both from the technical drawing and from the actual picture it is possible to notice that a cooling jacket has been provided to the reflux drum in case the heat transfer in the CB30 heat exchanger would not be sufficient.

Fig. 4.37 Picture of the Reflux Drum.

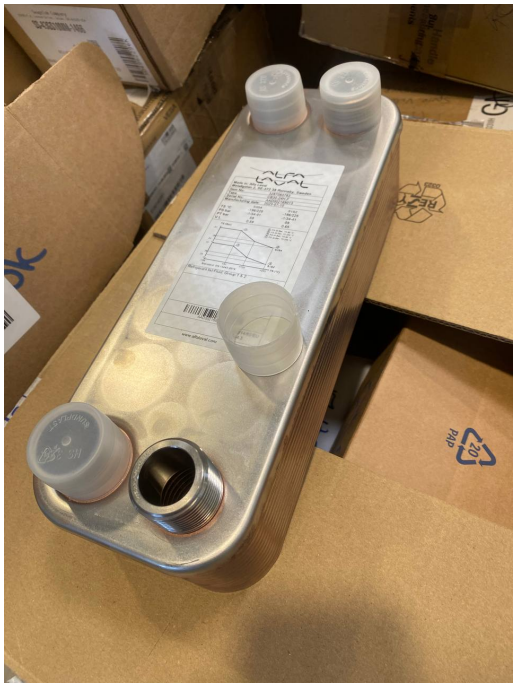

Fig. 4.38 Picture of the CB30 HeatEX.

The sizing of the reboiler unit follows a similar procedure; for this reason, the steps will not be described. The only difference is that, due to the lower heat demand and a vaporization temperature close to 20°C, it was decided to simply insert an electrically heated jacket. Figures 4.39 and 4.40 show a real picture and the technical scheme of the reboiler drum.

Fig. 4.39 Picture of the Reboiler Drum.

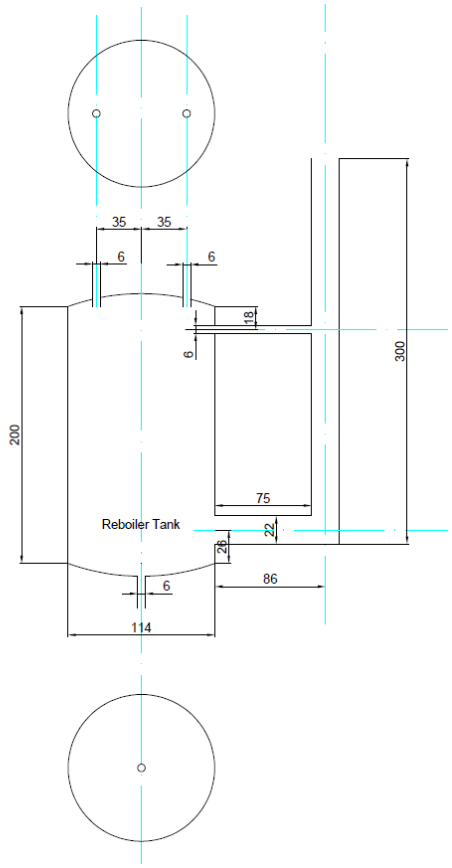

Fig. 4.40 Technical drawing of the Reboiler Drum

4.5.6 Control Logic and Dynamic Behavior of the Column

A control system plays a crucial role in maintaining process variables at their steady values. This is essential to ensure profitability, product quality, and the safety of the plant itself. It's clear that engineering an effective control system is key to the development of a process. In this section, we will describe the control logic chosen for the system in question, and, using Aspen Dynamics, we will show the effects that deviations in input variables, such as flow rate, temperature, and feed composition, have on the output variables, such as distillate and bottom product purity.

Among various control loops, the most common is the so-called "closed-loop feedback control" (FBC). A feedback control aims to maintain an output process variable (PV) at the defined set point (SP) through the following mechanism: (1) Measures the output variable in response to a disturbance; (2) Compares this variable

with the set point, deriving the error (ERR); (3) Sends a signal to the control system and the actuator (usually expressed as OP since it modifies the opening position of a valve), which adjusts the input variable to minimize the error. The error is defined as:

$$ERR(t) = SP(t) \; +- \; PV(t) \tag{4.19}$$

Where a positive sign indicates a negative gain (K_c), meaning direct acting (in other words, if the PV exceeds the SP, OP should increase), while the negative sign refers to a positive gain, i.e., reverse acting (that is, if the PV exceeds the SP, then OP should decrease) [22].

Therefore, the purpose of a control system is to minimize the error (Eq. 4.19) by bringing the process variable back to the set point. When choosing a control system, one must consider the balance between performance (response speed) and robustness (the ability to return the system to the set point stably). In other words, it is necessary to ensure a stable response where the process variable converges in an oscillatory motion towards its set point. In practice, the higher the gain, the faster the response. But it cannot be increased indefinitely, as it would lead to an unstable response regime in which the response is divergent oscillatory [31].

In general, robustness and performance depend on the choice of the controller and tuning parameters. There are four types of feedback controllers:

1. *On/Off Controller*: Used to manipulate variables that oscillate between two states. In this case, the logic is defined by the following structure: OP = 0% if PV < SP, else OP = 100% (in reverse action, the signs are the opposite).

2. *Proportional Controller (P)*: Generates an output proportional to the deviation of the control variable. The logic is as follows:

$$OP = OP_{ss} + K_c \; ERR \tag{4.20}$$

   The value of the bias, OP_{ss}, equals OP when PV equals SP. The resposnse of a P-only controller is the fastest one, but, unfortunately, an offset always shows up and it can be removed only if the gain tends to infinity. As we know robustness must be guaranteed, hence K_c has to be set below the value that brings the system to an unstable response. Usually, used for level control since an offset is a negligible problem.

3. *Proportional-Integral Controller (PI)*: a PI controller is able to damp out the oscillations and return to the set point. The integral term eliminates the offset but slows down the damping process. The integral time, τ_I, is the characteristic time required for the controller's output to move by an amount equivalent to the error. The lower the τ_I the slower the damping process, so it must be correctly tuned. The logic is defined by the following equation:

$$OP = K_c(ERR + \frac{\int ERR}{\tau_I}) \tag{4.21}$$

   PI controllers are used for most of the controls within a plant.

4. *Proportional-Integral-Derivative Controller (PID)*: When the response of a PI controller is not sufficiently fast, the addition of a derivative term promotes the acceleration of damping oscillations. By measuring the rate of change of the error, it is possible to understand the error's direction and, therefore, to act more quickly. The derivative time, τ_D, is the characteristic time required for the proportional action to reach the derivative action. The logic is defined by the following equation:

$$OP = K_c(ERR + \frac{\int ERR}{\tau_I} + \tau_D \frac{d(ERR)}{dt}) \tag{4.22}$$

   The derivative action is typically used for temperature and composition control, where a faster response is required.

In general, the guidelines for choosing the type of controller follow Figure 4.41.

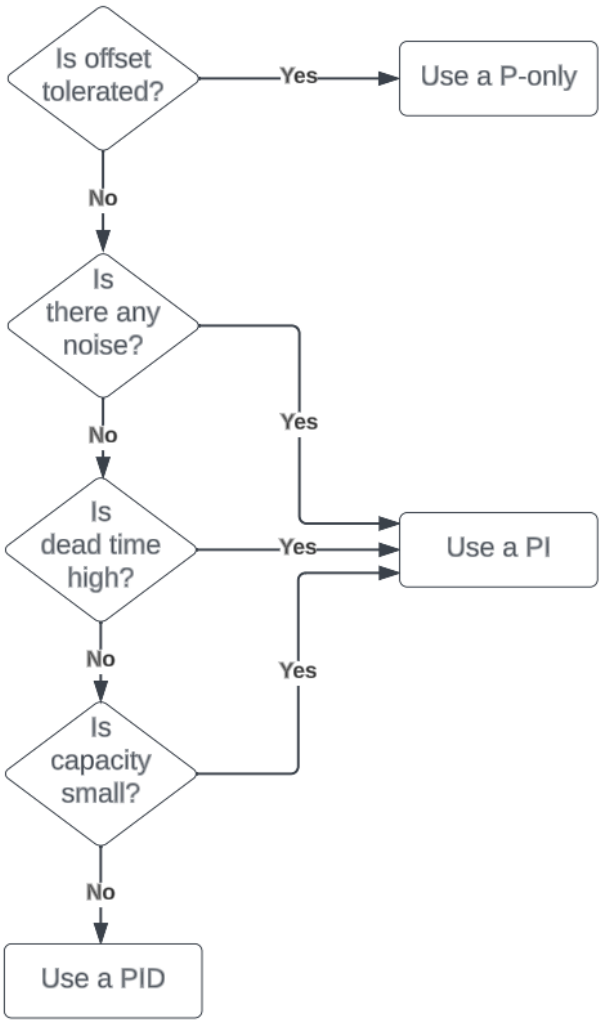

Fig. 4.41 Flowchart for controller selection [22].

After this brief introduction, it is needed to: (1) Choose controlled and manipulating variables; (2) Select the controller type and parameter tuning; (3) Test the system's response to any disturbances or set point variations.

Ideally, an effective control system aims to ensure that the compositions of the streams leaving the column are constant and equal to the steady-state values. In practice, continuous composition control presents two major issues: the extremely high cost of sensors and the difficult management due to the intrinsic delay caused by the long characteristic times of such sensors. Therefore, it is opted for a system capable of maintaining thermodynamic conditions constant and a thermal profile as

close to steady-state as possible. In the case under consideration (Fig. 4.42), it was decided to control the following variables:

1. The feed flow (W1) is measured and regulated using a mass flow meter (XMFC-10160).
2. The liquid level in the reflux drum is measured by a level sensor (LSH-10291) and kept constant by controlling the reflux flow rate in the column through a valve (YV-10220).
3. The head pressure is measured by a sensor (PT-10276) and controlled by adjusting the opening of a valve on the distillate line (PCV-10242).
4. The column temperature is monitored by a series of temperature sensors (TE-10280, TE-10284, TE-10286, TE-10288) along the height of the column, and the thermal profile is kept constant by varying the thermal power supplied to the reboiler (Heating Bands).
5. The liquid level in the reboiler drum is measured (LSH-10290) and kept constant by regulating the flow extracted from the bottom with the help of a mass flow meter (XMFC-10260).

It was decided, initially, not to regulate the amount of heat removed at the condenser. At the time of writing this text, the refrigeration unit has not yet been delivered by the supplier. For this reason, the possibility of modifying the control structure in the future is reserved.

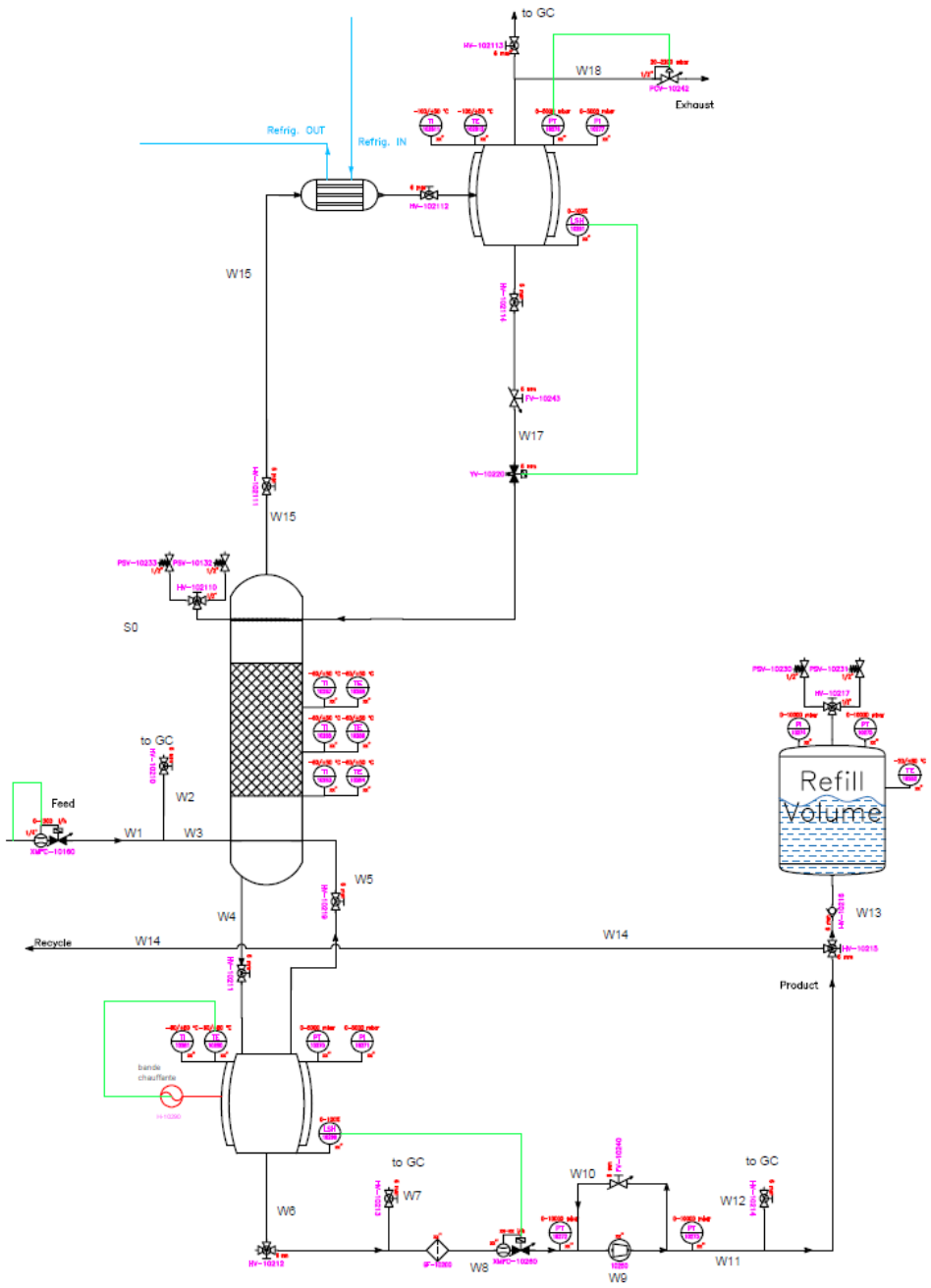

Fig. 4.42 P&ID of the distillation column section.

Once the control logic is established, the selection of individual controllers and tuning parameters is carried out. This was done using Aspen Dynamics software, which allows for creating transient simulations, tuning different control structures, and, most importantly, verifying the system's ability to respond to external distur-

bances. It was possible to determine an initial logic. Specifically, the parameters of the previously mentioned controllers are listed in Table 4.19. The choice of parameters was made using the ATV tuning setting [22] or by manually increasing the gain until the instability limit was reached.

Table 4.19 Controllers Structure and Tuning Parameters (Integral time expressed in minutes and Gain as a percentage).

Parameter	Condenser Drum Level (LCC)	Reboiler Drum Level (LCR)	Pilot Stage Temperature (TC)	Feed Flowrate (FC)	Condenser Drum Pressure (PC)
K_c	2	2	3.2	0.5	20
τ_I	10	10	5.3	0.3	12

In order to verify the selected controllers, a series of dynamic simulations were conducted in response to external disturbances. Specifically, the following were simulated:

1. An increase in the temperature of the incoming mixture (from 25 to 35°C).
2. Two variations in the composition of the feed. In the first case, a mixture poorer in C_4F_{10} was assumed compared to nominal conditions (molar fraction from 0.769 to 0.6). In the second case, a richer mixture was assumed (molar fraction from 0.769 to 0.9).
3. A variation in the molar flow rate at the inlet from 50 to 60 mol/h (in this case, instead of assuming an external disturbance, the set point value is varied).

First, let's analyze the effect of an increase in the enthalpy of the incoming mixture. The disturbance is introduced into the system in the fourth hour of the simulation. In Figure 4.43, it is observed that an increase in the feed temperature results in an increase in pressure and temperature on the pilot tray (the pilot tray corresponds to the second theoretical stage, as the thermal jump between the first and second stages is the largest). The controllers respond by opening the valve on the distillate line and reducing the thermal power supplied to the reboiler. The system quickly and stably returns to a new steady state.

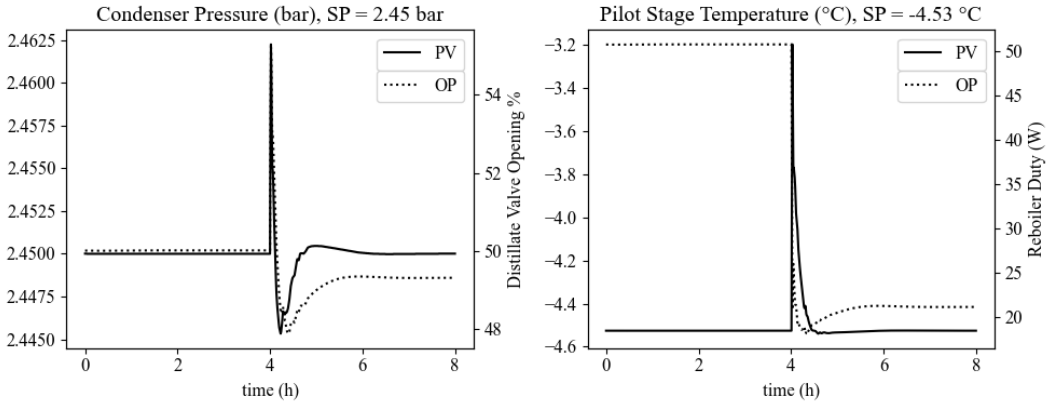

Fig. 4.43 Increasing feed temperature: Condenser pressure (PV) and PCV-10242 valve opening (OP), left-side chart, and pilot stage temperature (PV) and reboiler duty (OP), right-side chart, as a function of time.

In Figure 4.44, it is possible to observe that the variations in the level inside both the reboiler drum and the condenser drum are very small. In any case, the system's response is stable.

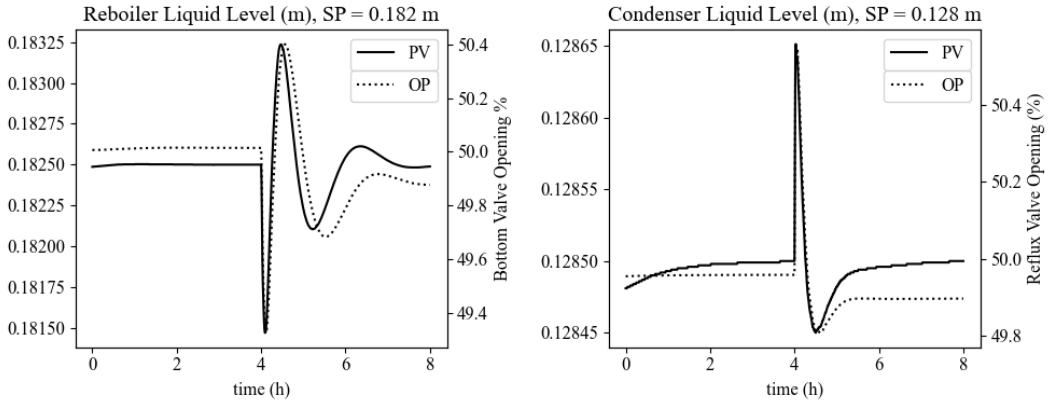

Fig. 4.44 Increasing feed temperature: reboiler drum level (PV) and XMFC-10260 valve opening (OP), left-side chart, and condenser drum level (PV) and YV-10220 opening (OP), right-side chart, as a function of time.

Figure 4.45, on the other hand, shows the key variables. It can be seen that the purity and the flow rates of distillate and bottom vary by only a few percentage points. The right-hand figure highlights a slight increase in the amount of decafluorobutane lost in the vapor phase. In other words, there is a small reduction in recovery. In general, it can be stated that the system performs well in response to a thermal disturbance at the inlet.

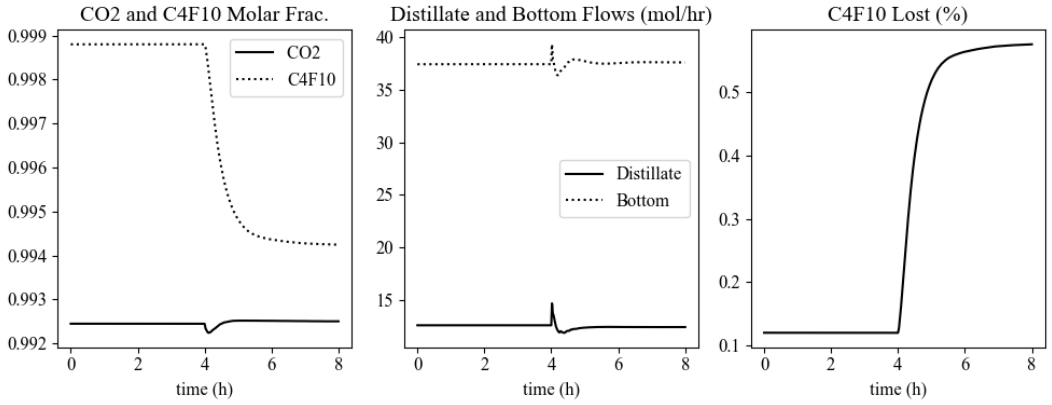

Fig. 4.45 Increasing feed temperature: CO_2 and C_4F_{10} molar fraction in the distillate and bottom streams (left-side chart), distillate and bottom flows (center chart) and C_4F_{10} lost in the distillate stream as a % of C_4F_{10} fed (right-side chart).

The second disturbance tested is a decrease in the molar fraction of C_4F_{10} in the feed stream. Figure 4.46 highlights a significant variation in the head pressure due to an increase in the average volatility of the mixture and a sudden reduction in the temperature of the pilot tray. In response to the external disturbance, the valve on the distillate line is opened, and an increase in thermal power supplied to the reboiler is observed (to bring the temperature back to its set point value). The system returns to a new steady state.

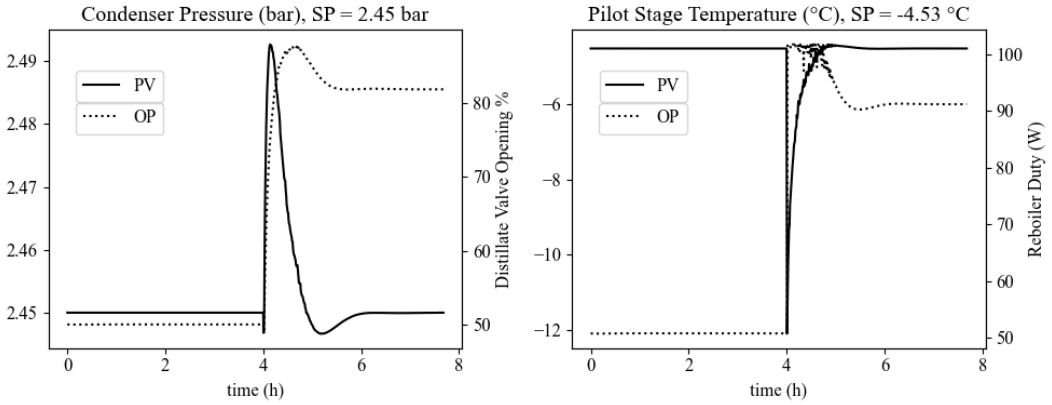

Fig. 4.46 Decreasing C_4F_{10} feed's molar fraction: Condenser pressure (PV) and PCV-10242 valve opening (OP), left-side chart, and pilot stage temperature (PV) and reboiler duty (OP), right-side chart, as a function of time.

In Figure 4.47, the variation in the level of the two drums is more pronounced in this case. Again, the response is stable and sufficiently fast.

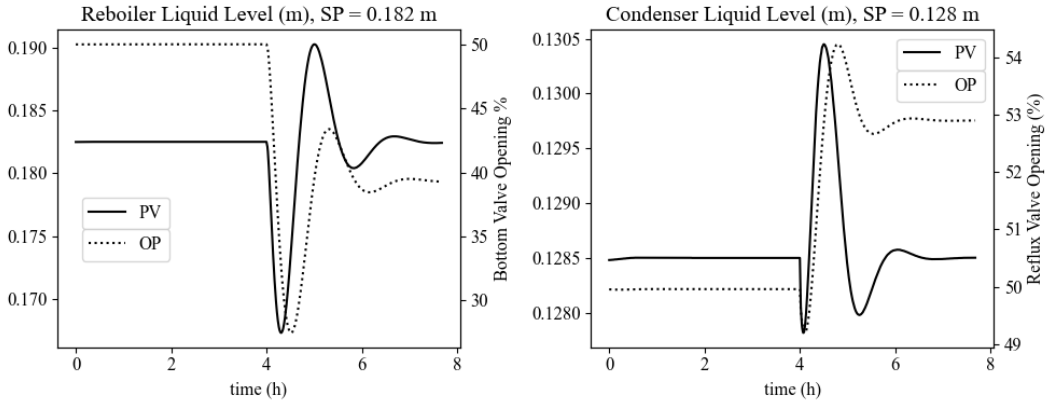

Fig. 4.47 Decreasing C_4F_{10} feed's molar fraction: reboiler drum level (PV) and XMFC-10260 valve opening (OP), left-side chart, and condenser drum level (PV) and YV-10220 opening (OP), right-side chart, as a function of time.

Figure 4.48 highlights how the product purity (bottom) is better than in the nominal case. Despite the increase in distillate flow, the effect of increased purity has a greater impact. This phenomenon is evident when observing the reduced quantity of C_4F_{10} lost. Summarizing, the system works well when the incoming mixture is enriched in carbon dioxide. This had already been highlighted in Section 4.5.3, where the performance of the system during the *filling* and *emptying* phases have been discussed.

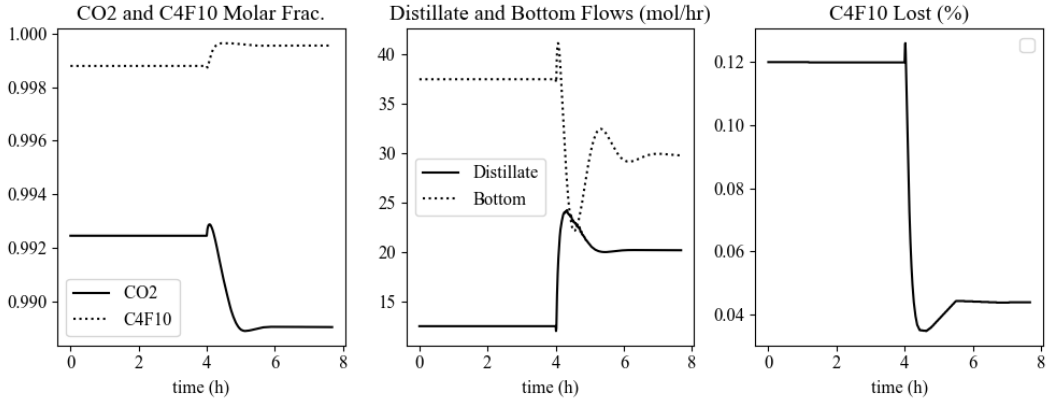

Fig. 4.48 Decreasing C_4F_{10} feed's molar fraction: CO_2 and C_4F_{10} molar fraction in the distillate and bottom streams (left-side chart), distillate and bottom flows (center chart) and C_4F_{10} lost in the distillate stream as a % of C_4F_{10} fed (right-side chart).

The third disturbance tested is an increase in the molar fraction of C_4F_{10} in the feed stream. Figures 4.49 and 4.50 show the behavior of the control devices

following the disturbances. In this case, a disturbance was introduced in the second hour, where the molar fraction of C_4F_{10} increased from 0.769 to 0.85, and a second disturbance in the fourth hour (from 0.85 to 0.90).

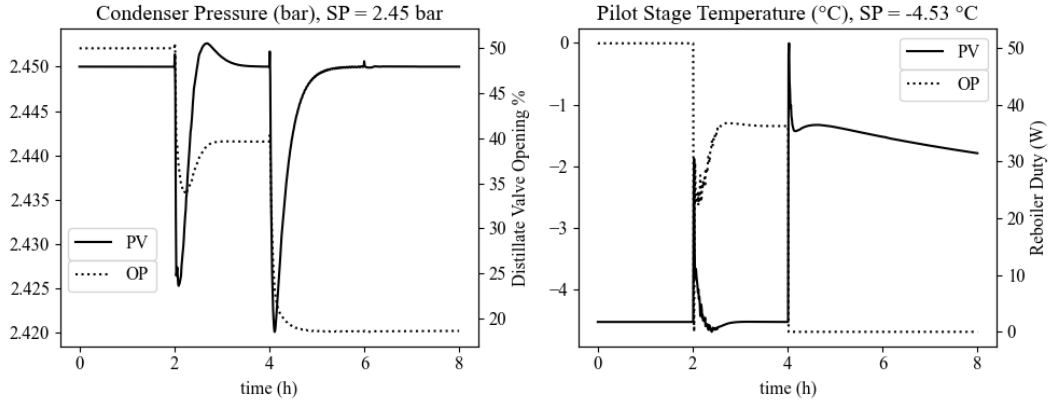

Fig. 4.49 Increasing C_4F_{10} feed's molar fraction: Condenser pressure (PV) and PCV-10242 valve opening (OP), left-side chart, and pilot stage temperature (PV) and reboiler duty (OP), right-side chart, as a function of time.

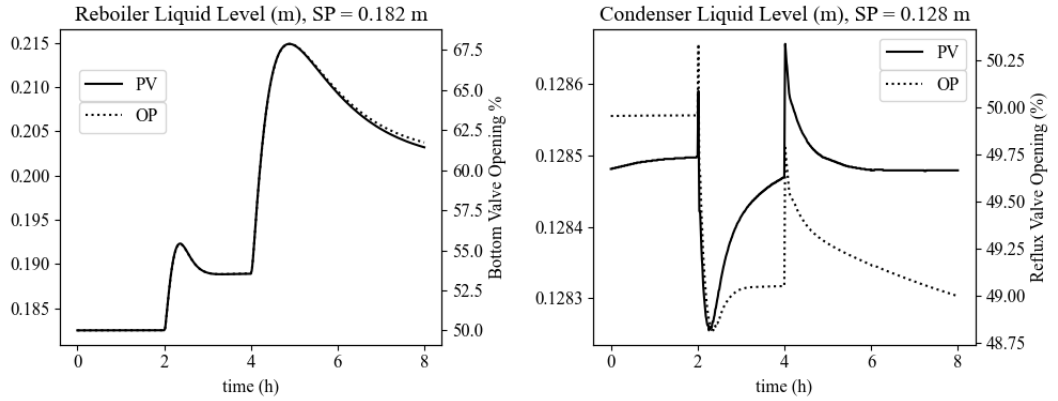

Fig. 4.50 Increasing C_4F_{10} feed's molar fraction: reboiler drum level (PV) and XMFC-10260 valve opening (OP), left-side chart, and condenser drum level (PV) and YV-10220 opening (OP), right-side chart, as a function of time.

Figure 4.51 highlights how the purity of the bottom product deteriorates. Fortunately, the reduction in distillate flow partially compensates for the increase in the amount of decafluorobutane lost. In fact, the system's behavior is diametrically opposed to that seen in the previous case.

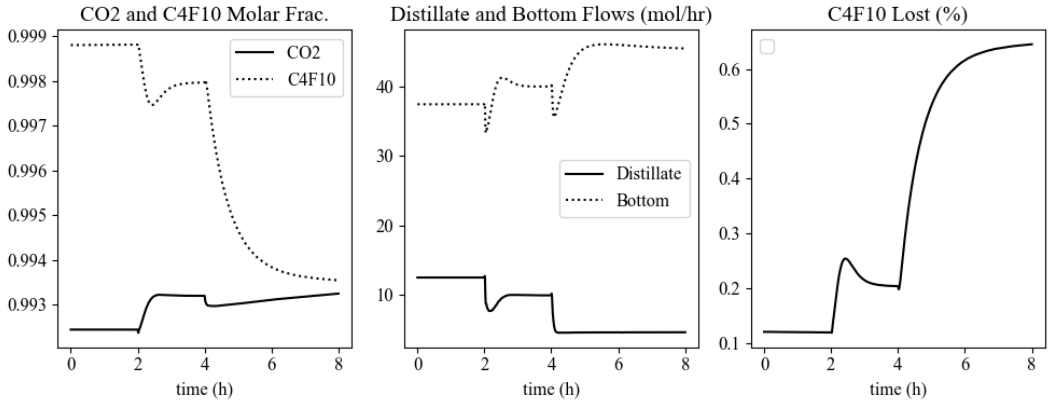

Fig. 4.51 Increasing C_4F_{10} feed's molar fraction: CO_2 and C_4F_{10} molar fraction in the distillate and bottom streams (left-side chart), distillate and bottom flows (center chart) and C_4F_{10} lost in the distillate stream as a % of C_4F_{10} fed (right-side chart).

Finally, one wonders what the system's response might be following a request for an increase in productivity. In other words, is desired to study the column's behavior following an increase in the feed rate. In this case as well, an increase in flow rate from 50 to 55 mol/h (third hour of simulation) and from 55 to 60 mol/h (seventh hour) is imposed. A greater quantity of fluid in the column results in a slight increase in pressure and a substantial increase in temperature. In practice, as it is not possible to control the heat removed by the condenser, the only way the system can reduce the column temperature is by reducing the thermal power generated by the reboiler (right-side chart of Fig. 4.52).

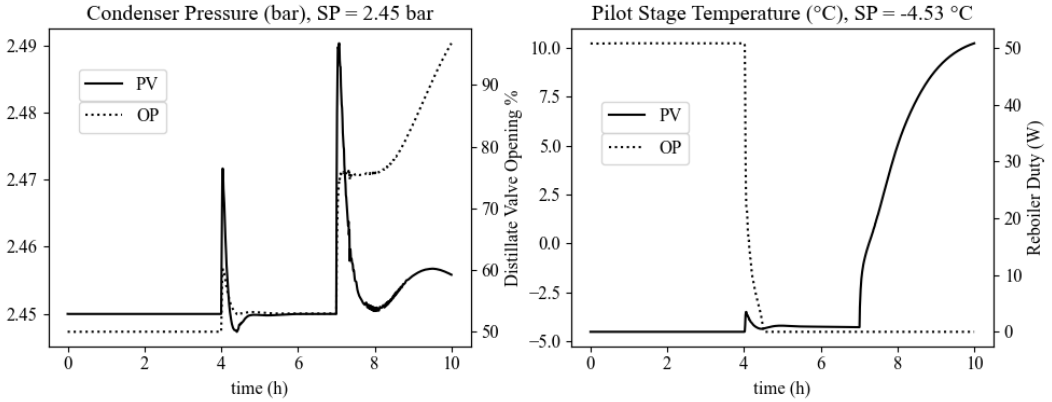

Fig. 4.52 Increasing feed's flow: Condenser pressure (PV) and PCV-10242 valve opening (OP), left-side chart, and pilot stage temperature (PV) and reboiler duty (OP), right-side chart, as a function of time.

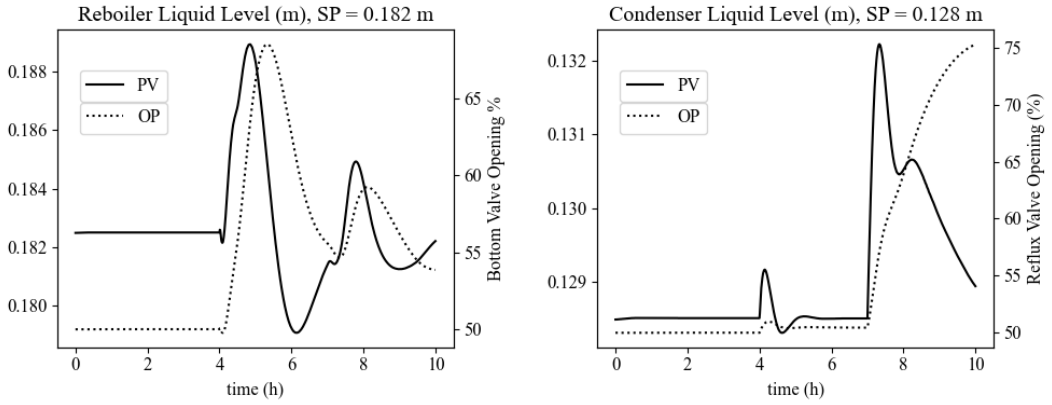

Fig. 4.53 Increasing Increasing feed's flow: reboiler drum level (PV) and XMFC-10260 valve opening (OP), left-side chart, and condenser drum level (PV) and YV-10220 opening (OP), right-side chart, as a function of time.

The system's inability to restore a thermal profile is the reason why it is not possible to establish a new steady state that allows the achievement of specifications close to nominal values. This phenomenon is very evident in Figure 4.55. It is clear that the thermal profile tends, over time, toward a flat line. With both thermal units (reboiler and condenser) inactive, the system reaches an equilibrium state where the column reaches the same temperature as the mixture being fed. In particular, the lower the thermal inertia of the system, the faster this flattening mechanism will be.

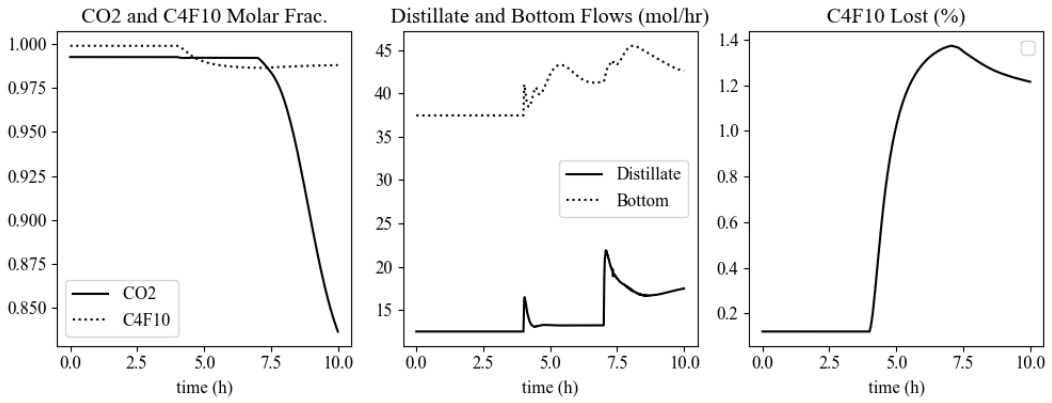

Fig. 4.54 Increasing feed's flow: CO_2 and C_4F_{10} molar fraction in the distillate and bottom streams (left-side chart), distillate and bottom flows (center chart) and C_4F_{10} lost in the distillate stream as a % of C_4F_{10} fed (right-side chart).

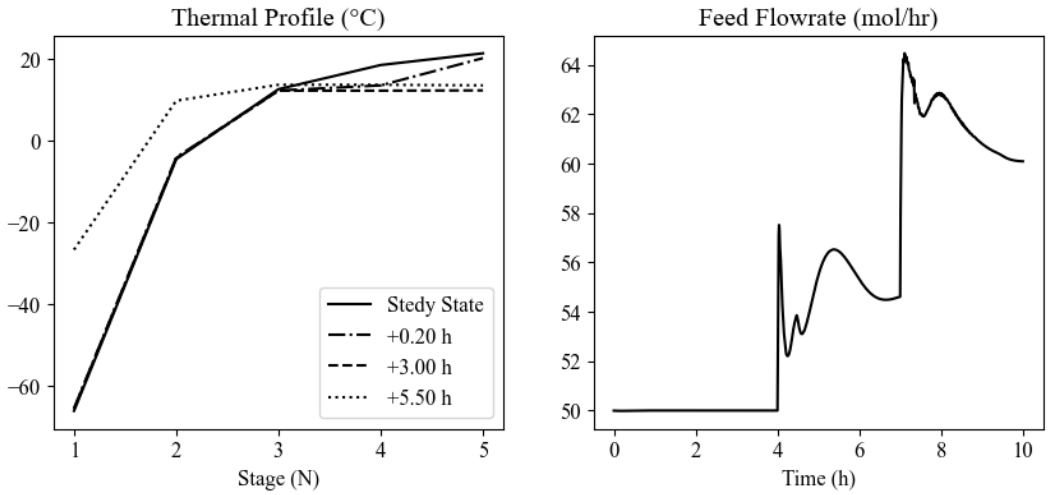

Fig. 4.55 Increasing feed's flow: column thermal profile at different time steps of the dynamic simulation (left-side chart) compared to the feed molar flow rate (right-side chart).

In conclusion, the simulations indicate that a control system based on the previously described logics behaves stably in the face of various disturbances imposed from the outside. Based on these results, the control logic is currently being implemented in collaboration with the members of the EP-DT-FS gas team at CERN.

Chapter 5

Conclusion: Status of the Systems and Future Goals

In the preceding sections of this thesis, the project's objectives and aims have been enstablished. Subsequently, a comprehensive analysis of the current system was imperative to identify areas for improvement (Section 4.1) and determine the approach for achieving the ultimate goals in terms of perfluorobutane recovery and purity. From the design and simulations conducted, it is evident that achieving a high-quality product is feasible. Specifically, the ability to accumulate and equalize flow and composition through the first subsystem (ATPS, Section 4.3) plays a pivotal role in smoothing the operation of the two downstream recovery subsystems. With the first recovery subsystem (DSE, Section 4.4), it is possible to recover decafluorobutane in liquid form with a molar purity of approximately 97%. The second subsystem (DC, Section 4.5), based on a structured packing distillation column (*Sulzer Chemtech AG's DX laboratory packings* [23], [21]), with an internal diameter and height of 0.03 and 1.5 m, exhibits superior performance. In steady-state conditions, it is theoretically possible to recover over 99% of C_4F_{10} exiting RICH-1 with nearly unit molar purity.

These results highlight that the work conducted is on the right path toward achieving the initially set objectives. Clearly, the research of solutions, simulations, and plant design optimization, extensively discussed in the preceding chapters, has progressed alongside various activities. Indeed, the stages through which a plant evolves from its embryonic state to effective operation are diverse. Specifically,

the approach used follows these steps: (1) Problem and objective definition; (2) Identification of potential solutions; (3) Design and simulation of promising solutions in line with the objectives; (4) Sourcing the necessary components and constructing the system; (5) System cleaning and thermal insulation; (6) Defining control logic, implementing sensors, control software, maintenance, and electrical components; (7) Safety inspection and leak tests; (8) Performance characterization.

It is evident that bringing an entire plant into operation demands a wider timeframe and the collaboration of numerous individuals and teams is also required. Currently, all three subsystems are in the transition between the fourth and fifth steps. While the assembly and cleaning of DSE are complete (Appendix D), the construction of DC and ATPS is temporarily halted due to material delivery delays (the list of materials is available in Appendix (E). Hence, this project is far from its end, moreover, the absence of experimental results remains the limitation of this work. Nevertheless, the project holds significant promise in economic, environmental, and future research terms. Firstly, the plant's operation would lead to a yearly reduction of approximately 600 tons of CO_2 equivalent emissions, as the 100-year Global Warming Potential (GWP) of C_4F_{10} is estimated at 9200 [7]. Secondly, it would enable CERN to save 15000 to 40000 €/year due to the exorbitant costs of perfluorobutane (ranging from 150 to 400 €/kg [32], [33]). Finally, the validation of future experimental data would be crucial for the optimization and revamping of all recovery systems at CERN. In fact, nearly all mixtures used in various experiments contain high-impact environmental chlorofluorocarbons, fluorocarbons, and fluorinated gases (CMS, ATLAS, and LHC experiments [34], [35]).

The work conducted during this period has been of utmost importance. In the first quarter of 2024, the entire team's objective is to complete the construction of the entire plant, carry out cleaning, insulation, and define control and safety systems. Adhering to this timeline is crucial to test the complete system by the second quarter of 2024. Clearly, the tests will follow an iterative approach, enabling the optimization of all thermodynamic variables influencing performance. Finally, comparing experimental results with those obtained through steady-state and dynamic simulations will be an intriguing aspect. Overall, collaborating with an organization like CERN and the prospect of future work are of utmost importance to me. Not only for my career development and personal growth, but particularly for the opportunity to have an impact on sustainability and environmental pollution reduction issues. Participating directly in the entire project cycle, from problem identification to solution research

and implementation, has been one of the most stimulating experiences throughout my engineering journey.

References

[1] Frank M. Forty R. Lhcb experiment, 1998.

[2] J.Sèguinot T. Ekelöf. The cerenkov ring-imaging detector: Recent progress and future development. *Physica Scripta*, 23:718–726, 1981.

[3] D. J. A. Cockerill R. M. Brown. Electromagnetic calorimetry. *Nuclear Instruments and methods in Physics research A*, 666:47–79, 2012.

[4] S. Easo. Overview of lhcb rich detector development. *Nuclear Instruments and methods in Physics research A*, pages 333–338, 2005.

[5] S. Easo. Development of the rich detectors in lhcb. *Nuclear Instruments and methods in Physics research A*, 502:46–51, 2005.

[6] D. Wiedner. The use of n-perfluorocarbons as rich radiators. *Nuclear Instruments and methods in Physics research A*, 595:216–219, 2008.

[7] Climate Change United Nations. Global warming potentials (ipcc fifth assessment report).

[8] A. A. H. Pàdue M. F. Costa. Interactions of carbon dioxide with liquid fluorocarbons. *Journal of Physical Chemistry*, 107:14020–14024, 2003.

[9] B. Gwinner et al. Co2 capture in flue gas: Semiempirical approach to select a potential physical solvent. *Industrial Engineering Chemistry Research*, 45:5044–5049, 2006.

[10] A. Valzt et al. Isothermal vapor–liquid equilibrium data for the carbon dioxide (r744)+decafluorobutane (r610) system at temperatures from 263 to 353k. *Fluid Phase Equilibria*, 304:44–51, 2011.

[11] H. Renon and J. M. Prausnitz. Local compositions in thermodynamic excess functions for liquid mixtures. *AIChE Journal*, 14:135–144, 1968.

[12] J. G. Hayden and J. P. O'Connell. A generalized method for predicting second virial coefficients. *Industrial and Engineering Chemistry Process Design and Development*, 14:209–216, 1975.

[13] O. Redlich and J. N. S. Kwong. On the thermodynamics of solutions. v. an equation of state. fugacities of gaseous solutions. *Chemical Reviews*, 44:233–244, 1949.

[14] D.Y. Peng and D. B. Robinson. A new two-constant equation of state. *Industrial Engineering Chemistry Fundamentals*, 15:59–64, 1976.

[15] V. Steffen and E. A. da Silva. Steady-state modeling of equilibrium distillation. *InTech*, 2017.

[16] Fernandez-Fassnacht E. The vapour pressure of co2 from 194 to 243 k. *Chemical Thermodynamics*, 16:469–474, 1984.

[17] R. H. Perry. *Perry's Chemical Engineer's Handbook (7th Edition)*. McGraw-Hill, 1997.

[18] R. E. Treyball. *Mass Transfer Operations (3rd Edition)*. McGraw-Hill, 1981.

[19] J. M. Coulson and J. F. Richardson. *Coulson and Richardson's Chemical Engineering (3rd Edition)*. BH, 1999.

[20] Alfa Laval. Cb30 plate heat exchanger.

[21] Sulzer Chemtech Ag. Dx laboratory packings features.

[22] *Dynamic Modeling*. Aspen Tech. Inc, 2005.

[23] A. E. Orlando Jr et al. Hetp evaluation of structured packing distillation column. *Brazilian Journal of Chemical Engineering*, 26:619–633, 2009.

[24] LHBc Collaboration. The lhcb detector at the lhc. *Journal of Instrumentation*, 3, 2008.

[25] M. Bosteels et al. C4f10 gas price, 2000.

[26] EEA Glossary. Gwp of perfluorocarbons.

[27] W. H. Mears J. A. Brown. Physical properties of n-perfluorobutane. *Journal of Physical Chemistry*, 62:960–962, 1958.

[28] S. I. Sandler. *Chemical, Biochemical and Engineering Thermodynamics (5th Edition)*. Wiley, 2017.

[29] The joule-thompson effect in carbon dioxide. 1942.

[30] Distillation fundamentals, 2017.

[31] D. E. Seborg. *Process Dynamics and Control (2nd Edition)*. Wiley, 2004.

[32] Dillon J. Hayes. Studies of refrigerant gases for use in cherenkov detectors at jefferson lab. 2018.

[33] Cern edh database (only accesible to cern's employees).

[34] B. Mandelli G . Rigoletti, R. Guida. Studies on rpc detectors operated with environmentally friendly gas mixtures in lhc-like conditions. *Nuclear Instruments ans Methods in Physics Research*, 1048, 2023.

[35] B. Mandelli et Al. Strategies for reducing the use of greenhouse gases from particle detectors operation at the cern lhc experiments. *Journal of Physics*, 2022.

Appendix A

Evaluation of RMSE and NRMSE

In order to evaluate the (Normalized) Root Mean Square Error for the pressure (*RMSEP*) and for the molar vapor fraction of CO_2 (*RMSEy*) it is necessary to define the generic *Error* and *Squared Error* as:

$$Error_i = \omega_i^{exp} - \omega_i^{model} \tag{A.1}$$

$$Squared\ Error_i = (\omega_i^{exp} - \omega_i^{model})^2 \tag{A.2}$$

Where ω can represent either the vapor pressure of the mixture or the vapor molar fraction of CO_2 and i goes from 0 to N (N is the number of available data points).
Once the Squared Error has been evaluated for each data point, it is possible to proceed by calculating the RMSEP and RMSEy substituting respectively P_i and y_i to ω_i:

$$RMSEP = \sqrt{\frac{\sum(P_i^{exp} - P_i^{model})^2}{N_p}} \tag{A.3}$$

$$RMSEy = \sqrt{\frac{\sum((y_i^{exp} - y_i^{model})^2}{N_p}} \tag{A.4}$$

Now, since the vapor pressure is a non-dimensionless variable it is interesting to define a dimensionless error as:

$$Dimensionless\ Error_i = \frac{P_i^{exp} - P_i^{model}}{P_i^{exp}} \tag{A.5}$$

Hence, it is possible to define a Normalized Root Mean Squared Error for the pressure variable (NRMSEP) as:

$$NRMSEP = \sqrt{\frac{\sum(\frac{P_i^{exp} - P_i^{model}}{P_i^{exp}})^2}{N_p}} \tag{A.6}$$

Appendix B

P&ID of the Plant

In this appendix, a brief description of the system in its various states is provided. Since it is a batch separation process, the control structure and operation of the individual subsystems must be finely tuned. To recap what has been described in the main body of the thesis, the system will need to manage three different phases during experiments on LHCb. These phases are "Filling," "Cleaning," and "Emptying." Additionally, the system can be divided into three subsystems: (1) Accumulation tank and pumping station (ATPS); (2) Distillation column (DC); (3) Double stage equilibrium (DSE). Each of these subsystems can be in an ON or OFF state depending on the reference phase.

Referring to Figure B.1, not all subsystems are meant to operate in every phase. It is, in fact, advisable to review each phase and understand how the system should behave.

- "Filling" Phase: During this phase, the detector is filled with C_4F_{10} to flush out the CO_2. The mixture exiting the detector enters the recovery system from the left (Process and Instrumentation Diagram in Figure B.2) and is accumulated in the accumulation phase of ATPS (4.3). After accumulation, the separation phase (Separation I and Separation II) follows. The equalized mixture is extracted from the tank and sent to one of the two recovery systems (DC or DSE), where carbon dioxide and decafluorobutane are respectively extracted as a gas and a liquid phase, respectively. The CO_2 is vented into the atmosphere, while C_4F_{10} is accumulated as a product in the refill volume.

- "Cleaning" Phase: The cleaning phase is necessary to remove nitrogen and oxygen present within the detector circuit. These molecules are due to air entering because of leaks along the entire circuit. The removal of N_2 and O_2 does not require accumulation; instead, the gaseous mixture is sent to the DSE, which removes air from the head of the first buffer.
- "Emptying" Phase: This phase is specular to filling. The operation is the same, but the detector is emptied of decafluorobutane by sending a flow of CO_2.

This brief description serves as a general understanding. Reading sections 4.3, 4.4 and 4.5 is key to fully understand the system's functioning.

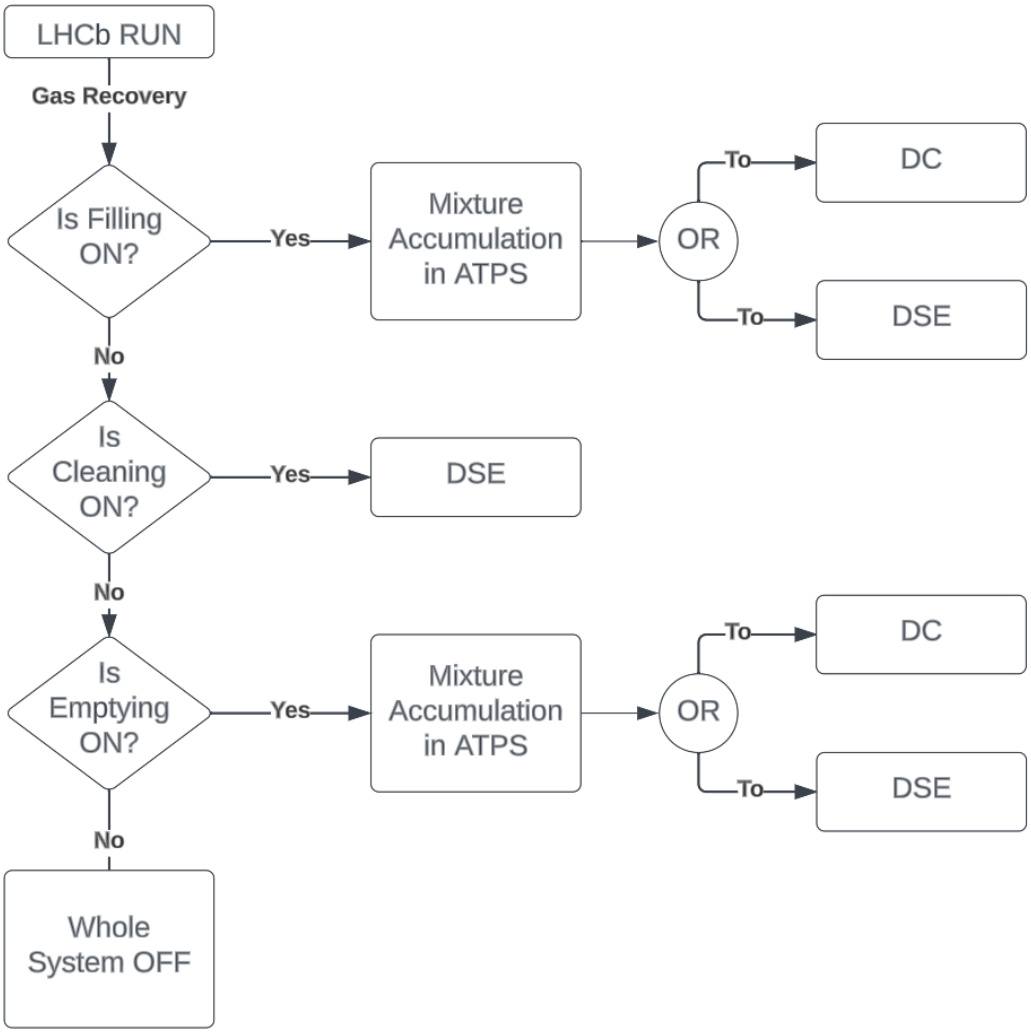

Fig. B.1 Flow Diagram of the decafluorobutane recovery system.

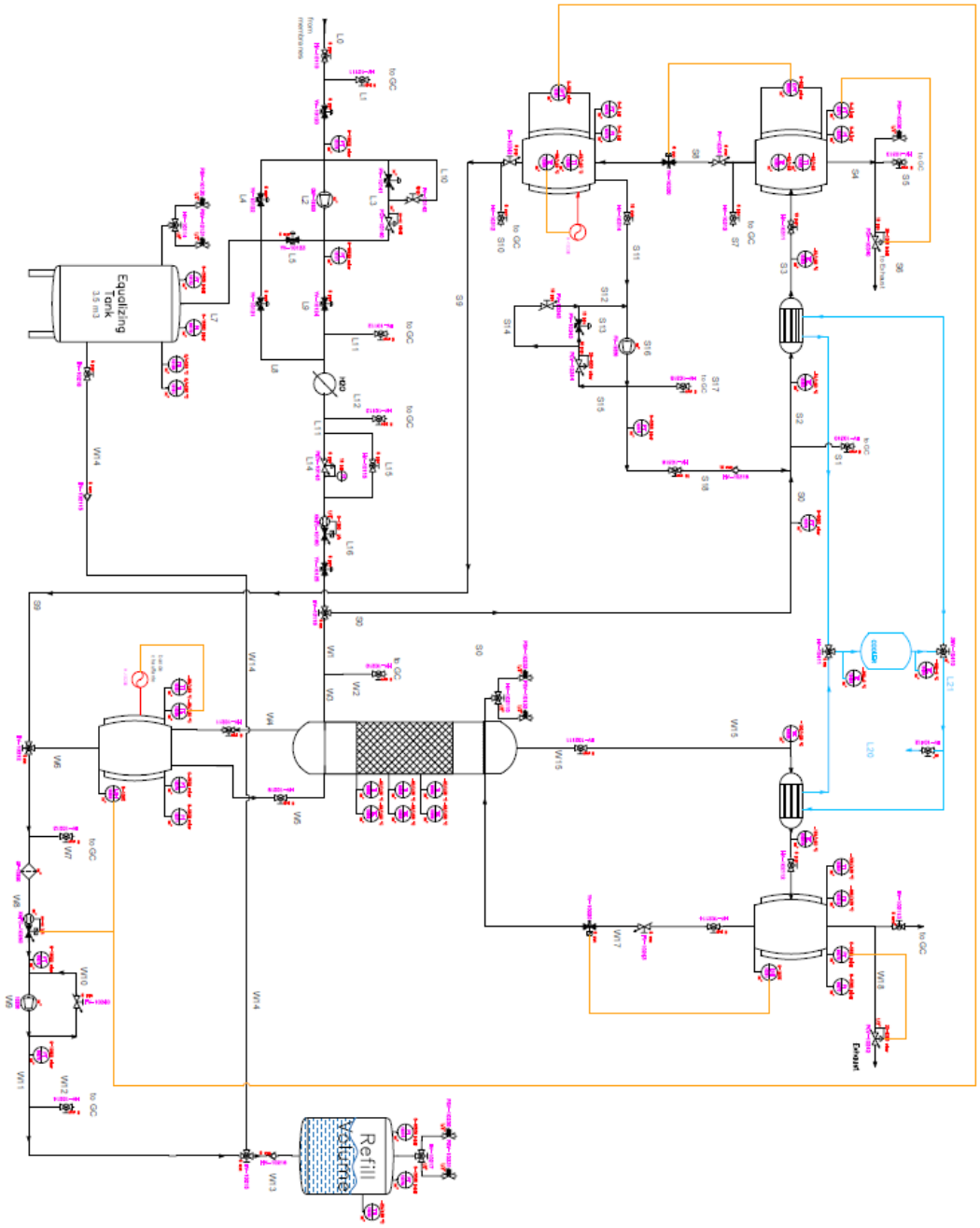

Fig. B.2 P&ID of the decafluorobutane recovery system.

Appendix C

Fitting the Solid-Vapor Equilibrium Line for CO_2

In this brief paragraph the extrapolation of a curve for estimating the frosting temperature of CO_2 as function of pressure. To do so, data have been retrieved from Fernandez-Fassnacht E. [16], then a given form of the P-T relationship must be assumed. In this case it is assumed that the saturation pressure of the solid (P_{ss}) is an exponential function of the temperature, thus it must have this form:

$$P_s^{SV}(T) = C_{s1}\ exp(C_{s2}\ T) \tag{C.1}$$

Where C_{s1} and C_{s2} are regression constants. Given this equation we can re-write is as:

$$ln(P_s^{SV}(T)) = ln(C_{s1}) + C_{s2}\ T \tag{C.2}$$

$$f(T) = C_{s3} + C_{s2}\ T \tag{C.3}$$

Where C_{s3} and $f(T)$ are the natural logarithms of C_{s1} and P_s^{SV}. Then, a linear regression has been applied (Least Squared Method) to find the values of the fitting constants. Having that we can verify the exactness of the regression based on the value of R^2 and $RMSE$, which in this case resulted, respectively, as 0.99931 and 0.01392 (range of validity from 194.23 to 216.56 K).
Finally the equation can be solved for T, thus knowing the constants, one can estimate

the solidification temperature given the pressure as:

$$T_{SV} = \frac{ln(P_s^{SV}) - C_{s3}}{C_{s2}} \tag{C.4}$$

The charts showing the regression error and the shape of T_{SV} as a function of P_s^{SV} are reported in section 4.5.4.

Appendix D

DSE: Construction Status

The DSE system is, at the time of writing this thesis, the most advanced in terms of its construction. As mentioned in the main body of the thesis, the construction and cleaning have been completed. The description of how the system operates has been addressed in Section 4.4. In this appendix, we provide photos and 3D representations to enhance a deeper understanding of its operation.

From the 3D representations (Fig D.1 and D.2), you can observe the various components mentioned in Section 4.4.1. The elements in gray represent the two buffers dedicated to partial condensation and subsequent vaporization, the operational temperatures of which have been deeply studied in Section 4.4.3. The components in green are PCV-10344, PV-10343, and FV-10345, which are the valves used for flow control and pressure regulation. As a fact, these are part of the compression loop. The compressor is placed below these valves in the lowest part of the rack (the compressor is not represented here). DPT-10390 and 10391 are depicted in yellow. The plate heat exchanger, similar to the CB30 used for the condenser of the DC system (Section 4.5.6), is shown in blue. Finally, in pink, you can see the valve PCV-10340, responsible for regulating the pressure in the first buffer by adjusting the exhaust flow rate. Lastly, from Figure D.3 and D.4 it is possible to appreciate the pictures of the status of the system.

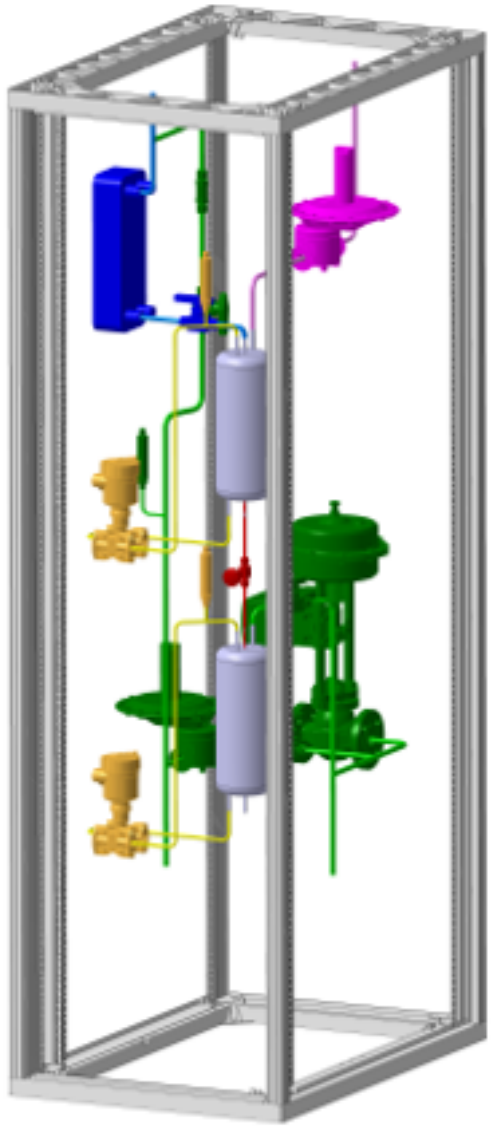

Fig. D.1 3D representation of the DSE system (1).

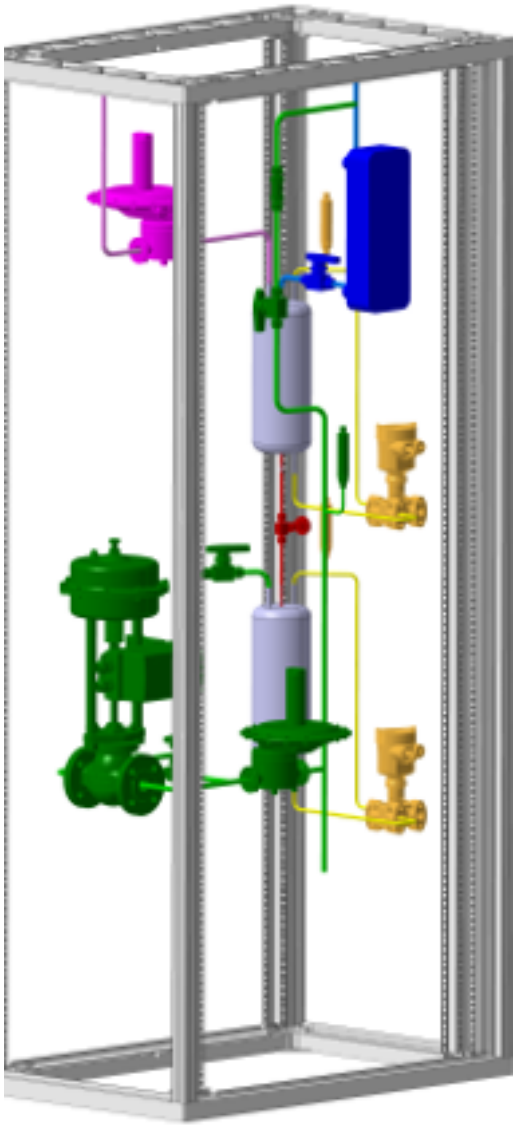

Fig. D.2 3D representation of the DSE system (2).

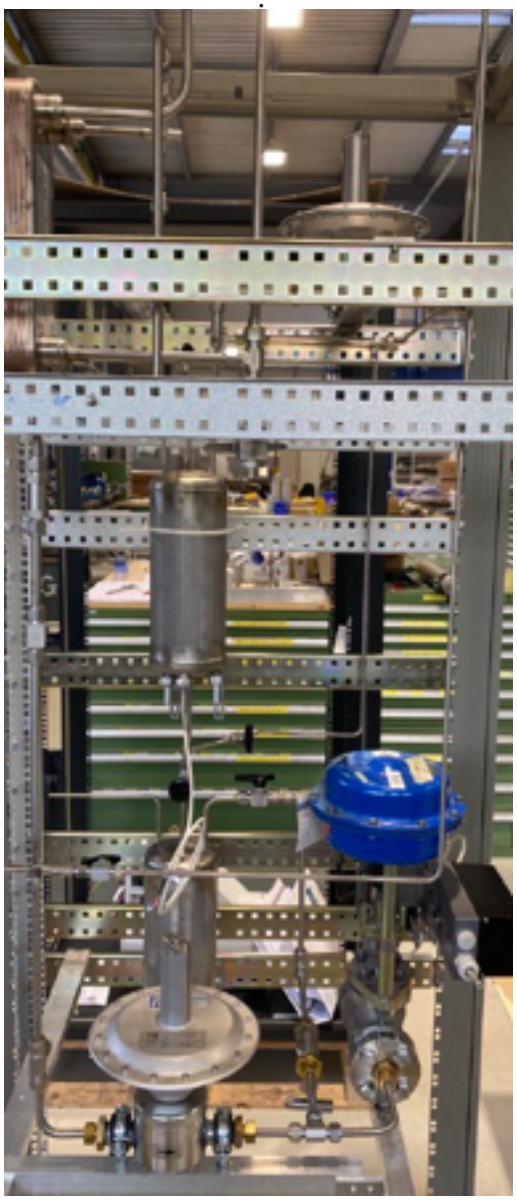

Fig. D.3 Picture of the DSE system (1).

Fig. D.4 Picture of the DSE system (2).

Appendix E

Components: Status and Features

This appendix contains the list of material required for the plant construction. The first tables (Tab E.1, E.2, E.3 and E.4) summarize the status of the orders, the supplier and the role and more. The second table (E.5 and E.6) regards the apparatuses as compressors, pumps, tanks and volumes.

SUPPLIER	NAME	ID	TIPO	OD (mm)	RANGE	POSITION	ORDER DATE	DELIVERY (WEEKS)	STATUS	SYSTEM	CLASS	NOTE
Arbor Fluiditec AG	Manual Valves (SS-42GS6MM-1466)	HV-10110	HV	6	CV 0,35	L0	15-May	2	A	ATPS	OPERATION VALVE	Manual open/close valve
Arbor Fluiditec AG	Manual Valves (SS-42GS6MM-1466)	HV-10111	HV	6	CV 0,35	L1	15-May	2	A	ATPS	OPERATION VALVE	Manual open/close valve
Arbor Fluiditec AG	Manual Valves (SS-42GS6MM-1466)	HV-10112	HV	6	CV 0,35	L11	15-May	2	A	ATPS	OPERATION VALVE	Manual open/close valve
Arbor Fluiditec AG	Manual Valves (SS-42GS6MM-1466)	HV-10113	HV	6	CV 0,35	L12	15-May	2	A	ATPS	OPERATION VALVE	Manual open/close valve
Arbor Fluiditec AG	3-Way valves	HV-10114	3WV	1/2'	CV 1,26	ET	22-May	4	A	ATPS	OPERATION VALVE	3 way valve 2open/1close
Arbor Fluiditec AG	Manual Valves (SS-42GS6MM-1466)	HV-10115	HV	6	CV 0,35	L15	15-May	2	A	ATPS	OPERATION VALVE	Manual open/close valve
Arbor Fluiditec AG	3-Way valves (SS-42GXS6MM-1466)	HV-10116	3WV	6	CV 0,35	L16	15-May	7	A	ATPS	OPERATION VALVE	3 way valve 2open/1close
Arbor Fluiditec AG	Pneumatic Valves (SS-6BK-MM-1C)	YV-10120	YV	6	CV 0,36	L0	15-May	7	A	ATPS	OPERATION VALVE	Pneumatic valve
Arbor Fluiditec AG	Pneumatic Valves (SS-6BK-MM-1C)	YV-10121	YV	6	CV 0,36	L8	15-May	7	A	ATPS	OPERATION VALVE	3W Pneumatic valve
Arbor Fluiditec AG	Pneumatic Valves (SS-6BK-MM-1C)	YV-10122	YV	6	CV 0,36	L4	15-May	7	A	ATPS	OPERATION VALVE	Pneumatic valve
Arbor Fluiditec AG	Pneumatic Valves (SS-6BK-MM-1C)	YV-10123	YV	6	CV 0,36	L5	15-May	7	A	ATPS	OPERATION VALVE	Pneumatic valve
Arbor Fluiditec AG	Pneumatic valves (SS-43GS10MM-1466)	YV-10124	YV	6	CV 0,36	L9	22-May	4	A	ATPS	OPERATION VALVE	Pneumatic valve
IN STOCK	IN STOCK	Safety Valve	PSV-10230	PSV	TO CALIBRATE	TO CHOOSE	CHF	IN STOCK	1	DC	SAFETY VALVE	Safety valve buffer Tank
IN STOCK	IN STOCK	Safety Valve	PSV-10231	PSV	TO CALIBRATE	TO CHOOSE	CHF	IN STOCK	1	DC	SAFETY VALVE	Safety valve buffer Tank
Zimmerli Messtechik AG	Pressure reducing valve (PR/F15S-GD-P3011/X/Sp)	PCV-10140	PCV	1/2'	DP 500-3000 spring mbar	L3	14-Jun	4	A	ATPS	REGULATION VALVE	Zimmerli to stabilize pressure for the compressor flow control
Von Rohr Armaturen AG	Regulation Valve	PV-10141	PV	15	CV 0,73 (0/10 bara & X/150 °C)	L3	02-Aug	12	W	ATPS	REGULATION VALVE	Von rohr to regulate the flow of the compressor
Cern Storage	Metering Valves (40.40.30.408.1)	FV-10142	FV	1/2'	CV 0,56	L10	07-Aug	1	A	ATPS	REGULATION VALVE	Metering valve to regulate manually the compressor flow
Cern Storage	Presure regulating valve	PICV-10143	PICV	1/2'	CV 0,73	L14			?	ATPS	REGULATION VALVE	regulatioj valve before feed massflowmeter
Bronkhorst France Sas	Mass flow controller (gas phase)	KMFC-10160	XMFC	1/4'	6/300 l/h	L16	26-Apr	19	A	ATPS	FLOWMETER	Gas mass flow meter to regulate the feed of the S1 and/or S2
IN STOCK	IN STOCK	PT-10170	PT	X	0-2,5 bar (X/+130°C)	L0	IN STOCK	IN STOCK	A	ATPS	P SENSOR	Pressure sensor and transmitter
Vega Technique SAS	Vegabar 29	PT-10171	PT	X	0-10 bar (X/+130°C)	L9	26-Oct	2	W	ATPS	P SENSOR	Pressure sensor and transmitter
Cern Storage	Manometre ECH- (-1,5 barg) D100	PI-10172	PI	X	1-5 barg	ET	22-May	4	A	ATPS	P SENSOR	Pressure sensor and transmitter
Vega Technique SAS	Vegabar 29	PT-10173	PT	X	0-10 bar (X/+130°C)	ET	26-Oct	2	W	ATPS	P SENSOR	Pressure sensor and transmitter
		TE-10180	TE	X		ET			E	ATPS	T SENSOR	Temperature sensor and transmitter
		TI-10181	TI	X		ET			E	ATPS	T SENSOR	Temperature indicator
Vaisala OYJ	DMT143 Miniature Dew Point Transmitter	H20	VAISALA	X	X	L13	15-May	2	A	ATPS	HUMIDITY SENSOR	Vaisala to measure water fraction in the feed stream
Arbor Fluiditec AG	Manual Valves (SS-42GS6MM-1466)	HV-10210	HV	6	CV 0,35	W2	15-May	2	A	DC	OPERATION VALVE	Manual open/close valve
Arbor Fluiditec AG	Manual Valves (SS-42GS6MM-1466)	HV-10211	HV	6	CV 0,35	W4	15-May	2	A	DC	OPERATION VALVE	Manual open/close valve
Arbor Fluiditec AG	3-Way valves (SS-42GXS6MM-1466)	HV-10212	3WV	6	CV 0,35	W6	22-May	4	A	DC	OPERATION VALVE	3 way valve 2open/1close
Arbor Fluiditec AG	Manual Valves (SS-42GS6MM-1466)	HV-10213	HV	6	CV 0,35	W7	15-May	2	A	DC	OPERATION VALVE	Manual open/close valve

Fig. E.1 List of valves and sensors of the subsystems (part 1).

Arbor Fluiditec AG	Manual Valves (SS-42GS6MM-1466)	HV-10214	HV	6	CV 0,35	W12	15-May	2	A	DC	OPERATION VALVE	Manual open/close valve
Arbor Fluiditec AG	3-Way valves (SS-42GXS6MM-1466)	HV-10215	3WV	6	CV 0,35	W13	22-May	4	A	DC	OPERATION VALVE	3 way valve 2open/1close
Arbor Fluiditec AG	Non return valves (SS-6C-MM-1/3-SC11)	HV-10216	NRV	6	CV 0,47	W13	22-May	4	A	DC	OPERATION VALVE	Non return valve avoiding back mixing
Arbor Fluiditec AG	3-Way valves	HV-10217	3WV	1/2'	CV 0,56	RV	22-May	4	A	DC	OPERATION VALVE	3 way valve 2open/1close
Arbor Fluiditec AG	Manual Valves (SS-42GS6MM-1466)	HV-10218	HV	6	CV 0,35	W14	15-May	2	A	DC	OPERATION VALVE	Manual open/close valve
Arbor Fluiditec AG	Manual Valves (SS-42GS6MM-1466)	HV-10219	HV	6	CV 0,35	W5	15-May	2	A	DC	OPERATION VALVE	Manual open/close valve
Arbor Fluiditec AG	3-Way valves	HV-102110	3WV	1/2'	CV 0,56	DC	22-May	4	A	DC	OPERATION VALVE	3 way valve 2open/1close
Arbor Fluiditec AG	Manual Valves (SS-42GS6MM-1466)	HV-102111	HV	6	CV 0,35	W15	15-May	2	A	DC	OPERATION VALVE	Manual open/close valve
Arbor Fluiditec AG	Manual Valves (SS-42GS6MM-1466)	HV-102112	HV	6	CV 0,35	W16	15-May	2	A	DC	OPERATION VALVE	Manual open/close valve
Arbor Fluiditec AG	Manual Valves (SS-42GS6MM-1466)	HV-102113	HV	6	CV 0,35	W19	15-May	2	A	DC	OPERATION VALVE	Manual open/close valve
Arbor Fluiditec AG	Manual Valves (SS-42GS6MM-1466)	HV-102114	HV	6	CV 0,35	W17	15-May	2	A	DC	OPERATION VALVE	Manual open/close valve
Arbor Fluiditec AG		FV-10240	FV	6	CV 0,37	W10	15-May	2	A	DC	REGULATION VALVE	Metering valve to reguluate the pump
Arbor Fluiditec AG	Metering Valves (SS-1RS6MM-SC11)	FV-10341	FV	6	CV 0,37	W10	15-May	2	A	DC	REGULATION VALVE	Metering valve to reguluate liquid from buffer 1
Zimmerli Messtechik AG	Back pressure valves (ZM-B15S-GD-P200180/X)	PCV-10242	PCV	1/2'	DP 20-200 spring +2000 dome mbar	W18	10-May	7	A	DC	REGULATION VALVE	Zimmerli to regulate condenser pressure
Bronkhorst France Sas	mini CORI-FLOW M14 liquid	KMFC-10260	XMFC	1/4'	0,18/9 l/h	W8	16-May	18	A	DC	FLOWMETER	Liquid Mass flowmeter
IN STOCK	Safety Valve	PSV-10230	PSV	1/2'	TO CALIBRATE	RV	IN STOCK	1	A	DC	SAFETY VALVE	For C4F10 tank
IN STOCK	Safety Valve	PSV-10231	PSV	1/2'	TO CALIBRATE	RV	IN STOCK	1	A	DC	SAFETY VALVE	For C4F10 tank
IN STOCK	Safety Valve	PSV-10232	PSV	1/2'	TO CALIBRATE	DC	IN STOCK	1	A	DC	SAFETY VALVE	For column head
IN STOCK	Safety Valve	PSV-10233	PSV	1/2'	TO CALIBRATE	DC	IN STOCK	1	A	DC	SAFETY VALVE	For column head
Arbor Fluiditec AG	Metering Valves (SS-1RS6MM-SC11)	FV-10243	FV	6	CV 0,37	W17	15-May	2	A	DC	REGULATION VALVE	Condeser drum metering valve
Vega Technique SAS	Vegapulse 6X	LSH-10290	LSH	NaN	0/120 m (-55/+150 °C)	REB	27-Apr	8	A	DC	LEVEL SENSOR	Reboiler drum LSH
Vega Technique SAS	Vegaflex 81	LSH-10291	LSH	NaN	0/0.3 m (-40/+150 °C)	COND	27-Apr	8	A	DC	LEVEL SENSOR	Condenser drum LSH
Vega Technique SAS	Vegabar 29	PT-10270	PT	NaN	0-5 bar (-90/+200 °C)	REB	27-Apr	8	A	DC	P SENSOR	Reboiler PT
Cern Storage	Manometre ECH- (-1,5 barg) D100	PI-10271	PI	NaN	1-5 barg	REB	22-May	4	A	DC	P SENSOR	Reboiler PI
Vega Technique SAS	Vegabar 29	PT-10272	PT	NaN	0-5 bar (-90/+200 °C)	W8	26-Oct	2	W	DC	P SENSOR	Prepump PT
Vega Technique SAS	Vegabar 29	PT-10273	PT	NaN	0-5 bar (-90/+200 °C)	W11	26-Oct	2	W	DC	P SENSOR	Postpump PT
Cern Storage	Manometre ECH- (-1,5 barg) D100	PI-10274	PI	NaN	1-5 barg	RV	22-May	4	A	DC	P SENSOR	C4F10 Tank PI
Vega Technique SAS	Vegabar 29	PT-10275	PT	NaN	0-5 bar (-90/+200 °C)	RV	26-Oct	2	W	DC	P SENSOR	C4F10 Tank PT
Vega Technique SAS	Vegabar 29	PT-10276	PT	Nan	0-5 bar (-90/+200 °C)	COND	26-Oct	2	W	DC	P SENSOR	Condeser PT
Vega Technique SAS	Vegabar 81	PT-10276	PT	NaN	0-5 bar (-90/+200 °C)	COND	27-Apr	8	A	DC	P SENSOR	Condeser PT
Cern Storage	Manometre ECH- (-1,5 barg) D100	PI-10277	PI	NaN	1-5 barg	COND	22-May	4	A	DC	P SENSOR	Condenser PI
		TI-10280	TI	X		REB			E	DC	T SENSOR	Reboiler TI
		TE-10281	TE	X		REB			E	DC	T SENSOR	Reboiler TE
		TE-10282	TE	X		RV			E	DC	T SENSOR	C4F10 Tank TE
		TI-10283	TI	X		DC			E	DC	T SENSOR	Column TI
		TE-10284	TE	X		DC			E	DC	T SENSOR	Column TE
		TI-10285	TI	X		DC			E	DC	T SENSOR	Column TI
		TE-10286	TE	X		DC			E	DC	T SENSOR	Column TE
		TI-10287	TI	X		DC			E	DC	T SENSOR	Column TI
		TE-10288	TE	X		DC			E	DC	T SENSOR	Column TE
		TE-10289	TE	X		W15			E	DC	T SENSOR	Input Exchanger TE

Fig. E.2 List of valves and sensors of the subsystems (part 2).

		TE-102810	TE	X		W16			E	DC	T SENSOR	Output Exchanger TE
		TI-102811	TI	X		COND			E	DC	T SENSOR	Condenser TI
		TE-102812	TE	X		COND			E	DC	T SENSOR	Condenser TE
Arbor Fluiditec AG	Manual Valves (SS-42GS6MM-1466)	HV-10310	HV	6	CV 0,35	S1	15-May	2	A	DSE	OPERATION VALVE	Manual open/close valve
Arbor Fluiditec AG	Manual Valves (SS-42GS6MM-1466)	HV-10312	HV	6	CV 0,35	S7	15-May	2	A	DSE	OPERATION VALVE	Manual open/close valve
Arbor Fluiditec AG	Manual Valves (SS-42GS6MM-1466)	HV-10313	HV	6	CV 0,35	S5	15-May	2	A	DSE	OPERATION VALVE	Manual open/close valve
Arbor Fluiditec AG	Manual Valves (SS-42GS6MM-1466)	HV-10315	HV	6	CV 0,35	S17	15-May	2	A	DSE	OPERATION VALVE	Manual open/close valve
Arbor Fluiditec AG	Manual Valves (SS-42GS6MM-1466)	HV-10317	HV	6	CV 0,35	S10	15-May	2	A	DSE	OPERATION VALVE	Manual open/close valve
Arbor Fluiditec AG	Non return valves (SS-10C-MM-1/3-SC11)	HV-10318	NRV	10	CV 1,68	S18	22-May	4	A	DSE	OPERATION VALVE	Non return valve avoiding back mixing
IN STOCK	Safety Valve	PSV-10233	PSV	1/2'	TO CALIBRATE	DC	IN STOCK	1	A	DSE	SAFETY VALVE	Safety valve buffer 1
Zimmerli Messtechik AG	Back pressure valves (ZM-B15S-GD-P200180/X)	PCV-10340	PCV	1/2'	DP 20-200 spring +2000 dome mbar	S6	10-May	7	A	DSE	REGULATION VALVE	Zimmerli to regulate buffer 1 pressure
Zimmerli Messtechik AG	Low Pressure Reducing valve (ZM-R15S-GD-P100020/Sp/X)	PCV-10344	PCV	1/2'	DP 100-1050 spring mbar	S15	14-Jun	4	A	DSE	REGULATION VALVE	Zimmerli to stabilize pressure for the compressor flow control
Arbor Fluiditec AG	Metering Valves (SS-1RS6MM-SC11)	FV-10341	FV	6	CV 0,37	S8	15-May	2	A	DSE	REGULATION VALVE	Metering valve to reguluate liquid from buffer 1
Arbor Fluiditec AG	Metering Valves (SS-1RS6MM-SC11)	FV-10342	FV	6	CV 0,37	S9	07-Aug	1	A	DSE	REGULATION VALVE	Metering valve to reguluate liquid from buffer 2
Cern Storage	Metering Valves (40.40.30.408.1)	FV-10345	FV	1/2'	CV 0,56	S14	07-Aug	1	A	DSE	REGULATION VALVE	Metering valve to regulate manually the compressor flow
Von Rohr Armaturen AG	Regulation Valve	PV-10343	PV	15	CV 0,73 (0/10 bara & X/150 °C)	S13	02-Aug	12	W	DSE	REGULATION VALVE	Von rohr to regulate the flow of the compressor
IN STOCK	IN STOCK	PT-10370	PT	X	0-2,5 bar (X/+130°C)	B1	IN STOCK	IN STOCK	A	DSE	P SENSOR	Pressure sensor and transmitter
Cern Storage	Manometre ECH (-1;5 barg) D100	PI-10371	PI	X	1-5 barg	B1	02-May	1	A	DSE	P SENSOR	Pressure sensor and transmitter
IN STOCK	Vegabar 29	PT-10372	PT	X	0-2,5 bar (X/+130°C)	B2	IN STOCK	IN STOCK	A	DSE	P SENSOR	Pressure sensor and transmitter
Cern Storage	Manometre ECH (-1;5 barg) D100	PI-10373	PI	X	1-5 barg	B2	02-May	1	A	DSE	P SENSOR	Pressure sensor and transmitter
IN STOCK	Vegabar 29	PT-10374	PT	X	0-5 bar (X/+130°C)	S18	IN STOCK	IN STOCK	A	DSE	P SENSOR	Pressure sensor and transmitter
Vega Technique SAS	VegaDF85 Differential P transmitter	DPT-10390	LSH	1/4'	0,1/160 bara (-40/+105 °C)	B1	28-Aug	6	W	DSE	LEVEL SENSOR	Differential Pressure level sensor and transmitter
Vega Technique SAS	VegaDF85 Differential P transmitter	DPT-10391	LSH	1/4'	0,1/160 bara (-40/+105 °C)	B2	28-Aug	6	W	DSE	LEVEL SENSOR	Differential Pressure level sensor and transmitter
		TE-10380	TE	X		S2			E	DSE	T SENSOR	Temperature sensor and transmitter
		TE-10381	TE	X		B1			E	DSE	T SENSOR	Temperature sensor and transmitter
		TI-10382	TI	X		B1			E	DSE	T SENSOR	Temperature indicator
		TE-10383	TE	X		CM			E	DSE	T SENSOR	Temperature sensor and transmitter
		TE-10384	TE	X		CM			E	DSE	T SENSOR	Temperature sensor and transmitter
		TE-10385	TE	X		S3			E	DSE	T SENSOR	Temperature sensor and transmitter
		TE-10386	TE	X		B2			E	DSE	T SENSOR	Temperature sensor and transmitter
		TI-10387	TI	X		B2			E	DSE	T SENSOR	Temperature indicator
Arbor Fluiditec AG	Non return valves (SS-6C-MM-1/3-SC11)	HV-102115	NRV	6	CV 0,47	W14	22-May	4	A	DC	OPERATION VALVE	Non return valve avoiding back mixing

Fig. E.3 List of valves and sensors of the subsystems (part 3).

Arbor Fluiditec AG	Pneumatic valves (SS-43GS10MM-1466)	YV-10125	YV	6	CV 0,36	L16	22-May	4	A	ATPS	OPERATION VALVE	Pneumatic valve
Vega Technique SAS	Vegabar 29	PT-10375	PT	X	0-10 bar (X/+130°C)	S0	26-Oct	2	W	DSE	P SENSOR	Pressure sensor and transmitter
ASCO NUMATICS GMBH (EMERSON)	E262K114S1TD0	YV-10220	YV	1/4"	KV 0,63 (KV =1,16 CV)	W17	20-Oct	3	W	DC	ELECTRIC VALVE	Solenidal valve for liquid level ON/OFF control
ASCO NUMATICS GMBH (EMERSON)	E262K114S1TD0	YV-10320	YV	6	KV 0,63 (KV =1,16 CV)	S8	20-Oct	3	W	DSE	ELECTRIC VALVE	Solenidal valve for liquid level ON/OFF control
		H-10390	H	X		B1			E	DSE	BANDE CHAUFFANTE	Resistive heater
		H-10290	H	X		REB			E	DC	BANDE CHAUFFANTE	Resistive heater

Fig. E.4 List of valves and sensors of the subsystems (part 4).

SUPPLIER	NAME and SPECIFICATIONS		CODE	NUMBER	ORDER DATE	DELIVERY (WEEKS)
Sulzer Managment AG	STRCTURED PACKING	DX PACKING 316L 29,4mm	STR-PAK-01	15	13-Sep	10
Sulzer Managment AG	STRCTURED PACKING	DX PACKING 316L 29,4mm	STR-PAK-02	15	13-Sep	16
Munters Euroform Gmbh	Pall rings for random packing	Pall Rings 10 mm (SS304)	RND-PAK-01	1	26-Apr	12
Cern Storage	(buffers body)Tube Rond 304L 114,3x2,6	39.39.05.113.8	MAT-BUF-1	1x1m	02-May	1
Cern Storage	(buffers head and bottom)Fond Bonbe 316L 114,3x3,0	41.03.06.100.1	MAT-COL-1	8	02-May	1
Cern Storage	(buffers body)Tube Rond 304L 33,7x2,6	39.39.05.033.7	MAT-BUF-2	1x4m	02-May	1
Cern Storage	(buffers head and bottom)Fond Bonbe 316L 33,7x2,0	41.03.06.025.5	MAT-BUF-3	2	02-May	1
Haug Sauer Kompressoren AG	Hot Discharge Compressor	HAUG-Pluto 11E 26 D4 (Hot Discharge)	CMP-10150	1	15-May	12
Cern Storage	(buffers body)Tube Rond 304L 139,7x2,6	39.39.05.139.9	MAT-BUF-4	1x2,3m	17-May	1

Fig. E.5 List of main apparatuses of the subsystems (part 1).

Cern Storage	(buffers head and bottom)Fond Bonbe 316L 139,7x3,0	41.03.06.125.2	MAT-BUF-5	2	17-May	1
Haug Sauer Kompressoren AG	Compressor	HAUG-Pluto 11E 26 D4	CMP-10350	1	24-May	12
Pommee	Accumulation Tank	Tank Pop 7bar, Pmax 10 bar	AT	1	30-Aug	20
Interfluid SRL	Pump	5LG AIR DRIVEN GAS BOOSTER 4:1	PUMP-10250	1	12-Jun	11
Igz Instruments AG	Lauda Cooling Machine	Thermostat de process Lauda IN 1590 XTW (-90...220 °C 8,50kW)	COOLING MACHINE	1	15-Sep	14
Christof Fischer Kaelte Klima	Plate Heat Exchangers	Echang. chal. plaques Alfa Lav. CB30-24H	HEAT-EX	4	14-Jun	6

Fig. E.6 List of main apparatuses of the subsystems (part 2).